

ПРИМЉЕНО:		17. 09. 2024	
Рад.јед.	б р о ј	Арх.шифра	Прилог
0801	165211		

НАУЧНОМ ВЕЋУ ИНСТИТУТА ЗА ФИЗИКУ

Adresa: Pregrevica 118, 11000 Beograd, Srbija

PREDMET: Molba za pokretanje postupka za sticanje zvanja NAUČNI SARADNIK

Sa obzirom da ispunjavam kriterijume propisane od strane Ministarstva nauke i Naučnog veća Instituta za fiziku u Beogradu za sticanje zvanja NAUČNI SARADNIK, molim Naučno veće Instituta za fiziku da pokrene postupak za moj izbor u zvanje.

U prilogu dostavljam:

1. Mišljenje rukovodioca grupe sa predlogom članova komisije za izbor u zvanje,
2. Stručnu biografiju,
3. Pregled naučne aktivnosti,
4. Elemente za kvalitativnu analizu naučnog doprinosa,
5. Elemente za kvantitativnu analizu naučnog doprinosa,
6. Spisak objavljenih radova i njihove kopije,
7. Podatke o citiranosti radova (Scopus),
8. Rešenje o prethodnom izboru u zvanje,
9. Potvrdu o odbranjenoj doktorskoj disertaciji.

Beograd

20. septembar 2024.



dr Miloš Travar

1 MIŠLJENJE RUKOVODIOCA GRUPE SA PREDLOGOM ČLANOVA KOMISIJE ZA IZBOR U ZVANJE NAUČNI SARADNIK - KANDIDAT MILOŠ TRAVAR

Miloš Travar, rođen 9.7.1993. u Novom Sadu je 9.8.2024. uspešno odbranio doktorsku disertaciju pod naslovom "Verifikacija simulacionih tehnika u izučavanju nuklearnih procesa" ("Verification of simulation techniques in the study on nuclear processes") na Prirodno-matematičkom fakultetu Univerziteta u Novom Sadu. Mentori doktorske disertacije su bili prof. dr Jovana Nikolov, redovni profesor Prirodno-matematičkog fakulteta Univerziteta u Novom Sadu, i dr Dejan Joković, viši naučni saradnik Instituta za fiziku u Beogradu.

Miloš Travar je u periodu od 2019. do 2023. bio nosilac stipendije Ministarstva prosvete, nauke i tehnološkog razvoja Vlade Republike Srbije kao student doktorskih studija u okviru projekta OI171002 "Nuklearne metode istraživanja retkih događaja i kosmičkog zračenja". Od 15. maja 2023. Miloš je zaposlen na Institutu za fiziku u Beogradu u okviru Niskofonske laboratorije za nuklearu fiziku. Tokom studija, Miloš je kao glavni autor ili koautor objavio više naučnih radova u visoko kvalifikovanim naučnim časopisima. Iz priloženog materijala, Miloš zadovoljava sve predviđene uslove u skladu sa Pravilnikom o postupku, načinu vrednovanja i kvantitativnom iskazivanju naučno-istraživačkih rezultata Ministarstva prosvete, nauke i tehnološkog razvoja Vlade Republike Srbije, za izbor u zvanje naučni saradnik, te predlažem Naučnom veću Instituta za fiziku u Beogradu da pokrene izbor Miloša Travara u pomenuto zvanje.

Za članove komisije predlažem:

- **dr Dejan Joković** ☉, viši naučni saradnik Instituta za fiziku (Beograd),
- **dr Nikola Veselinović** ☉, viši naučni saradnik Instituta za fiziku (Beograd),
- **prof. dr Jovana Nikolov** ☉, redovni profesor Prirodno-matematičkog fakulteta (Novi Sad).

ИНСТИТУТ ЗА ФИЗИКУ

ПРИМЉЕНО:		17. 09. 2024	
Ред.јед.	б р о ј	Арх.шифра	Прилог
0801	165212		

Beograd
20. avgust 2024.

dr Vladimir Udovičić, naučni savetnik
Rukovodilac Niskofonske laboratorije za nuklearnu fiziku

1 STRUČNA BIOGRAFIJA - MILOŠ TRAVAR

Miloš Travar rođen je 9. jula 1993. u Novom Sadu. Osnovnu školu "Jovan Popović" završava u Novom Sadu, posle koje upisuje prirodno-matematički smer gimnazije "Jovan Jovanović Zmaj". Nakon završetka gimnazije 2012. godine upisuje osnovne akademske studije fizike, smer medicinska fizika, na departmanu za fiziku, Prirodno-matematički fakultet, Univerzitet u Novom Sadu. Posle osnovnih studija upisuje i master akademske studije 2017. na istoj katedri, smer nuklearna fizika, koje završava 2018. sa odbranom master rada pod naslovom "Priprema NICOLE opreme za LTNO eksperiment". Doktorske akademske studije upisuje 2018. godine takođe na katedri za nuklearnu fiziku Prirodno-matematičkog fakulteta koje uspešno završava 9.8.2024. sa disertacijom pod naslovom "Verifikacija simulacionih tehnika u izučavanju nuklearnih procesa".

U periodu od 2019. do 2023. godine Miloš je bio stipendista Ministarstva nauke, prosvete i tehnološkog razvoja Vlade Republike Srbije, angažovan kao student doktorant na projektu OI171002 naslova "Nuklearne metode istraživanja retkih događaja i kosmičkog zračenja". Od 15. maja 2023. godine zaposlen je na Institutu za fiziku u Beogradu, kao istraživač saradnik u okviru Niskofonske laboratorije za nuklearnu fiziku.

Tokom master i doktorskih studija uključuje se u više različitih naučnih grupa u okviru kojih sprovodi svoja istraživanja. Od 2018. godine postaje član CERN-a, u okviru ISOLDE kolaboracije, gde radi na NICOLE eksperimentu. Takođe je bio dobitnik više ENEN stipendija (European Nuclear Education Network) u okviru kojih je sproveo istraživačke radove na institutima European Commission - Joint Research Centre u Belgiji i Nemačkoj. Pored ovih kolaboracija član je i drugih naučnih grupa sa više različitih svetski priznatih instituta. Naučne oblasti kojima se bavi su γ -spektrometrija, Monte Karlo simulacije, nuklearna forenzika, radioekologija i druge. Tokom master i doktorskih studija učestvovao je na raznim internacionalnim školama i treninzima. Autor i koautor je više naučnih radova u međunarodnim časopisima koji su svojevrsno prezentovani na međunarodnim naučnim skupovima i konferencijama na kojima je učestvovao.

Beograd
20. septembar 2024.



dr Miloš Travar

2 PREGLED NAUČNE AKTIVNOSTI

Naučno-istraživački rad dr Miloša Travara se temelji na istraživanjima u okviru oblasti oblasti Monte Karlo simulacija, γ -spektrometrije, kosmike, radioekologije, nuklearne forenzike i bezbednosti u drugih.

Shodno tome, rad kandidata se može klasifikovati u nekoliko kategorija:

- Ispitivanja nuklearnih procesa,
- Razvijanje i validacija Monte Karlo simulacija,
- Eksperimentalne i simulacione tehnike γ -spektrometrije.

Kandidat je do sada učestvovao na znatnom broju međunarodnih naučnih skupova i kao autor i koautor je objavio ukupno 7 radova u vrhunskim međunarodnim časopisima, od toga 5 od trenutka biranja u prethodno zvanje istraživača saradnika (datum izbora 7.2.2022.) pa do danas.

RAZVIJANJE I VALIDACIJA MONTE KARLO KODOVA

Jedan od glavnih zadata γ -spektrometrijske laboratorije predstavlja precizno određivanje tj. kvantifikaciju detekcione efikasnosti eksperimentalne postavke. U standardnoj γ -spektrometrijskoj praksi, određivanje aktivnosti radioizotopa koji emituju nisko-energetske kvante zračenja se može pokazati kao relativno složeno. γ -spektrometrija se često koristi kao inicijalan alat u određivanju osnovnih karakteristika nepoznatih uzoraka, posebno kada se za uzorak sumnja da je deo nezakonitog transporta tj. krijumčarenja radioaktivnih materijala. Glavna zabrinutost u većini slučajeva predstavlja uranijum, kako se jedan od njegovih izotopa (^{235}U) može iskoristiti u svrhu nuklearnog naoružanja. Upravo γ -spektrometrija, u kombinaciji sa Monte Karlo simulacijama, predstavlja najčešće korišćenu nedestruktivnu tehniku u nuklearnoj forenzici u kontekstu analize izotopskih kompozicija uranijumskih matrica. Glavni cilj u okviru istraživanja ove prirode bio je razviti simulacionu metodu korišćenjem GEANT4 transportnog Monte Karlo simulacionog paketa i ispitati prednosti i nedostatke u komparaciji sa polu-empirijskim metodama. Na osnovu generalnih rezultata prezentovani su predlozi korišćenja kako polu-empirijskih tako i simulacionih metoda u svrhu istraživanja ove prirode. Rezultati istraživanja su objavljeni u radu:

1. Testing of EFFTRAN and Angle software in comparison to GEANT4 simulations in gamma spectrometry of cylindrical and noncylindrical sample geometries

Autori: A. Vraničar, J. Nikolov, N. Todorović, I. Maksimović, M. Mladenović, D. Mrđa, **M. Travar**
Časopis: *Nuclear Instruments and Methods in Physics Research Section A: Accelerators, Spectrometers, Detectors and Associated Equipment*, Volume 986, 11. januar 2021; **M22, IF 1.335**
DOI: [10.1016/j.nima.2020.164768](https://doi.org/10.1016/j.nima.2020.164768)

ISPITIVANJE NUKLEARNIH PROCESA - FISIONA DINAMIKA

Proteklih godina modelovanje nuklearnog procesa fisije je doživelo znatni iskorak. Razvijeni su kodovi sa ciljem simuliranja emisije fisionih neutrona i γ -fotona. Svi modeli dele zajedničko svojstvo oslanjanja na

eksperimentalne podatke fisionih fragmenata, npr. emisionih prinosa i ukupne kinetičke energije, kao i podataka nuklearne strukture. Kako su podaci nuklearne strukture za jezgra bogata neutronima veoma siromašni, neprecizni ili pak nedostupni, proračuni modela se oslanjaju na ekstrapolirana svojstva posmatanjem stabilnih jezgara. Podela ekscitacione energije između fisionih fragmenata u trenutku fisije igra krucijalnu ulogu i može biti parametrizovana na osnovu ograničenih podataka promptnih fisionih neutrona. Ovo ostavlja teoretičare sa brojnim parametrima modela. Kao posledica, koherentan opis emisije promptnih neutrona i γ -fotona i dan danas ne poseduje neophodnu preciznost i predvidljivost. Posmatrani su promptni γ -fotoni emitovani tokom spontane fisije ^{252}Cf . Srednji broj (multiplicitet) promptnih γ -fotona je određen u funkciji mase fisionih fragmenta i ukupne kinetičke energije. Dobijeni podaci, dobijeni korišćenjem tri detektora u tri različite postavke, nedvosmisleno potvrđuju "testerast" oblik funkcije multipliciteta u funkciji mase, u kontrastu sa prethodno objavljenim podacima. Dodatno, zavisnost multipliciteta u odnosu na ukupnu kinetičku energiju je eksperimentalno određeno i poređeno sa skorašnih publikacijama. Rezultati istraživanja su objavljeni u radu:

1. **Experimental information on mass- and TKE-dependence of the prompt fission γ -ray multiplicity**

Autori: M. Travar, V. Piau, A. Göök, O. Litaize, J. Nikolov, A. Oberstedt, S. Oberstedt, J. Enders, M. Peck, W. Geerts, M. Vidali
Časopis: *Physics Letters B*, Volume 817, 10. jun 2021; **M21, IF 4.95**
DOI: [10.1016/j.physletb.2021.136293](https://doi.org/10.1016/j.physletb.2021.136293)

EKSPERIMENTALNE I SIMULACIONE TEHNIKE γ -SPEKTROMETRIJE

Tokom godina HPGe sistemi su se pokazali kao odličan praktičan alat i kao takvi su utemeljili svoju široku primenu u raznim granama nuklearne fizike, uključujući i niskofonsku γ -spektrometriju. Jedna od glavnih prednosti ove discipline predstavlja njenu prostu pripremu uzorka koja u najvećem broju slučajeva ne zahteva dodatnu hemijsku obradu i/ili separaciju. Stoga, uz samo jedno merenje moguće je simultano izvesti kako kvalitativnu tako i kvantitativnu analizu. Pouzdanost HPGe sistema pored ostalih faktora zavisi i od kvaliteta kalibracije. Prilikom identifikacije radionuklida neophodna je precizna energetska kalibracija, dok je sa druge strane u cilju dobijanja kvalitetne karakterizacije aktivnosti neophodno precizno poznavanje FEPE funkcije prilagođene eksperimentalnim uslovima. U kombinaciji sa Monte Karlo simulacijama moguće je nadomestiti određene eksperimentalne nedostatke γ -spektrometrije kao što je upravo precizno poznavanje FEPE funkcije, ili npr. kvantifikacija uzoraka nepoznatih hemijskih sastava. Precizno poznavanje matrice uzorka igra značajnu ulogu u određivanju koncentracija aktivnosti uzoraka i obrnuto, za šta je takođe neophodno imati precizan i pouzdan simulacioni model ukoliko se koriste Monte Karlo simulacije u kombinaciji sa γ -spektrometrijom. U okviru ovih istraživanja kvantifikacija matrice je vršeno na nepoznatim uranijumskim uzorcima dok je prethodno optimizacija i validacija detekcionih modela vršena korišćenjem GEANT4 Monte Karlo transportnog koda. Rezultati ovih istraživanja su objavljeni u radovima:

1. **Sample matrix influence on the efficiency function modeling for uranium isotopes determination by gamma spectrometry**

Autori: A. Vraničar, J. Nikolov, Đ. Lazarević, A. Rikalo, N. Todorović, D. Arbutina, M. Travar
Časopis: *Radiation Physics and Chemistry*, Volume 192, mart 2022; **M21a, IF 2.9**
DOI: [10.1016/j.radphyschem.2021.109891](https://doi.org/10.1016/j.radphyschem.2021.109891)

2. Detailed optimization procedure of an HPGe detector using GEANT4 toolkit

Autori: M. Travar, J. Nikolov, N. Todorović, A. Vraničar,

P. Volgyesi, P. Kirchknopf, I. Čeliković, T. Milanović, D. Joković

Časopis: *Journal of Radioanalytical and Nuclear Chemistry*, Volume 332, 5. mart 2023; **M22, IF 1.5**

DOI: [10.1007/s10967-023-08810-x](https://doi.org/10.1007/s10967-023-08810-x)

ISPITIVANJE NUKLEARNIH PROCESA - KOSMIČKO ZRAČENJE

Dinamika Sunčevog koronalnog magnetnog polja može prouzrokovati složenim kosmičkim događajima. Među ovim događajima su npr. solarne eksplozije ili baklje (SF), koronalna izbacivanja masa (CME), međuplanetarna koronalna izbacivanja masa (ICME), emisija solarnih energetske čestice (SEP), i drugi. Ovi događaji mogu dovesti do raznih negativnih efekata u heliosferi, što posledično utiče i na Zemljinu sredinu.

Generalno, SF i CME mogu izazvati složene promene i poremećaje kako u okviru heliosfere tako i u okviru Zemljine magnetosfere. Kako bi se ovi događaji bolje razumeli moraju se ispitati sve moguće veze između različitih procesa koje ovi fenomeni indukuju. U ovom kontekstu ispitivan je Forbušov pad 4.11.2021. uočen preko raznih detekcionih stanica kosmičkih zraka (uključujući i stanicu u Beogradu) koji je omogućila serija CME događaja u periodu između 28.10.2021. i 4.11.2021. Pored ovoga, ukazano je na mogućnost postojanja dve klase Forbušovog pada prilikom čega je razvijena procedura klasifikacije koja implementira mašinsko učenje u cilju potencijalnog poboljšanja statistike. Detaljno je ispitana veza između povećanog SEP fluksa i svojstava istovremenog Forbušovog pada. Rezultati ovih istraživanja su objavljeni u radovima:

1. Analyzing solar activity with Belgrade muon station: case study of 2021 November 4th Forbush decrease

Autori: N. B. Veselinović, M. B. Savić, D. M. Maletić, A. L. Dragić,

R. M. Banjanac, D. R. Joković, D. Knežević, **M. Travar**, V. I. Udovičić

Časopis: *Contributions of the Astronomical Observatory Skalnaté Pleso*, Vol. 53, 2023; **M23, IF 0.4**

DOI: [10.31577/caosp.2023.53.3.148](https://doi.org/10.31577/caosp.2023.53.3.148)

2. Forbush decrease events associated with coronal mass ejections: Classification using machine learning

Autori: M. B. Savić, N. B. Veselinović, A. L. Dragić, D. M. Maletić,

R. M. Banjanac, D. R. Joković, D. Knežević, **M. Travar**, V. I. Udovičić

Časopis: *Contributions of the Astronomical Observatory Skalnaté Pleso*, Vol. 53, 2023; **M23, IF 0.4**

DOI: [10.31577/caosp.2023.53.3.156](https://doi.org/10.31577/caosp.2023.53.3.156)

3. Further study of the relationship between transient effects in energetic proton and cosmic ray fluxes induced by coronal mass ejections

Autori: M. Savić, N. Veselinović, D. Maričić, F. Šterc, R. Banjanac, **M. Travar**, A. Dragić

Časopis: *Universe*, Volume 10, jun 2024; **M22, IF 2.9**

DOI: [10.3390/universe10070283](https://doi.org/10.3390/universe10070283)

3 ELEMENTI ZA KVALITATIVNU ANALIZU NAUČNOG DOPRINOSA KANDIDATA

3.1 ZNAČAJ NAUČNIH REZULTATA

Miloš Travar se bavio istraživačkim radom u okviru više različitih disciplina nuklearne fizike koje su ukratko opisane zajedno sa značajem rezultata dalje u tekstu. Kao član Niskofonske laboratorije na Institutu za fiziku u Beogradu, glavna oblast istraživanja kandidata predstavljaju Monte Karlo simulacije.

U okviru ove oblasti istraživanja, kandidat je svojevrsno razvio simulacione programske kodove u okviru različitih eksperimentalnih postavki tokom kolaboracija i boravka na više različitih inostranih svetski priznatih instituta u okviru kojih su ovi eksperimenti sprovedeni. Ovim simulacionim modelima i kodovima su pokrivene različite oblasti istraživanja fizike nuklearnih procesa, neke među kojima su fisiona dinamika, γ -spektrometrija, nuklearna bezbednost i forenzika, retrospektivna dozimetrija, itd. Razvijeni simulacioni modeli su korišćeni u svrhu validacije eksperimentalnih rezultata, ali i uspešnog modelovanja i predviđanja eksperimentalno nedostupnih podataka. Ovim istraživanjima su rezultovale naučne publikacije u vrhunskim međunarodnih časopisima ukratko opisane **tačkom 3**.

Pored glavnog pravca svog istraživanja, Miloš Travar je dao svoj doprinos i u drugim naučnim granama nuklearne fizike uključujući nuklearnu bezbednost i forenziku, retrospektivnu dozimetriju, itd. Kao član Niskofonske laboratorije za nuklearnu fiziku na Institutu za fiziku u Beogradu, Miloš je takođe dao svoj doprinos i u oblasti kosmičkog zračenja. Sve svoje naučne rezultate Miloš je svojevrsno prezentovao kako na vrhunskim međunarodnim naučnim skupovima i konferencijama tako i na domaćim skupovima.

3.1.1 PARAMETRI KVALITETA ČASOPISA

Dr Miloš Travar je tokom svoje naučne karijere kao autor i koautor objavio ukupno 7 radova u vrhunskim međunarodnim časopisima. Od prethodnog izbora u zvanje istraživača saradnika (datum izbora 7.2.2022.) Miloš je objavio ukupno 5 radova. Kvalitet objavljenih radova se može između ostalog proceniti i prema kvalitetu časopisa u kojima su ovi radovi objavljeni, a to su:

- 1 rad u istaknutom međunarodnom časopisu: *Nuclear Instruments and Methods in Physics Research Section A: Accelerators, Spectrometers, Detectors and Associated Equipment* (M22, IF 1.335),
- 1 rad u vrhunskom međunarodnom časopisu: *Physics Letters B* (M21, IF 4.95),
- 1 rad u međunarodnom časopisu izuzetnih vrednosti: *Radiation Physics and Chemistry* (M21a, IF 2.9),
- 1 rad u istaknutom međunarodnom časopisu: *Journal of Radioanalytical and Nuclear Chemistry* (M22, IF 1.5),
- 2 rada u međunarodnom časopisu: *Contributions of the Astronomical Observatory Skalnaté Pleso* (M23, IF 0.4),
- 1 rad u istaknutom međunarodnom časopisu: *Universe* (M22, IF 2.9).

Ukupan impakt faktor publikovanih radova kandidata je **14.385**.

	IF	M	SNIP
Ukupno	14.385	39	5.387
Usrednjeno po članku	2.055	5.57	0.77
Usrednjeno po autoru	1.72	4.81	0.66

3.1.2 POZITIVNA CITIRANOST RADOVA KANDIDATA

Prema Scopus bazi podataka ([Scopus link](#)), radovi dr Miloša Travara citirani su 22 puta, od čega 21 put izuzimajući autocitate, sa ukupnim h-indeksom 3.

3.2 NORMIRANJE BROJA KOAUTORSKIH RADOVA, PATENATA I TEHNIČKIH REŠENJA

Svi radovi dr Miloša Travara spadaju u eksperimentalne radove u prirodno-matematičkim naukama tako da se radovi sa 7 koautora uzimaju sa punom težinom, dok se radovi sa više koautora (jedan rad iz međunarodnih časopisa sa 11 i tri rada sa 9 koautora) normiraju po formuli datoj u Pravilniku o postupku i načinu vrednovanja, i kvantitativnom iskazivanju naučno-istraživačkih rezultata istraživača ($K/(1+0.2(n-7))$).

3.3 UČEŠĆA NA PROJEKTIMA, POTPROJEKTIMA I PROJEKTNIM ZADACIMA

Kandidat je u periodu od 2019. do 2023. kao stipendista bio angažovan na projektu pod brojem OI171002 naslova "Nuklearne metode istraživanja retkih događaja i kosmičkog zračenja" Ministarstva prosvete, nauke i tehnološkog razvoja Vlade Republike Srbije, vođen od strane prof. dr Ištvana Bikita.

3.4 UTICAJ NAUČNIH REZULTATA

Značaj objavljenih naučnih rezultata kandidata je detaljno opisan u **tački 4.1**, dok se njihov uticaj ogleda u prilogu o citiranosti opisan u **tački 4.1.2**.

3.5 KONKRETAN DOPRINOS KANDIDATA U REALIZACIJI RADOVA U NAUČNIM CENTRIMA U ZEMLJI I INOSTRANSTVU

Kandidat je svoje naučne aktivnosti realizovao na Prirodno-matematičkom fakultetu Univerziteta u Novom Sadu, Institutu za fiziku u Beogradu, Centre for Energy Research istraživačkom institutu u Mađarskoj ([CER](#), Budimpešta), European Commission Joint Research Centre institutu u Belgiji ([EC-JRC](#), Geel) i European Commission Joint Research Centre institutu u Nemačkoj ([EC-JRC](#), Karlsruhe). Svoj doprinos tokom istraživanja je realizovao i dao u vidu numeričkog računanja, dizajniranja eksperimentalnih postavki, razvijanju simulacija, analizom i interpretacijom rezultata, pisanju radova i komunikaciji sa recenzentima.

3.6 UVODNA PREDAVANJA NA KONFERENCIJAMA, DRUGA PREDAVANJA I AKTIVNOSTI

Tokom studija kandidat dr Miloš Travar je učestvovao na sledećim naučnim skupovima, treninzima, školama i konferencijama kako u zemlji tako i u inostranstvu:

Stručne škole i treninzi:

1. *CERN Masterclass: Overview of LHC data & radiotherapy simulations*; 2018/2023; Novi Sad, Srbija,
2. *THOR: Study of hot matter and heavy ion collisions*; 2020; Jahorina, BiH,

3. **EC-JRC**: *Workshop on γ -spectra evaluation via PC FRAM*; 2021; Novi Sad, Srbija,
4. **EUNPDC**: *WDM Non-proliferation and disarmament pathways*; 2022; Stokholm, Švedska,
5. **CER & ARIEL**: *Study & analysis of nuclear data from research reactors*; 2023; Budimpešta, Mađarska.

Međunarodni skupovi i konferencije:

1. **RAD** - *Seventh International Conference of Radiation in Various Field of Research; ^{210}Pb correction for self-absorption effect in EFFTRAN and Angle softwares* (**M. Travar**, J. Nikolov, N. Todorović, A. Vraničar, J. Hansman, D. Mrđa); Jun 2019, Crna Gora,
2. **RAD** - *Seventh International Conference of Radiation in Various Field of Research; ^{226}Ra n water measurement by non-Marinelli geometry and γ -spectrometry* (**M. Travar**, J. Nikolov, N. Todorović, A. Vraničar, J. Hansman, D. Mrđa); Jun 2019, Crna Gora,
3. **ENVIRA** - *Conference on Environmental Radioactivity Variations of Environmental Radionuclides; Self-absorption effects in low-energy region for non-destructive nuclear forensics method* (J. Nikolov, A. Vraničar, N. Todorović, **M. Travar**, J. Hansman, S. Gadžurić, D. Mrđa); Septembar 2019, Republika Češka,
4. **THEORY5** - *Workshop on Nuclear Fission Dynamics and the Emission of Prompt Neutrons and γ -Rays; An Insight into the future of NICOLE* (**M. Travar**, J. Nikolov, A. Vraničar, R. Grzywacz, M. Madruga, J. R. Stone, N. J. Stone, K. Kolos); Septembar 2019, Italija,
5. **ENVIRA** - *Conference on Environmental Radioactivity Variations of Environmental Radionuclides; Monte Carlo approach for model optimization of HPGe detector* (A. Vraničar, **M. Travar**, N. Todorović, J. Nikolov); Decembar 2021, Grčka,
6. **ENVIRA** - *Conference on Environmental Radioactivity Variations of Environmental Radionuclides; Experimental verification of ANGLE5 software for quantitative γ -spectrometry* (J. Nikolov, A. Vraničar, **M. Travar**, N. Todorović); Decembar 2021, Grčka,
7. **BPUII** - *11th International conference of the Balkan Physical Union; Presentacija pod naslovom HPGe detector optimization by means of Monte Carlo simulations through application of GEANT4 toolkit* (**M. Travar**, J. Nikolov, A. Vraničar, N. Todorović, D. Joković, I. Čeliković, T. Milanović); Avgust 2022, Srbija,
8. **ELISCIR** - *Potential electronic instrumentation for ionizing radiation environments; Experimental verification of ANGLE 5 software for quantitative gamma spectrometry* (A. Vraničar, **M. Travar**, N. Todorović, J. Nikolov); Januar 2023, Srbija,
9. **ELISCIR** - *Potential electronic instrumentation for ionizing radiation environments; Retrospective dosimetry by GEANT4 for possible application in Nuclear Forensics* (**M. Travar**, J. Nikolov, A. Vraničar); Januar 2023, Srbija,
10. **ELISCIR** - *Potential electronic instrumentation for ionizing radiation environments; Development of nuclear forensics capabilities in Serbia* (J. Nikolov, N. Todorović, A. Vraničar, **M. Travar**); Januar 2023, Srbija,
11. **RANC** - *International Conference on Radioanalytical and Nuclear Chemistry; Presentacija pod naslovom Applied retrospective dosimetry in nuclear forensics* (J. Nikolov, **M. Travar**, A. Vraničar, N. Todorović, Z. Arazi, E. Elish, S. Segal, G. Yardeni, E. Gilad, N. Porat, P. Völgyesi, A. Kovacs, A. Klemen, V. Sos, Z. Varga, M. Wallenius, K. Mayer); Maj 2023, Mađarska.

4 ELEMENTI ZA KVANTITATIVNU ANALIZU NAUČNOG DOPRINOSA KANDIDATA

Ostvareni rezultati (*Tabela 1*):

Tabela 1: Ostvareni rezultati.

Kategorija	M bodova po radu	Broj radova	Broj radova za normiranje	Ukupno M bodova	Ukupno M bodova sa normiranjem
M21a	10	1	0	10	10
M21	8	1	1	8	4.44
M22	5	3	1	15	13.57
M23	3	2	2	6	4.29
M34	0.5	11	2	5.5	5.08
M70	6	1	0	6	6
Ukupan broj bodova				50.5	43.38

Poređenje sa minimalnim kvantitativnim uslovima za izbor u zvanje naučni saradnik (*Tabela 2*):

Tabela 2: Minimalni uslovi.

	Minimalno	Ostvareni rezultati	Ostvareni normirani rezultati
Ukupno	16	50.5	43.38
M10+M20+M31+M32+M33+M41+M42	10	39	32.3
M11+M12+M21+M22+M23	6	39	32.3

5 SPISAK NAUČNIH RADOVA MILOŠA TRAVARA

Radovi u međunarodnim časopisima izuzetnih vrednosti (M21a)

1. *Sample matrix influence on the efficiency function modeling for uranium isotopes determination by gamma spectrometry*; A. Vraničar, J. Nikolov, Đ. Lazarević, A. Rikalo, N. Todorović, D. Arbutina, **M. Travar**; *Radiation Physics and Chemistry*, Volume 192, mart 2022;

Radovi u vrhunskim međunarodnim časopisima (M21)

1. *Experimental information on mass- and TKE-dependence of the prompt fission γ -ray multiplicity*; **M. Travar**, V. Piau, A. Göök, O. Litaize, J. Nikolov, A. Oberstedt, S. Oberstedt, J. Enders, M. Peck, W. Geerts, M. Vidali; *Physics Letters B*, Volume 817, 10. jun 2021;

Radovi u istaknutim međunarodnim časopisima (M22)

1. *Testing of EFFTRAN and Angle software in comparison to GEANT4 simulations in gamma spectrometry of cylindrical and noncylindrical sample geometries*; A. Vraničar, J. Nikolov, N. Todorović, I. Maksimović, M. Mladenović, D. Mrđa, **M. Travar**; *Nuclear Instruments and Methods in Physics Research Section A: Accelerators, Spectrometers, Detectors and Associated Equipment*, Volume 986, 11. januar 2021;
2. *Detailed optimization procedure of an HPGe detector using GEANT4 toolkit*; **M. Travar**, J. Nikolov, N. Todorović, A. Vraničar, P. Volgyesi, P. Kirchknopf, I. Čeliković, T. Milanović, D. Joković; *Journal of Radioanalytical and Nuclear Chemistry*, Volume 332, 5. mart 2023;
3. *Further study of the relationship between transient effects in energetic proton and cosmic ray fluxes induced by coronal mass ejections*; M. Savić, N. Veselinović, D. Maričić, F. Šterc, R. Banjanac, **M. Travar**, A. Dragić; *Universe*, Volume 10, jun 2024;

Radovi u međunarodnim časopisima (M23)

1. *Analyzing solar activity with Belgrade muon station: case study of 2021 November 4th Forbush decrease*; N. B. Veselinović, M. B. Savić, D. M. Maletić, A. L. Dragić, R. M. Banjanac, D. R. Joković, D. Knežević, **M. Travar**, V. I. Udovičić; *Contributions of the Astronomical Observatory Skalnaté Pleso*, Volume 53, decembar 2023;
2. *Forbush decrease events associated with coronal mass ejections: Classification using machine learning*; M. B. Savić, N. B. Veselinović, A. L. Dragić, D. M. Maletić, R. M. Banjanac, D. R. Joković, D. Knežević, **M. Travar**, V. I. Udovičić; *Contributions of the Astronomical Observatory Skalnaté Pleso*, Volume 53, decembar 2023;


Saopštenja sa međunarodnih skupova štampano u izvodu (M34)

1. *RAD - Seventh International Conference of Radiation in Various Field of Research; ^{210}Pb correction for self-absorption effect in EFFTRAN and Angle softwares* (**M. Travar**, J. Nikolov, N. Todorović, A. Vraničar, J. Hansman, D. Mrđa); Jun 2019., Crna Gora,
2. *RAD - Seventh International Conference of Radiation in Various Field of Research; ^{226}Ra n water measurement by non-Marinelli geometry and γ -spectrometry* (**M. Travar**, J. Nikolov, N. Todorović, A. Vraničar, J. Hansman, D. Mrđa); Jun 2019., Crna Gora,

3. *ENVIRA - Conference on Environmental Radioactivity Variations of Environmental Radionuclides; Self-absorption effects in low-energy region for non-destructive nuclear forensics method* (J. Nikolov, A. Vraničar, N. Todorović, **M. Travar**, J. Hansman, S. Gadžurić, D. Mrđa); Septembar 2019., Republika Češka,
4. *THEORY - Workshop on Nuclear Fission Dynamics and the Emission of Prompt Neutrons and γ -Rays; An Insight into the future of NICOLE* (**M. Travar**, J. Nikolov, A. Vraničar, R. Grzywacz, M. Madrugá, J. R. Stone, N. J. Stone, K. Kolos); Septembar 2019., Italija,
5. *ENVIRA - Conference on Environmental Radioactivity Variations of Environmental Radionuclides; Monte Carlo approach for model optimization of HPGe detector* (A. Vraničar, **M. Travar**, N. Todorović, J. Nikolov); Decembar 2021., Grčka,
6. *ENVIRA - Conference on Environmental Radioactivity Variations of Environmental Radionuclides; Experimental verification of ANGLE5 software for quantitative γ -spectrometry* (J. Nikolov, A. Vraničar, **M. Travar**, N. Todorović); Decembar 2021., Grčka.
7. *BPU11 - 11th International conference of the Balkan Physical Union; Prezentacija pod naslovom HPGe detector optimization by means of Monte Carlo simulations through application of GEANT4 toolkit* (**M. Travar**, J. Nikolov, A. Vraničar, N. Todorović, D. Joković, I. Čeliković, T. Milanović); Avgust 2022., Srbija,
8. *ELISCIR - Potential electronic instrumentation for ionizing radiation environments; Experimental verification of ANGLE 5 software for quantitative gamma spectrometry* (A. Vraničar, **M. Travar**, N. Todorović, J. Nikolov); Januar 2023., Srbija,
9. *ELISCIR - Potential electronic instrumentation for ionizing radiation environments; Retrospective dosimetry by GEANT4 for possible application in Nuclear Forensics* (**M. Travar**, J. Nikolov, A. Vraničar); Januar 2023., Srbija,
10. *ELISCIR - Potential electronic instrumentation for ionizing radiation environments; Development of nuclear forensics capabilities in Serbia* (J. Nikolov, N. Todorović, A. Vraničar, **M. Travar**); Januar 2023., Srbija,
11. *RANC - International Conference on Radioanalytical and Nuclear Chemistry; Prezentacija pod naslovom Applied retrospective dosimetry in nuclear forensics* (J. Nikolov, **M. Travar**, A. Vraničar, N. Todorović, Z. Arazi, E. Elish, S. Segal, G. Yardeni, E. Gilad, N. Porat, P. Völgyesi, A. Kovacs, A. Klemen, V. Sos, Z. Varga, M. Wallenius, K. Mayer); Maj 2023., Mađarska.

Travar, Miloš

University of Belgrade, Belgrade, Serbia  57219438505  <https://orcid.org/0000-0001-6976-5464>

 Is this you? [Connect to Mendeley account](#) [View more](#)

22

Citations by 21 documents


7

Documents

3

h-index [View h-graph](#)

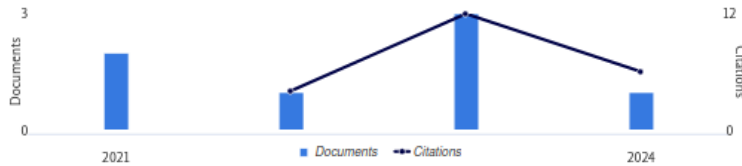
[View all metrics >](#)

 Set alert

 Edit profile

 More

Document & citation trends



[Analyze author output](#) [Citation overview](#)

Most contributed Topics 2019–2023

Monte Carlo Method; Gamma Radiation; Germanium
3 documents

Gamma Radiation; Mass Distribution; Kinetic Energy
1 document

Forbush Decrease; Solar Wind; Interplanetary Medium
1 document

[View all Topics](#)

7 Documents

Author Metrics

New

Cited by 21 documents

1 Preprint

33 Co-Authors

4 Topics

0 Awarded Grants


Beta

21 citations

[Export all](#) [Save all to list](#)

Sort by [Date \(newest\)](#)

[View list in search results format](#)

 Set citation alert

Article

Background radioactivity level estimation and passive shield optimization using adjoint Monte Carlo method

0

Citations

Satti, K.H., Dilband, M., Siddique, M.T., ... Malik, A.H., Mansoor, S.

Applied Radiation and Isotopes, 2024, 212, 111471

[Show abstract](#) [View at Publisher](#) [Related documents](#)

Article

Measurement of fragment-correlated γ -ray emission from Cf 252 (sf)

0

Citations

Marin, S., Tolstukhin, I.A., Giha, N.P., ... Protopopescu, V., Pozzi, S.A.

Physical Review C, 2024, 109(5), 054617

[Show abstract](#) [View at Publisher](#) [Related documents](#)

Article

Semiclassical treatment of photon cascades in nuclei

0

Citations

Randrup, Jø., Døssing, T.

Physical Review C, 2024, 109(5), 054613

[Show abstract](#) [View at Publisher](#) [Related documents](#)

Article

Scission Deformation of the Cd120/Sn132 Neutronless Fragmentation in Cf252(sf)

0

Citations

Francheteau, A., Gaudefroy, L., Scamps, G., ... Ebran, A., Bélier, G.

Physical Review Letters, 2024, 132(14), 142501

[Show abstract](#) [View at Publisher](#) [Related documents](#)

Article

LSC screening of coloured water samples for simultaneous ^{137}Cs and $^{90}\text{Sr}/^{90}\text{Y}$ measurements during nuclear emergencies

2

Citations

Stojković, I., Todorović, N., Nikolov, J., ... Gadžurić, S., Vraneš, M.

Radiation Physics and Chemistry, 2024, 216, 111447

[Show abstract](#) [View at Publisher](#) [Related documents](#)

Article

Irradiation and analysis of Uranyl Nitrate solutions in different Uranium concentrations for use in subcritical reactors for ^{99}Mo production

2

Citations

Putra, F., Syarip, S., Sihana, S.

Nuclear Engineering and Design, 2023, 415, 112701

[Show abstract](#) [View at Publisher](#) [Related documents](#)

Article

Effect of the Coulomb force on fission fragment angular momenta

1

Citations

Randrup, Jø.

Physical Review C, 2023, 108(6), 064606

[Show abstract](#) [View at Publisher](#) [Related documents](#)

- Article - Open access
Examination of how properties of a fissioning system impact isomeric yield ratios of the fragments 1
 Citations
 Gjestvang, D., Wilson, J.N., Al-Adili, A., ... Yavahchova, M., Ziliani, S.
Physical Review C, 2023, 108(6), 064602
[Show abstract](#) [View at Publisher](#) [Related documents](#)
- Article
Prompt emission calculations for $^{252}\text{Cf}(\text{SF})$ focused on post-neutron fragment distributions and different correlations between pre- and post-neutron fragment quantities 2
 Citations
 Tudora, A.
European Physical Journal A, 2023, 59(11), 283
[Show abstract](#) [View at Publisher](#) [Related documents](#)
- Article
Application of Geant4 simulation in measurement of cosmic-ray muon flux and studies of muon-induced background 1
 Citations
 Joković, D., Maletić, D., Dragić, A., ... Banjanac, R., Knežević, D.
European Physical Journal Plus, 2023, 138(11), 1006
[Show abstract](#) [View at Publisher](#) [Related documents](#)
- Article
Determination of detection efficiency on HPGe detector for point-like and volumetric samples based on Geant4 simulations 0
 Citations
 Lin, M., Wang, Y., Qin, Z.
Applied Radiation and Isotopes, 2023, 200, 110989
[Show abstract](#) [View at Publisher](#) [Related documents](#)
- Article - Open access
TALYS calculations of prompt fission observables and independent fission product yields for the neutron-induced fission of ^{235}U 5
 Citations
 Fujio, K., Al-Adili, A., Nordström, F., ... Chiba, S., Koning, A.
European Physical Journal A, 2023, 59(8), 178
[Show abstract](#) [View at Publisher](#) [Related documents](#)
- Article - Open access
Instrumentation for correlated prompt n- γ emission studies in coincidence with fission fragments 1
 Citations
 Marin, S., Tolstukhin, I.A., Giha, N.P., ... Pozzi, S.A., Tovesson, F.
Nuclear Instruments and Methods in Physics Research, Section A: Accelerators, Spectrometers, Detectors and Associated Equipment, 2023, 1048, 168027
[Show abstract](#) [View at Publisher](#) [Related documents](#)
- Article
Characterization of the thickness of dead layer and cold finger for portable HPGe γ -spectrometer 1
 Citations
 Wu, Z., Wang, B., Sun, J.
Radiation Physics and Chemistry, 2023, 204, 110665
[Show abstract](#) [View at Publisher](#) [Related documents](#)
- Article - Open access
Neutron and gamma multiplicities calculated in the consistent framework of the Hauser-Feshbach Monte Carlo code FIFRELIN 8
 Citations
 Piau, V., Litaize, O., Chebboubi, A., ... Gök, A., Oberstedt, A.
Physics Letters, Section B: Nuclear, Elementary Particle and High-Energy Physics, 2023, 837, 137648
[Show abstract](#) [View at Publisher](#) [Related documents](#)
- Conference Paper - Open access
The role of angular momentum in fission 0
 Citations
 Vogt, R., Randrup, J.
16th Varenna Conference on Nuclear Reaction Mechanisms, NRM2023, 2023, 08006
[Show abstract](#) [View at Publisher](#) [Related documents](#)
- Book Chapter
Prompt and Delayed Emission 0
 Citations
 Devlin, M., Gök, A., Serot, O., Talou, P., Vogt, R.
Nuclear Fission: Theories, Experiments and Applications, 2023, pp. 263-400
[Show abstract](#) [View at Publisher](#) [Related documents](#)
- Article - Open access
Probing fission fragment angular momenta by photon measurements 13
 Citations
 Randrup, J., Døssing, T., Vogt, R.
Physical Review C, 2022, 106(1), 014609
[Show abstract](#) [View at Publisher](#) [Related documents](#)

Review · [Open access](#)

Gamma-ray spectroscopy of fission fragments with state-of-the-art techniques

12

Citations

Leoni, S., Michelagnoli, C., Wilson, J.N.

Rivista del Nuovo Cimento, 2022, 45(7), pp. 461–547

[Show abstract](#) [View at Publisher](#) [Related documents](#)

Article · [Open access](#)

Directional dependence of the event-by-event neutron- γ multiplicity correlations in Cf 252 (sf)

8

Citations

Marin, S., Sansevero, E.P., Okar, M.S., ... Protopopescu, V.A., Pozzi, S.A.

Physical Review C, 2022, 105(5), 054609

[Show abstract](#) [View at Publisher](#) [Related documents](#)

Article

Sample matrix influence on the efficiency function modeling for uranium isotopes determination by gamma spectrometry

1

Citations

Vraničar, A., Nikolov, J., Lazarević, D., ... Arbutina, D., Travar, M.

Radiation Physics and Chemistry, 2022, 192, 109891

[Show abstract](#) [View at Publisher](#) [Related documents](#)



Природно-математички факултет
Универзитет у Новом Саду

Трг Доситеја Обрадовића 3, 21000 Нови Сад, Србија

тел 021.455.630 факс 021.455.662 e-mail dekanpmf@uns.ac.rs web www.pmf.uns.ac.rs

ПИБ 101635863 МБ 08104620

УНИВЕРЗИТЕТ У НОВОМ САДУ
ПРИРОДНО-МАТЕМАТИЧКИ ФАКУЛТЕТ
Изборно веће Департмана за физику
Нови Сад, Трг Доситеја Обрадовића 3

Број: 02-14/9

Датум: 07.02.2022.

На основу члана 14. Правилника о поступку стицања истраживачких и научних звања на Природно-математичком факултету Универзитета у Новом Саду (пречишћен текст) број: 0601-208/9, од 27.08.2019. године, Изборно веће Департмана за физику Природно-математичког факултета у Новом Саду, на 6. седници одржаној **07. фебруара 2022. године**, донело је следећу

О Д Л У К У

Милош Травар бира се у истраживачко звање **истраживача сарадник** за област науке: **Природно-математичке науке**, грана науке: **Физика**, научна дисциплина: **Физика високих енергија (физика елементарних честица, нуклеарна физика, акцелератори и снопови, радијациона физика)** на Департману за физику Природно-математичког факултета у Новом Саду.

О б р а з л о ж е њ е

Милош Травар, дана 22. новембра 2021. године упутила је Изборном већу Департмана за физику предлог за покретање поступка бирања звања истраживача сарадника.

Изборно веће Департмана за физику, на предлог Већа Департмана за физику, на својој 3. седници одржаној дана 30. новембра 2021. године формирало је комисију за припрему извештаја.

Извештај комисије био је стављен на увид јавности, на начин утврђен општим актима Факултета и Универзитета у Новом Саду.

Чланом 14 Правилника о поступку стицања истраживачких и научних звања на Природно-математичком факултету Универзитета у Новом Саду, дефинисано је да је Изборно веће одговарајућег департмана, као Научно веће у складу са чланом 69. став 2. Статута Природно-математичког факултета, орган који доноси одлуку о избору у звање истраживача сарадника.

На основу свега изнетог донета је Одлука као у диспозитиву.

ПРЕДСЕДНИК ИЗБОРНОГ ВЕЋА
ДЕПАРТМА НА ФИЗИКУ

Проф. др Зоран Мијатовић

Доставити:

1. Кандидату;
2. Служби општих послова Факултета;
3. Архиви Департмана.



Природно-математички факултет
Универзитет у Новом Саду

Трг Доситеја Обрадовића 3, 21000 Нови Сад, Србија

тел 021.455.630 факс 021.455.662 e-mail dekan@pmf.uns.ac.rs web www.pmf.uns.ac.rs

ПИБ 101635863 МБ 08104620

Број: 0603-268/21-8
Датум: 12.8.2024.

ПОТВРДА

Којом се потврђује од стране Природно-математичког факултета у Новом Саду да је **Милош Травар**, дана 9.8.2024. године одбранио докторску дисертацију под насловом „**Верификација симулационих техника у изучавању нуклеарних процеса**“ и стекао научни степен доктор наука – физичке науке.

Уверење о одбрањеној докторској дисертацији биће издато након усвајања Извештаја о одбрани на седници Наставно-научног већа Факултета.

Потврда се издаје на лични захтев именованог.

ДЕКАН
Природно-математичког факултета
Др Милица Павков Хрвојевић, редовни професор





Contents lists available at ScienceDirect

Nuclear Inst. and Methods in Physics Research, A

journal homepage: www.elsevier.com/locate/nima

Testing of EFFTRAN and Angle software in comparison to GEANT 4 simulations in gamma spectrometry of cylindrical and noncylindrical sample geometries



Andrej Vraničar^a, Jovana Nikolov^{a,*}, Nataša Todorović^a, Ivana Maksimović^b,
Miloš Mladenović^b, Dušan Mrđa^a, Miloš Travar^a

^a University of Novi Sad, Faculty of Sciences, Trg Dositeja Obradovića 3, 21000 Novi Sad, Serbia

^b Public Company Nuclear Facilities of Serbia, PO Box 4, 11000 Belgrade, Serbia

ARTICLE INFO

Keywords:

Semi-empirical efficiency transfer method

Simulation method

Gamma spectrometry

Nuclear and other radioactive materials

ABSTRACT

Being able to accurately determine the efficiency of detection, in respect of having precise measurements of radioactivity, represents one of the main objectives of every gamma spectrometry laboratory. In standard gamma spectrometry practice, activities of low-energy emitters can prove to be difficult for measurement. Gamma spectrometry is often used as an initial monitoring tool to determine basic parameters of the unknown sample found in the field, especially when it is suspected that this material can be a part of illicit trafficking involving radioactive materials. The main concern in most cases is uranium, as one of its isotopes (^{235}U) can be used in the production of a nuclear bomb. Gamma spectrometry is the most applicable, non-destructive technique used in a nuclear forensic investigation for uranium isotopic composition analysis.

The main idea of this paper was to test the advantages and disadvantages of semi-empirical methods by using two software (EFFTRAN and Angle) and simulation method in GEANT 4 applied on samples containing uranium and thorium isotopes. Special attention was devoted to non-cylindrical sample geometries. The general purpose of the presented study was to investigate the possibilities of routine gamma spectrometry laboratory to be able to respond to a nuclear security event.

Based on the obtained results, general recommendations for the use of semi-empirical and simulation methods are given.

1. Introduction

Being recognized as one of the main challenges in low-energy gamma spectrometry (energies below 200 keV), accurately determining the efficiency of detection in this region proves to be of crucial importance to produce precise results for activity concentration of uranium isotopes.

One of the possible applications of gamma spectrometry is as a non-destructive technique for nuclear forensics purposes. The phenomenon of nuclear smuggling and illicit trafficking of nuclear material has led to the development of nuclear forensics. As a relatively young scientific discipline, nuclear forensics represents a way to use knowledge and skills from the domain of nuclear physics and implement them to help authorities in criminalistic investigations [1]. Samples of interest for nuclear forensics may serve as evidence for an ongoing investigation, hence a non-destructive method such as gamma-spectrometry is at all times the preferential choice [2]. In the case of special nuclear material containing uranium, gamma spectrometry can be used for

the determination of total nuclear material content, the age of the material (time past since last enrichment), the presence of reprocessed uranium, and the presence of fission products. In addition to this, being a non-destructive method for sample analysis, laboratory applications of gamma-spectrometry for purposes of nuclear forensics provide means to accurately determine the isotopic composition of gamma-emitting radionuclides in a sample and to quantify the amount of each radioisotope present [3].

Uranium is a naturally occurring rare earth element that is found in Earth's crust with an average presence of 3 ppm. Natural uranium is a mixture of three radioactive isotopes ^{238}U (99.27% abundance), ^{235}U (0.72% abundance) and ^{234}U (0.0054% abundance) [4]. The majority of the most intensive gamma-lines that are emitted from all uranium isotopes lie in the low-energy part of the gamma spectrum. This energy region presents a challenge in any gamma spectrometric analysis. In order to obtain any information about radionuclide from the gamma spectrum, the main prerequisite must be fulfilled, and that is having

* Corresponding author.

E-mail address: jovana.nikolov@df.uns.ac.rs (J. Nikolov).

<https://doi.org/10.1016/j.nima.2020.164768>

Received 6 July 2020; Received in revised form 12 October 2020; Accepted 12 October 2020

Available online 15 October 2020

0168-9002/© 2020 Elsevier B.V. All rights reserved.

an accurate reading for the count rate from the lower end part of the spectrum. This can prove to be difficult for mainly two reasons, line positioning in the area which naturally has a substantial background and poorly (inadequately) defined function of detection efficiency for this energy range. One of the reasons for the latter could be if the self-absorption effects of the low-energy gammas in the sample are not quantified. Given what is stated, one of the main problems in low-energy gamma spectrometry is accurately determining the function of the efficiency of detection in this region and it proves to be of crucial importance to produce precise results for the activity concentration of uranium.

The samples found in the field are in most cases irregular in shape — non-cylindrical, and if we want to keep the sample undamaged for further analysis we cannot change its shape and constitution. In regular gamma spectrometry laboratory calibration of germanium detectors is usually done for the cylindrical geometry of the sample. In order to be able to use those calibrations for any sample that is not necessarily cylindrical, a satisfyingly good approximation of its geometry must be created. Also the density, composition, and radionuclide content of the samples found in the field may vary and it is not easy to find an adequate approximation that is needed in mathematical calculations of detection efficiency.

A typical gamma-spectrometry laboratory is dealing with limited resources in routine practice. There are automatic, commercial software available for the characterization of suspicious nuclear material found in the field like MGAU, MGAU++ (Multi-Group Analysis for Uranium), PC FRAM [5–7]. That software is dealing with the analysis of the gamma spectra using multiplet deconvolution functions. But, from the other side, having in mind that analysis of nuclear and other radioactive material for nuclear forensics needs is not that often, it is of great importance to test also the capabilities and limitations of available mathematical calculation codes (EFFTRAN, ANGLE, and similar) for efficiency determination that could be used for further more precise experimental analysis of gamma spectra. Those mathematical codes are not devoted only to uranium and/or plutonium content analysis and therefore are more commonly found in gamma spectrometry laboratory. With the adequate adjustment, efficiency transfer mathematical calculation codes could give acceptable results for activity concentration of radioisotopes present in the sample of interest.

In a number of studies that are focused on the impact of different samples matrices, densities, and composition in cylindrical sample geometries on efficiency determination, it was concluded that currently available mathematical calculation codes for efficiency transfer gave substantial deviations in resulting activity concentrations for radionuclides in the lower energy region [8–10]. The idea of this paper is to test the applicability of two semi-empirical methods (by using EFFTRAN and Angle software) in comparison to the simulation method (GEANT 4) for analysis of samples of both, non-cylindrical and cylindrical, geometry by carefully defining the shape of the sample more precisely. This study was conducted on the samples that contain uranium and/or thorium isotopes. The general purpose of this study was to investigate the possibilities of routine gamma spectrometry laboratory to be able to respond to a nuclear security event.

2. Materials and methods

2.1. Detector

In this study, an extended range closed-end coaxial HPGe Canberra GX10021 ultra-low background detector was used. The detector has an active volume of 380 cm³ and a 100% relative detection efficiency. Its end-cap is 0.89 mm thick and is made of a high-strength carbon fiber composite, which provides greater than 85% transmissions for photon energy above 15 keV and nearly 100% transmissions for photons with energies above 20 keV [11]. It has a 1.4 keV at 122 keV and 2.0 keV at

1332 keV energy resolution [8]. Count rates are 0.05–46 cps depending on the sample.

The HPGe detector Canberra GX10021 is placed in a commercial ultra low-background passive bulk lead shielding. The manufacturer's mark of the shielding is Canberra model 777B. The total mass of this shielding is 1633 kg. The thickness of the lead in the shielding is 15 cm. The outer 125 mm of the shielding is made of low-background lead, while the innermost 25 mm are made of selected lead with ²¹⁰Pb content of 20 Bq kg⁻¹. The thickness of the inner lead layer is enough to stop the bremsstrahlung from the outer lead volume. Model 777B has an additional inner layer of low background tin (1 mm) and high purity copper (1.5 mm). Tin is used to stop the lead K-shell x rays with energies 75–85 keV. The copper is used to stop the tin K-shell x rays with energies 25–28 keV.

The counting system consists of the HPGe detector (combined with the pre-amplifier), a high-voltage supply system (4.5 kV), an amplifier, and a Multi-Channel Analyser system connected to a PC.

Spectrum analysis was done with GENIE 2000 software. It contains multiple packages, but in this work, Gamma Analysis Software and Interactive Peak Fit packages were used. Gamma Analysis Software is a package that contains a set of advanced algorithms for gamma spectrum analysis that are acquired by GENIE 2000 software. Interactive Peak Fit is a package that provides various tools for analyzing peaks in a given spectrum. This package is useful when acquiring complex spectrums, because of its capability of singlet or multiplet peak analysis, independently of the rest of the spectrum. It also provides the user with an option to manually fit any gamma peak (singlet or multiplet).

2.2. Samples

Sample 1: Sample 1 (Fig. 1) is a uranium dioxide (UO₂) pellet. It is cylindrical in shape, with a diameter of 11.2 mm and a height of 15.1 mm and placed within a glass test-tube container with a wall thickness of 1 mm. It was placed horizontally on the detector cap and measured. Spectra acquisition time was 7.5·10⁴ s. Due to the fact that EFFTRAN and Angle software are designed to work only with vertical axially-symmetrical cylindrical sample geometry, there is a need to define an approximate equivalent sample geometry which means to “make” any irregular sample geometry as close to cylindrical shape as possible. In this way, a certain uncertainty is introduced that cannot be easily estimated and it is neglected in further calculations as we used the same equivalent sample geometry in both software that was compared. Only in GEANT 4, there is no need for approximation with equivalent sample geometry as the shape of the sample could be defined with details. The sample was defined as a cylinder with a diameter of 18.33 mm and a height of 5.6 mm. It was approximated that the equivalent cylinder base surface was equal to half of the UO₂ pellet shell and the height was calculated based on the assumption that the UO₂ pellet and the effective cylinder have the same volume. The sample matrix was taken to be UO₂ with a density of 10.96 g cm⁻³.

Sample 2: Sample 2 is IAEA reference material, uranium ore (IAEA-RGU-1) [12], packed in a horizontally placed 1 mm wall thickness HDPE vial with a diameter of 27 mm and a height of 48 mm. Equivalent sample geometry was a cylinder with a diameter of 42.29 mm and a height of 18.4 mm. Spectra acquisition time was 8.3·10⁴ s. An effective cylinder base surface was taken to be the cross-section of a horizontally placed vial (Fig. 2) and the height was calculated based on the assumption that the U-ore horizontal vial and the effective cylinder have the same volume. Sample 2 was also packed in a standard cylindrical geometry (Fig. 3) with a diameter of 69 mm and a height of 60 mm. Sample matrix was taken to be soil-like with a measured density of (1.23 ± 0.05) g cm⁻³. Sample 2 has a reference value for activity concentration of ²³⁸U of (4.94 ± 0.49) kBq kg⁻¹.

Sample 3: Sample 3 (Fig. 4) is a metallic iron sheet, originating from an airplane engine with a high ²³²Th content. It has a uniform thickness of 2 mm, and is irregular in shape, approximately 32 by

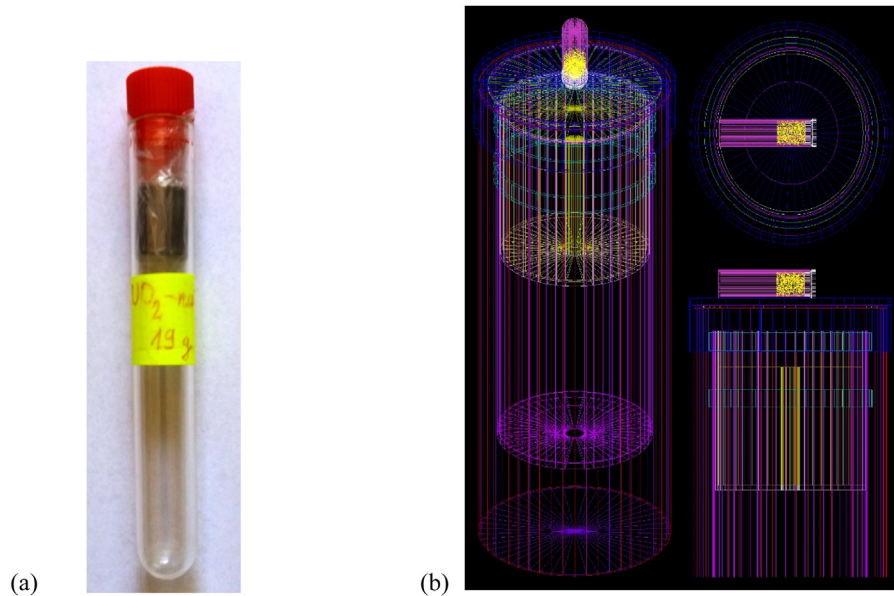


Fig. 1. (a) Sample 1 uranium dioxide pellet, (b) Sample 1 placed on detector obtained by GEANT 4.

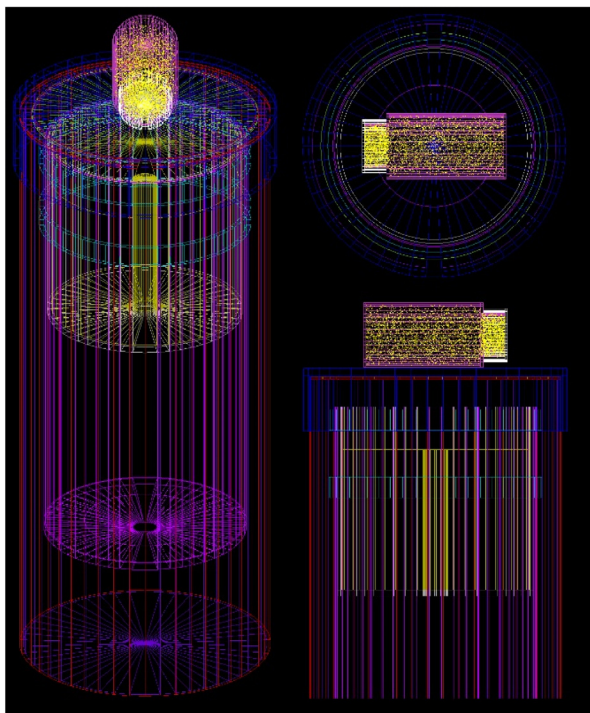


Fig. 2. Sample 2 reference material in vial placed on detector obtained by GEANT 4.

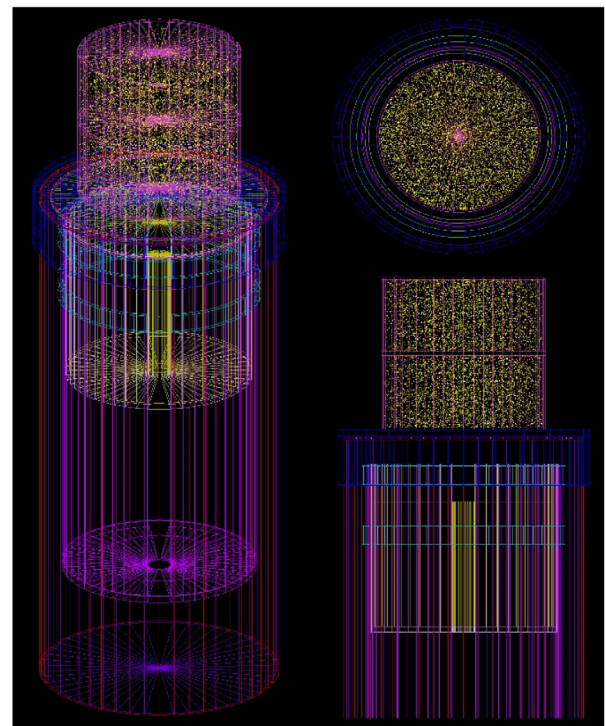


Fig. 3. Sample 2 reference material in cylindrical geometry placed on detector obtained by GEANT 4.

38 mm. Equivalent sample geometry was a cylinder with a diameter of 39.36 mm and a height of 2 mm. Spectra acquisition time was $7.9 \cdot 10^4$ s. An effective cylinder base surface was taken to be the surface of the irregular metal plate, considering it was a square. The sample matrix was taken to be Fe with a density of 7.874 g cm^{-3} packed in an HDPE container with a wall thickness of 1 mm.

2.3. Calculations

To calculate appropriate efficiency functions Angle and EFFTRAN software were used.

Angle is an advanced efficiency calculation application for High Purity Germanium and Sodium Iodide detectors based on the concept of Efficiency Transfer. This method combines the measured efficiency of a known reference configuration and solid angle models to derive the efficiency for different containers, sample materials, and sample positions. This semi-empirical approach is more accurate than pure mathematical models due to large errors that can be imposed by detector characteristics that are not precisely known – such as crystal defects, contact thickness, and dead layers – as these errors cancel out in the reference efficiency measurement. And, since the reference efficiency can be determined from any standard source, there is no need

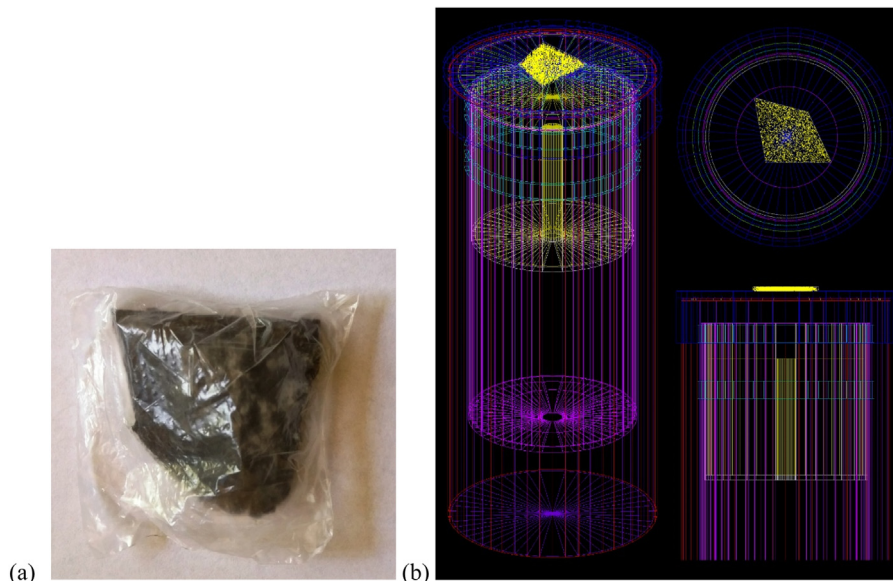


Fig. 4. (a) Sample 3 - metallic iron sheet, (b) Sample 3 placed on detector obtained by GEANT 4.

for complex and costly factory characterization of the detector [13]. The very concept that is behind the code is well described in the paper of Jovanovic et al. [14]. Angle software does not include the corrections for the effects of true coincidence summing.

EFFTRAN is a mathematical software code which is written in Fortran 77 and runs on the Windows platform through a Microsoft Excel interface by using some of its Visual Basic Application (VBA) features [15]. It represents an implementation of the efficiency transfer method for cylindrical samples in gamma-ray spectrometry, based on a Monte Carlo integration of the interaction probabilities of gamma rays throughout the detector and sample volumes. This approach makes it possible for the computer code to be relatively straightforward to write and the speed of the calculation to be adequate for routine on-line analysis of gamma-ray spectra. The mechanism of this method is calculating the ratio of the total efficiencies for the sample of interest and the calibration sample and by multiplying it with the measured Full Energy Peak Efficiency (FEPE) of the latter [16]. A major advantage of the method, as pointed out and verified by its founders, is that in the calculated ratio many inaccuracies in the detector model can be expected to cancel out to a large degree, making it possible to work directly with non-optimized detector data supplied by the manufacturer. The cancellation of differences also applies to the interaction cross-section data that different implementations of the ET method may use and to their physical models of particle interaction and tracking. EFFTRAN software also has the ability to calculate true coincidence summing correction factors for a given radionuclide in a corresponding sample and detector geometry [15]. During the calculation of these factors, gamma-gamma, gamma-X-ray, and X-ray-X-ray coincidences are taken into account. After the calculation, true coincidence summing correction factors are used to multiply the net peak area with them. EFFTRAN software automatically calculates correction factors for true coincident summing effects, based on a sample geometry, detector model, and radionuclide of interest input.

In the majority of the gamma lines of considered radionuclides in analyzed samples, the obtained true coincidence summing correction factors that are calculated by EFFTRAN software are close to 1 and therefore the difference from obtained Angle values is generally smaller than 8%. So, in this case, the coincidence summing correction factors were not of great importance for obtaining the final results.

Angle and EFFTRAN software both rely on a process called efficiency transfer to calculate the unknown efficiency on a given sample. The procedure of acquiring the detection efficiency for an unknown

sample is well described in Ref. [8]. The efficiency transfer method is carried out according to the equation:

$$\varepsilon = \varepsilon_{ref} \frac{\eta}{\eta_{ref}} \quad (1)$$

Here, full-energy-peak efficiencies are designated by ε and total efficiencies by η . Quantities without labels refer to the volume sample and those labeled “ref” to the calibration reference source geometry. The two total efficiencies are computed by the code and the reference source full energy-peak efficiency has to be measured. The result of the method is the required full-energy peak efficiency of the volume source. To be able to calculate these total efficiencies, a detailed model of the detector must be constructed.

In order to get accurate results of gamma spectrometry measurements, it is of great importance that the efficiency of a detector gets precisely calculated for different energies, source geometries, and matrices, either with the help of a source standard with known activities of radionuclides where there is no need for approximations or by using a designated software for numerical or semi-empirical calculations. Therefore, efficiency calibration is an intrinsic part of any measurement dealing with detectors with parameter-specific efficiencies. After the spectra are measured, the reference efficiency calculation process can be approached. First, after measuring a well-defined source with known activity, a peak selection is made from which activity analysis is done for specific radionuclides. Then, efficiency can be derived from the following formula:

$$\varepsilon_{ref} = \frac{N}{t \cdot p_{\gamma} \cdot A} \quad (2)$$

In this formula, N stands for the total number of detected gamma photons, t is the collection time, p_{γ} is the probability of emission of a photon at a given energy, and A is the activity of a radionuclide with the decay correction. Reference efficiency curves can be calculated for reference material, for different detectors, sample geometries, and matrices. Knowing that detector, sample, and standard specifications, EFFTRAN and Angle software can give us the desired efficiency values for our measured sample.

As reference material for all calculations, we used certified Czech Metrology Institute standard type CBSS 2, which contains a mixture of various radionuclides, for an energy interval of 59–1846 keV. These radionuclides are implanted in a silicon resin with known composition and a density of 0.985 g cm^{-3} . The standard material was packed in a cylindrical geometry with a diameter of 70 mm and a height of 69 mm.

Comparing to the semi-empirical method, for the simulation method there is no need to have reference material at all. Therefore, the simulation method is tested with the same group of samples.

Monte Carlo simulation, based on GEANT 4 simulation package [17], has been developed to obtain the response of germanium detectors, with the aim to reproduce experimental spectra of detectors in a wide range of applications in gamma spectroscopy measurements [18, 19]. GEANT 4 allows the description of an experimental setup represented by a structure of geometrical volumes filled by given materials and associated with tracking media. In the simulation, germanium detectors, together with the whole detector assembly, are constructed in great detail, according to the manufacturer's data specifications. In the present work, the GEANT 4 software (version 4.9.5.) [17] was used to obtain the detection efficiencies for different geometries of voluminous sources placed in front of the HPGe detector (Figs. 1–4). In order to perform the simulations, the detector was modeled taking into account the technical features obtained from the manufacturer, except for the central void, whose size parameters were estimated [20]. For each gamma energy, 10^6 photons were generated isotropically from a certain source. The elemental composition, as well as density of the source matrices, were taken into account in simulations. The photopeak efficiency for each gamma energy was found as the ratio of the number of photons detected under photo-peak of given energy and the number of generated photons. The GEANT 4 standard electromagnetic package was applied in the simulations with the following MC simulation parameters: 1000 nm for tracking cut and 990 eV for energy cut.

The activity of the sample was calculated using the following equation:

$$A = \frac{N}{t \cdot p_\gamma \cdot \epsilon} \quad (3)$$

The combined relative measurement uncertainty for calculated sample activity using EFFTRAN and Angle software, $u(A)$ was obtained according to the following equation:

$$u(A) = \sqrt{(\delta\epsilon)^2 + (\delta N)^2} \quad (4)$$

where $\delta\epsilon$ represents relative uncertainty of the efficiency function fit combined with the relative uncertainty of the radioactive solution of the secondary reference material and the uncertainty introduced in the process of production of the secondary reference material given by the manufacturer, used in efficiency transfer method, δN is the relative counting uncertainty. The uncertainties introduced via t and p_γ are negligible. Relative measurement uncertainty $u(A)$ for all energies did not exceed 10% at 2σ level of confidence level.

In GEANT 4, during the calculation of measurement uncertainty, the following assumption was taken into account. The main variables that have been input into the simulation are 9 characteristic dimensions of the detector (crystal diameter and length, crystal cavity diameter and length, top and side dead layer, end-cap diameter, window thickness, and window to crystal gap) and 4 characteristics related to the sample (sample volume, sample and container material, namely density and chemical composition, and container to detector window gap). For these variables, except the chemical composition of sample and container, the uncertainty can be estimated to be 1% for the geometry of crystal and container to detector window gap and 10% for window thickness and window to crystal gap. To minimize the discrepancy between simulated and measured values, bulletization, dead layer, and window to crystal gap was varied in the simulation, and the uncertainty was lowered to an estimated 1%. The chemical composition of the container is well defined, but for the sample, the situation is more complicated, and inadequate knowledge of the chemical composition of uranium ore, metallic plate, and UO_2 pellet can be the source of larger uncertainty. This is estimated to be 10% [20]. Regarding simulation, the relative uncertainty $u_{simulation}$ was calculated according to the following equation:

$$u_{simulation} = \sqrt{\sum (\delta x_i)^2} \quad (5)$$

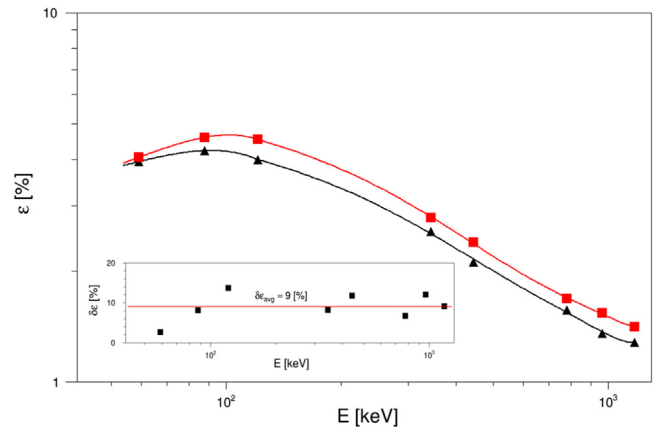


Fig. 5. Efficiency curves for experimental and simulated (with appropriate adjustment of detector characteristics) certified reference material CBSS 2.

where δx_i stands for the relative uncertainty of the value. In the calculation of the relative measurement uncertainty of the simulation, the variable x_i represents the Full Energy Peak Efficiencies (FEPE) that was individually simulated within GEANT 4 code for the each energy, whereas δx_i represents the relative deviation of FEPE values calculated from simulation runs with different number of generated events per run. The optimum number of events per run which yields good statistics with favorable uncertainty was found to be 10^6 events per run, while keeping this uncertainty in the range of the mentioned 5%. Taking into account what is stated, the overall uncertainty of the simulated results is estimated to be 5%.

3. Results and discussion

The results obtained by two efficiency transfer software (Angle and EFFTRAN) and simulation method (GEANT 4) are presented in the form of activity concentrations on a selected group of energies (Tables 1–4). In this work the efficiency transfer method was implemented in GEANT 4 simulation code on the following way: the manufacturer characteristics of the detector were used with additional geometry adjustment (such as the thickness of dead layers, crystal distance from the window, etc.) with a goal to validate simulation results. The measured and simulated efficiency curves of the certified reference material CBSS 2 are presented in Fig. 5. The relative uncertainty for a full spectrum range falls under 15%. The adjusted detector characteristics were then used for all further calculations for investigated samples.

The activity concentration of the ^{238}U was calculated from 63.3 keV line originating from ^{234}Th and 1001.03 keV line originating from $^{234\text{m}}\text{Pa}$, due to the least interference from other gamma lines in spectra. The activity concentration of the ^{235}U was calculated from 143.8 keV and 163.3 keV gamma line (Tables 1–3).

For ^{232}Th the energy lines 238.6 keV and 338.3 keV were used to test the methods (Table 4).

The activities calculated for a given sample geometry using EFFTRAN, Angle, and GEANT 4 software were obtained from the same spectrum.

A comparison of the obtained results for lower energies is given in Figs. 6–10. For Samples 1 and 3 the correct value is unknown so to test methods we used average value with appropriate deviation. Sample 2 is reference material and activities of all containing radioisotopes are known, so we used reference value as a true value.

From the results for Sample 2 in different geometries presented in Table 2 and Fig. 7, as well as Table 3 and Fig. 8 it can be seen that both, semi-empirical and simulation, methods gave satisfying results—good agreement with the average value. Therefore, the total activity concentration is also calculated both for Sample 1 and for Sample 2 in

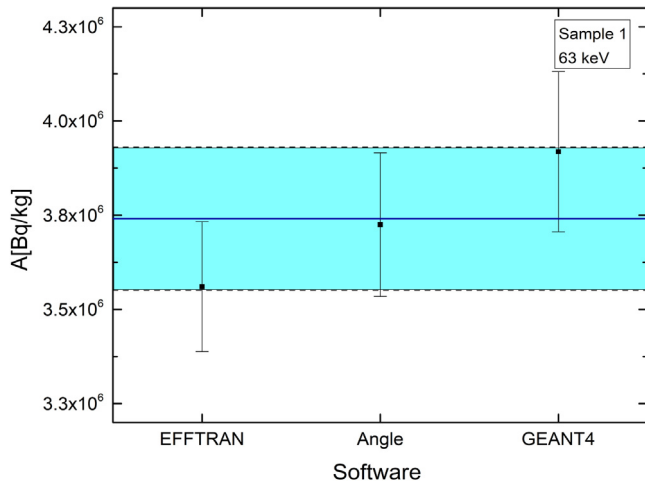


Fig. 6. Activity concentrations on 63.3 keV obtained by different methods for Sample 1.

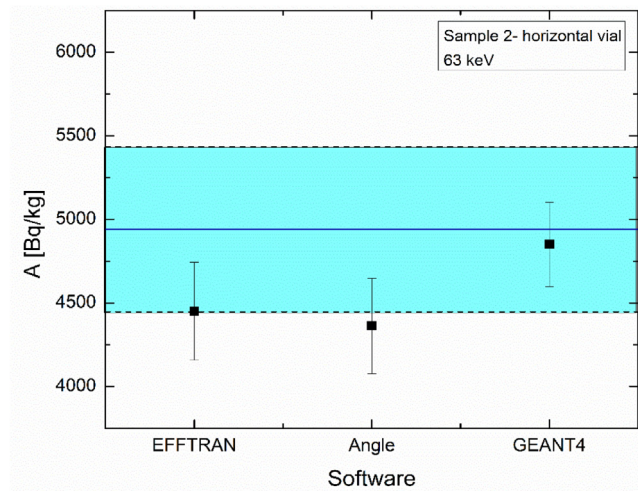


Fig. 7. Activity concentrations on 63.3 keV obtained by different methods for Sample 2 in a horizontal vial.

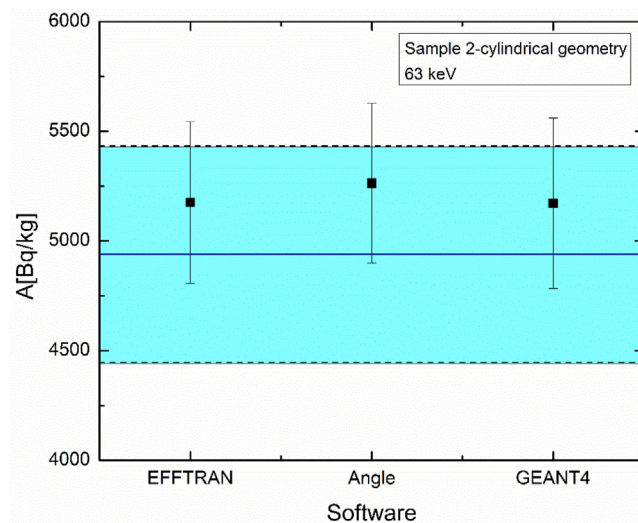


Fig. 8. Activity concentrations on 63.3 keV obtained by different methods for Sample 2 in cylindrical geometry.

Table 1
Activity concentrations for Sample 1 obtained by semi-empirical and simulation methods.

Software	Energy [keV]	Activity concentration [MBq kg ⁻¹]
EFFTRAN	63.3	3.56 ± 0.17
	143.8	0.233 ± 0.014
	163.3	0.245 ± 0.016
	1001.03	5.68 ± 0.24
Angle	63.3	3.73 ± 0.19
	143.8	0.195 ± 0.013
	163.3	0.234 ± 0.015
	1001.03	5.38 ± 0.81
GEANT 4	63.3	3.94 ± 0.21
	143.8	0.213 ± 0.014
	163.3	0.219 ± 0.014
	1001.03	5.79 ± 0.87

Table 2
Activity concentrations for Sample 2 in horizontal vial geometry obtained by semi-empirical and simulation methods.

Software	Energy [keV]	Activity concentration [kBq kg ⁻¹]
EFFTRAN	63.3	4.45 ± 0.29
	143.8	0.424 ± 0.018
	163.3	0.266 ± 0.015
	1001.03	4.51 ± 0.26
Angle	63.3	4.36 ± 0.28
	143.8	0.382 ± 0.019
	163.3	0.254 ± 0.021
	1001.03	4.37 ± 0.25
GEANT 4	63.3	4.85 ± 0.31
	143.8	0.386 ± 0.018
	163.3	0.251 ± 0.015
	1001.03	5.34 ± 0.29

Table 3
Activity concentrations for Sample 2 in cylindrical geometry obtained by semi-empirical and simulation methods.

Software	Energy [keV]	Activity concentration [kBq kg ⁻¹]
EFFTRAN	63.3	5.17 ± 0.24
	143.8	0.242 ± 0.019
	163.3	0.249 ± 0.021
	1001.03	5.23 ± 0.26
Angle	63.3	5.26 ± 0.25
	143.8	0.248 ± 0.018
	163.3	0.266 ± 0.022
	1001.03	5.28 ± 0.27
GEANT 4	63.3	5.17 ± 0.26
	143.8	0.193 ± 0.018
	163.3	0.204 ± 0.015
	1001.03	5.23 ± 0.28

Table 4
Activity concentrations for Sample 3 obtained by semi-empirical and simulation methods.

Software	Energy [keV]	Activity concentration [10 ⁵ Bq kg ⁻¹]
EFFTRAN	238.6	1.11 ± 0.04
	338.3	1.12 ± 0.05
Angle	238.6	1.09 ± 0.05
	338.3	1.03 ± 0.06
GEANT 4	238.6	0.91 ± 0.05
	338.3	0.94 ± 0.05

different geometries. For Sample 1 the correct value of activity concentration is unknown so as a reference value we used average value with appropriate deviation. In Tables 5–7 as well as in Figs. 11–13, the total

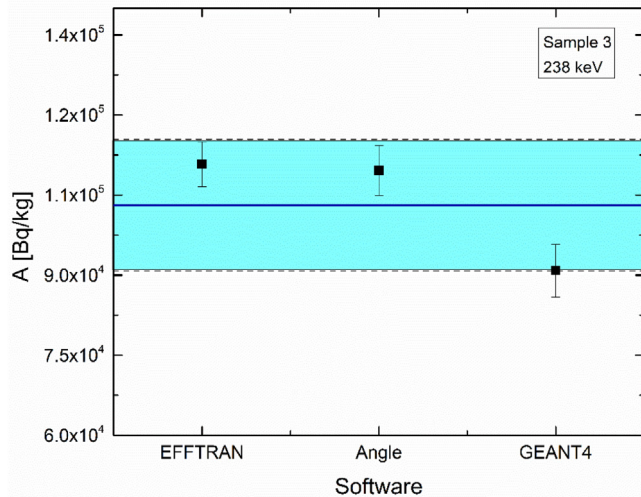


Fig. 9. Activity concentrations on 238.6 keV obtained by different methods for Sample 3.

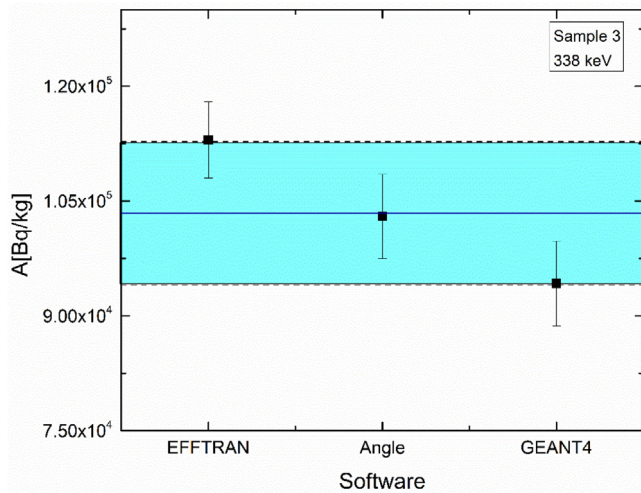


Fig. 10. Activity concentrations on 338.3 keV obtained by different methods for Sample 3.

Table 5
Total ²³⁸U activity concentration for Sample 1.

Software	Total ²³⁸ U activity concentration [MBq kg ⁻¹]	Medium value as a reference [MBq kg ⁻¹]	Relative deviation [%]
EFFTRAN	4.96 ± 0.08	4.82 ± 0.15	+2.92
Angle	4.67 ± 0.13		-3.26
GEANT 4	4.84 ± 0.15		+0.31

activity concentration of ²³⁸U and relative deviation from reference activity concentration is presented. Total activity was calculated both from 63.3 keV and 1001.03 keV lines (from ²³⁸U progeny) as well as from 143.8 keV and 163.3 keV gamma line (from ²³⁵U decay chain). When calculating the ²³⁸U activity concentration from ²³⁵U gamma lines, the following formula was used [21], where 1/0.046 is the ²³⁵U to ²³⁸U activity concentration ratio in natural samples.

$$A(^{238}\text{U}) = A(^{235}\text{U}) \cdot \frac{1}{0.046} \quad (6)$$

Relative deviations of total activity concentration for ²³⁸U from reference value for Sample 2 for two tested geometries are below 8% for both, semi-empirical and simulation, methods, Tables 6–7 and

Table 6
Total ²³⁸U activity concentration for Sample 2 in a horizontal vial.

Software	Total ²³⁸ U activity concentration [kBq kg ⁻¹]	Reference value [kBq kg ⁻¹]	Relative deviation [%]
EFFTRAN	4.96 ± 0.39	4.94 ± 0.49	+0.40
Angle	4.79 ± 0.38		-3.04
GEANT 4	5.25 ± 0.37		+3.58

Table 7
Total ²³⁸U activity concentration for Sample 2 in cylindrical geometry.

Software	Total ²³⁸ U activity concentration [kBq kg ⁻¹]	Reference value [kBq kg ⁻¹]	Relative deviation [%]
EFFTRAN	5.25 ± 0.44	4.94 ± 0.49	+6.38
Angle	5.31 ± 0.45		+7.61
GEANT 4	4.81 ± 0.39		-2.71

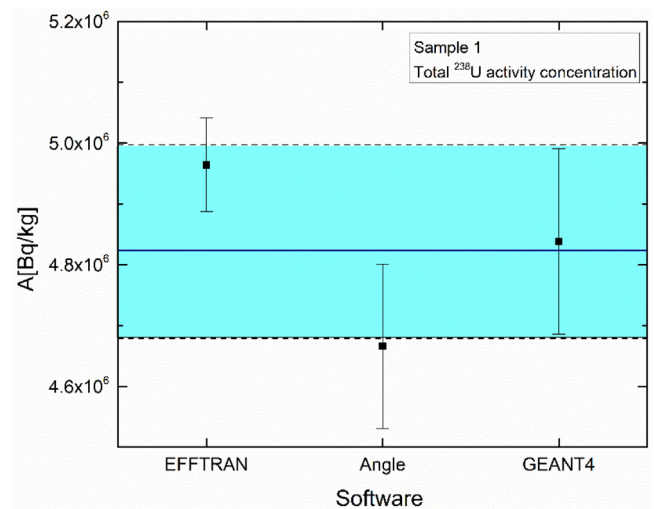


Fig. 11. Total ²³⁸U activity concentration for Sample 1.

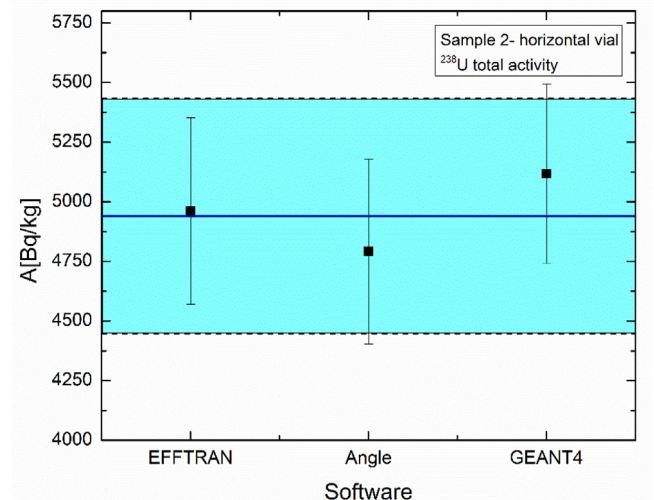


Fig. 12. Total ²³⁸U activity concentration for Sample 2 in a horizontal vial.

Figs. 12–13. Similar agreement between methods was obtained on specific energies, presented in Tables 2–3 and Figs. 7–8. In Ref. [20] similar conclusion was obtained by using a comparison of EFFTRAN

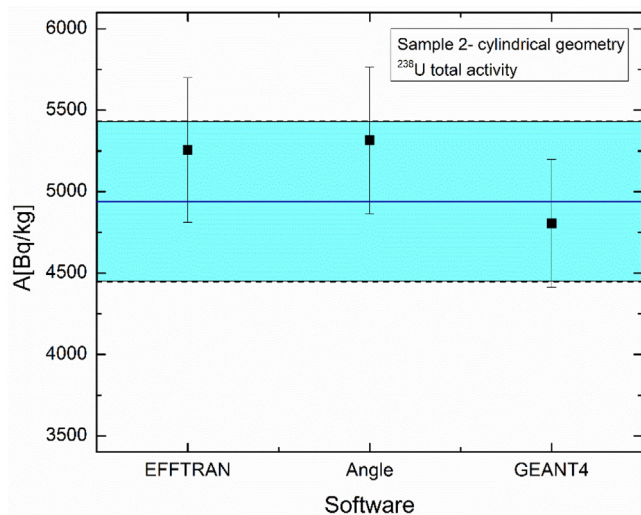


Fig. 13. Total ^{238}U activity concentration for Sample 2 in cylindrical geometry.

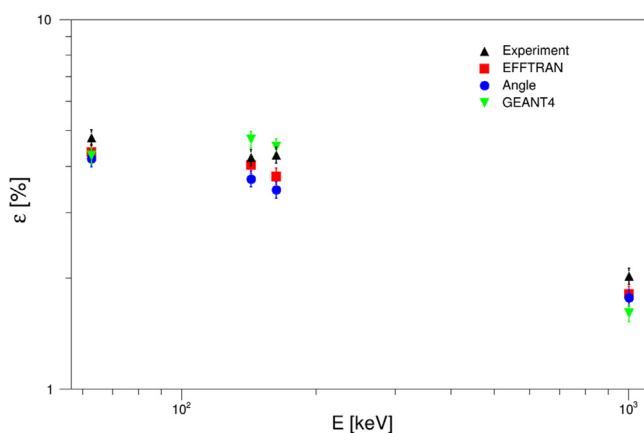


Fig. 14. A comparison between EFFTRAN, Angle, and GEANT 4 efficiency results and experimental results obtained for reference material Sample 2 for cylindrical geometry.

and GEANT 4, the authors concluded that when a lower part of the spectrum is of interest (63 keV line) EFFTRAN produces results with greater accuracy. In an ideal situation, the activity concentrations calculated separately for lines 63.3 keV and 1001.03 keV should be comparable. From Tables 1–3 it is obvious that Angle and EFFTRAN software both gave satisfactory results.

A similar assumption can be applied for calculation of activity concentration of ^{232}Th from energy lines 238.6 keV and 338.3 keV separately. The results presented in Table 4 are showing that all three used methods give expected results.

To get a more direct indication of the accuracy of the applied methodology, additional comparison between EFFTRAN, Angle, and GEANT 4 efficiency results and experimental results obtained for reference material Sample 2 for cylindrical geometry is presented in Fig. 14. Experimental efficiency was obtained with reference activity concentration values that are known in advance. Results presented in Fig. 14 clearly indicate the good agreement of efficiencies for all investigated methods.

4. Conclusion

The main idea of this paper was to test the applicability of two mathematical calculations software EFFTRAN and Angle for precise determination of the activity concentrations in comparison with the

simulation method (GEANT 4) for different sample geometries. The obtained results may be of use in every gamma-spectrometry laboratory that does not have commercial software designed especially for uranium content determination as analysis of nuclear and other radioactive materials for nuclear forensics needs are not that often. Both methods (two semi-empirical and simulation) were tested on 3 different sample geometries and matrices, although the samples measured are not directly related to the field of nuclear forensics they were used only for testing purposes and the conclusion could be related to any other sample. The analyzed samples were UO_2 pellet, the reference material in the cylindrical vertical axis, and cylindrical vial placed in a horizontal position on the detector, and a small metal plate with an irregular shape. The main idea of using a reference material was to test the methods with known activity concentrations. In practice, when speaking about samples that could be found out of regulatory control they can be in a variety of forms and composition and the overall conclusion of this investigation is that the only way to use EFFTRAN and Angle software for activity concentration determination (efficiency transfer method) is to approximate the geometry as close to cylindrical and also the composition–density of the sample should be approximated or measured. In GEANT 4 simulation toolkit the sample geometry and composition can be defined more precisely.

From the obtained results it can be concluded that both Angle and EFFTRAN efficiency transfer software with adequate approximate geometry definition gave satisfying results although Angle is not including coincidence summing correction and both software is designed for cylindrical vertical axis geometry. But the definition of sample geometry has to be performed as close as possible to the cylindrical shape. The main disadvantage is that in order to use that two software, certified reference material is needed. From the other side, GEANT 4 simulation method could be used without certified reference material with manufacturer definition of the detector, but more accurate results can be obtained if the definition of detector characteristics is done based both on manufacturer definition and with special adjustment with simulation performed on certified reference material. The other way is similar to the efficiency transfer method on which Angle and EFFTRAN are based.

The overall conclusion is that both methods (semi-empirical and simulation method) can be used for the initial estimation of the activity concentration of uranium radioisotopes in samples of different geometries. Although when using a simulation method a certified reference material is not needed, better results can be obtained if the detector set-up is validated with certified reference material. From the other side, although the geometry of the analyzed metal plate was challenging both methods gave comparable results for ^{232}Th activity concentration.

In future studies the tests can be made also for other non-cylindrical samples with the unknown radioisotope content as different nuclear and other radioactive materials can be found out of regulatory control and gamma spectrometry has been proved to be one of the best non-destructive technique for initial, fast characterization and categorization of the unknown material.

CRedit authorship contribution statement

Andrej Vraničar: Methodology, Formal analysis, Investigation, Writing - original draft. **Jovana Nikolov:** Conceptualization, Writing - review & editing, Supervision. **Nataša Todorović:** Validation, Methodology. **Ivana Maksimović:** Resources, Conceptualization. **Miloš Mladenović:** Resources, Conceptualization. **Dušan Mrđa:** Software, Formal analysis. **Miloš Travar:** Software, Formal analysis, Investigation.

Declaration of competing interest

The authors declare that they have no known competing financial interests or personal relationships that could have appeared to influence the work reported in this paper.

Acknowledgments

The authors acknowledge the financial support of the International Atomic Energy Agency (IAEA) via IAEA Research Contract No. 23159/R0 and of the Ministry of Education, Science and Technological Development of the Republic of Serbia (Grant No. 451-03-68/2020-14/200125).

References

- [1] K. Mayer, M. Wallenius, I. Ray, Nuclear forensics—a methodology providing clues on the origin of illicitly trafficked nuclear materials, *Analyst* 130 (2005) 433–441, <http://dx.doi.org/10.1039/b412922a>.
- [2] INFL Guideline: High-Resolution Gamma-Spectrometry General Overview, Nuclear Forensics ITWG, 2016.
- [3] Apostol, et al., Isotopic composition analysis and age dating of uranium samples by high resolution gamma ray spectrometry, *Nucl. Instrum. Methods Phys. Res. B* 383 (2016) 103–108.
- [4] Y.Y. Ebaid, Use of gamma-ray spectrometry for uranium isotopic analysis in environmental samples, *Rom. J. Phys.* (ISSN: 1221-146X) 55 (2009) 69–74.
- [5] R. Gunnick, et al., MGAU: A new analysis code for measuring U-235 enrichments in arbitrary samples, IAEA-SM-333/88, IAEA Symposium on International Safeguards, Vienna, 1994.
- [6] MGA++ software user's manual, software version 1, EG&G ORTEC.
- [7] FRAM-bwplutonium and uranium isotopic analysis software user's manual, ORTEC part no. 785030.
- [8] G. Stanic, J. Nikolov, I. Tucakovic, D. Mrdja, N. Todorovic, Z. Grahek, I. Coha, A. Vranicar, Angle. vs, Angle vs LabSOCS for HPGe efficiency calibration, *Nucl. Instrum. Methods Phys. Res. A* (ISSN: 0168-9002) 920 (2019) 81–87, <http://dx.doi.org/10.1016/j.nima.2018.12.059>.
- [9] S. Kaminski, A. Jakobi, C. Wilhelm, *Appl. Radiat. Isot.* 94 (2014) 306.
- [10] I. Tucakovic, D. Barisic, Z. Grahek, *Appl. Radiat. Isot.* (2017) 162.
- [11] D. Mrdja, et al., Optimization of the HPGe detector passive shields by Monte-Carlo simulations, *Nucl. Instrum. Methods A* 929 (2019) 76–83.
- [12] Preparation and Certification of IAEA Gamma Spectrometry Reference Materials RGU-1 IAEA, Rgth-1 and RGK-1, Report IAEA/RL/148, Vienna 1987.
- [13] A.N.G.L.E. 4, efficiency calculations for semiconductor and scintillation detectors, user guide, 2016.
- [14] S. Jovanovic, et al., Angle: A PC code for semiconductor detector efficiency calculations, *J. Radioanal. Nucl. Chem.* 218 (1) (1997) 13–20.
- [15] T. Vidmar, EFFTRAN—A Monte Carlo efficiency transfer code for gamma-ray spectrometry, *Nucl. Instrum. Methods Phys. Res. Sect. A: Accel. Spectrom. Detect. Assoc. Equip.* 550 (3) (2005) 603–608, <http://dx.doi.org/10.1016/j.nima.2005.05.055>.
- [16] T. Vidmar, et al., Testing efficiency transfer codes for equivalence, *Appl. Radiat. Isot.* (ISSN: 0969-8043) 68 (2010) 355–359.
- [17] S. Agostinelli, et al., Geant 4—a simulation toolkit, *Nucl. Instrum. Methods A* 506 (2003) 250–303.
- [18] D. Joković, A. Dragić, V. Udovičić, R. Banjanac, J. Puzović, I. Aničin, *Appl. Radiat. Isot.* 67 (5) (2009) 719.
- [19] M. Krmar, J. Hansman, N. Jovančević, N. Lalović, J. Slivka, D. Joković, D. Maletić, *Nuclear Instrum. Methods A* 709 (2013) 8–11.
- [20] J. Nikolic, T. Vidmar, D. Jokovic, M. Rajacic, D. Todorovic, *Nucl. Instrum. Methods Phys. Res. A* 763 (2014) 347–353.
- [21] G. Olszewski, A. Boryło, B. Skwarzec, The radiological impact of phosphogypsum stockpile in Wislinka (northern Poland) on the Martwa Wisła river water, *J. Radioanal. Nucl. Chem.* 307 (2016) 653–660.



Experimental information on mass- and TKE-dependence of the prompt fission γ -ray multiplicity



M. Travar^a, V. Piau^b, A. Gök^{c,1}, O. Litaize^b, J. Nikolov^a, A. Oberstedt^d, S. Oberstedt^{c,*}, J. Enders^e, M. Peck^e, W. Geerts^c, M. Vidali^c

^a University of Novi Sad, Faculty of Sciences, Department for Physics, 21000 Novi Sad, Serbia

^b CEA, DES, IRESNE, DER, SPRC, Cadarache, 13108 St. Paul lez Durance, France

^c European Commission, Joint Research Centre (JRC), 2440 Geel, Belgium

^d Extreme Light Infrastructure - Nuclear Physics (ELI-NP), 077125 Bucharest-Magurele, Romania

^e Technische Universität Darmstadt, Fachbereich Physik, Institut für Kernphysik, Schlossgartenstraße 9, 64289 Darmstadt, Germany

ARTICLE INFO

Article history:

Received 6 May 2020

Received in revised form 8 April 2021

Accepted 10 April 2021

Available online 14 April 2021

Editor: B. Blank

Keywords:

Prompt fission γ rays

γ multiplicity

Mass-dependent γ -ray emission

$M_\gamma(A)$

Total kinetic energy (TKE)

$\bar{\nu}(A)$

ABSTRACT

Prompt γ rays from the spontaneous fission of ^{252}Cf were measured with cerium-doped LaBr_3 detectors. The average prompt fission γ -ray multiplicity, M_γ , was determined as a function of fragment mass number (A) and total kinetic energy (TKE). High-statistics data, obtained from three detectors of different size at different angles relative to the fission chamber, confirms unequivocally a saw-tooth like shape of the γ multiplicity as a function of fragment mass, in contrast to previously published data. In addition, the TKE-dependence of M_γ was determined experimentally and compared with recent data.

© 2021 The Author(s). Published by Elsevier B.V. This is an open access article under the CC BY license (<http://creativecommons.org/licenses/by/4.0/>). Funded by SCOAP³.

1. Introduction

In recent years nuclear fission modeling has witnessed considerable progress. Research groups in the US [1–8], France and Germany [9–14] have developed model codes aiming at simulating prompt fission neutron and γ -ray emission. All models have in common that they rely on experimental fission-fragment data, e.g. emission yield and total kinetic energy, as well as on nuclear-structure data. Since, for very neutron-rich isotopes, the latter data is scarce, imprecise or even unavailable, model calculations rest on properties extrapolated from stable nuclei. The sharing of excitation energy between the two fission fragments at the moment of scission plays a crucial role here and can only be parametrized based on a limited number of prompt-fission neutron data. This situation leaves theoreticians with numerous model parameters. As a consequence, a coherent description of prompt neutron and γ -

ray emission is, to date, still lacking the necessary precision and predictability.

Hence, correlation data between prompt fission neutrons or γ rays and fission fragment properties, in particular yield and total kinetic energy (TKE), needs to be provided from experiment. For example, the mass-dependence of the prompt fission neutron (PFN) multiplicity, $\nu(A)$, is governed mainly by the initial excitation energy and may teach us about how it is partitioned between the two fragments at scission. The prompt γ -ray multiplicity for a given fragment mass, $M_\gamma(A)$, is determined by the nuclear structure of the fragments and the initial spin and excitation energy. Together, prompt neutron and γ -ray multiplicities, can guide the modeling of the fragments' excitation energy and angular momentum distribution.

Although several PFN measurement campaigns were conducted in recent years to obtain such correlated data, the few experimental data on prompt fission γ rays (PFG) essentially date back to the 1970s [15–21] and 1980s [22]. The former data from $^{233,235}\text{U}(n_{th},f)$, $^{239}\text{Pu}(n_{th},f)$ and $^{252}\text{Cf}(sf)$ showed that $M_\gamma(A)$ has a similar, saw-tooth like shape as observed for prompt neutrons, $\bar{\nu}(A)$. In contrast, Ref. [22] was interpreted to show only a weak dependence of the fragment mass, if any. The previously observed shape was interpreted as an artifact due to a wrongly calibrated

* Corresponding author.

E-mail address: stephan.oberstedt@ec.europa.eu (S. Oberstedt).

¹ Present address: Department of Physics, KTH Royal Institute of Technology, 10691 Stockholm, Sweden.

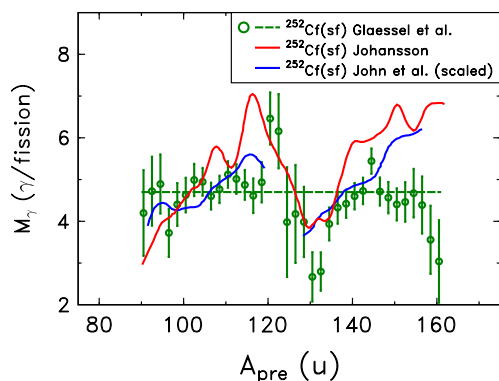


Fig. 1. Available experimental data on the prompt fission γ -ray multiplicity, M_γ , as a function of the fragment mass prior to prompt neutron emission, A_{pre} from the spontaneous fission of ^{252}Cf [15,17,22]; the data from John et al. [17] is multiplied with a constant to match our average total gamma multiplicity for shape comparison. The data was extracted from the corresponding publications by means of digitization [23].

mass scale of the fission detector. In Fig. 1 the so far available $M_\gamma(A)$ data for the spontaneous fission of ^{252}Cf is shown.

We have measured this mass-dependent PFG characteristics. In this paper we focus on the presentation of the employed experimental technique and the results on $M_\gamma(A)$ for the spontaneous fission of ^{252}Cf , but also its dependence on the fragments' total kinetic energy, $M_\gamma(TKE)$.

2. The experiment

The experiment was performed at the European Commission's JRC-GEEL. We coupled the VESPA (versatile γ spectrometer array) spectrometer to a position-sensitive Frisch-grid ionization chamber, developed in-house, which serves as fission detector [24]. We used three cerium-doped LaBr_3 γ -ray detectors of two different sizes. Those detectors offer a superior combination of intrinsic peak efficiency, energy and timing resolution [25–27], and their implementation led to considerable improvements of prompt fission γ ray spectra (PFGS) data [28], as demonstrated in a number of recent experiments on $^{252}\text{Cf}(\text{sf})$ [27,29,30], $^{235}\text{U}(n_{th}, f)$ [29,31] and $^{241}\text{Pu}(n_{th}, f)$ [29,32]. Here we used a ^{252}Cf source with a 5 mm wide circular spot deposited on a 250 nm thick nickel backing and a fission strength of 800 fissions per second. In total, the measurement went on for about three months.

2.1. The γ -ray detectors

One large-volume detector (A11218) was placed on the symmetry axis of the fission detector and two medium-size detectors at the same $\cos(\theta)$ with respect to the symmetry axis, but at different azimuthal angles, ϕ , labelled IKDA and A14400, as shown in Fig. 2. For all three detectors, the distance to the fission source was about 35 cm. The γ -ray detectors were calibrated in the energy range between 80 keV and 9 MeV with several standard sources, ^{133}Ba , ^{137}Cs and ^{60}Co , ^{208}Tl , as well as with $^9\text{Be}(\alpha, n)^{12}\text{C}$ and $^{58}\text{Ni}(n_{th}, \gamma)$ reactions. The three calibration spectra up to $E_\gamma = 4.4$ MeV are depicted in Fig. 3. The energy resolution at $E_\gamma = 662$ keV was 3.5, 2.8 and 3.0% for detector A11218, IKDA and A14400, respectively.

2.2. The fission-fragment detector

The fission-fragment detector provides information about the fragment energies and masses, as well as the fission-axis orientation, which is needed to reconstruct the direction of γ -ray emission. For details about the design and working principle we refer to Ref. [24].

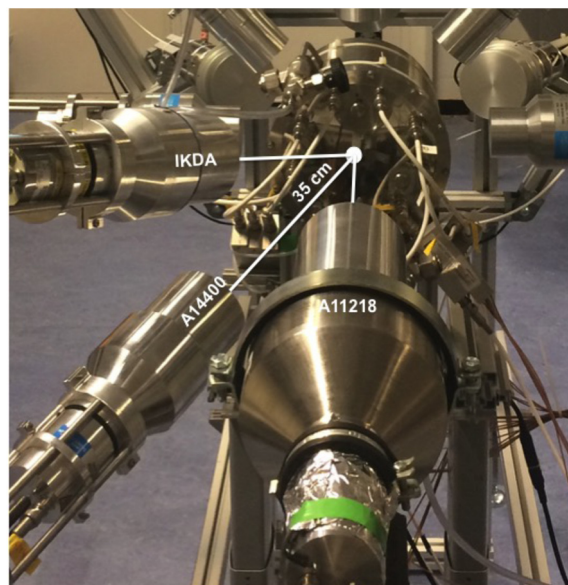


Fig. 2. Partial view of the versatile γ spectrometer array, VESPA, and the position-sensitive fission detector; the three cerium-doped LaBr_3 γ -ray detectors, of size (diameter \times length) 89 mm \times 203 mm (A11218) and 76 mm \times 76 mm (IKDA, A14400), used for the present work are labeled.

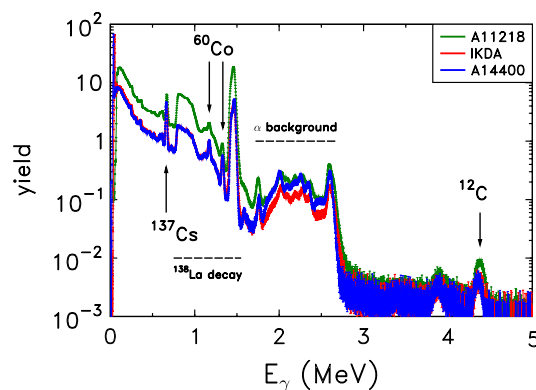


Fig. 3. Calibration spectra for the three cerium-doped LaBr_3 γ -ray detectors, as shown and specified in Fig. 2, for γ -ray energies up to 4440 keV.

Fission fragment energies and masses are determined via the double-kinetic-energy ($2E$) technique, based on conservation of mass and linear momentum [33–35]. The intrinsic energy resolution of the ionization chamber is better than 0.6 MeV. Taking target thickness, responsible for an average energy spread of about 0.4 MeV, and correction for the PFN emission into account, we end up with a TKE resolution of about 1.5 MeV [36]. As counting gas we used CH_4 gas (99.9995%). The pulse height defect of the counting gas is corrected with parameters adjusted to reproduce known values of the average light and heavy fragment masses and TKE [37,38]. The deviation of the average light and heavy pre-neutron fission-fragment masses is smaller than $0.25 u$. The correctness of the mass calibration was verified by gating on several isomeric γ -decay lines (Fig. 4 a) and projecting the data on the fragment-mass axis. The corresponding mass spectra in ^{95}Sr and ^{134}Te are depicted in Fig. 4 b), as representative examples. The pre- and post-neutron mass resolution at $A = 95$ is 4.2 u and 4.9 u (FWHM), respectively. The coincidence timing resolution of the fission chamber with a γ -ray detector was around 1 ns (FWHM). Since prompt γ -rays were taken in an interval of ± 3 ns relative to fission, all prompt fission neutrons were essentially discriminated.

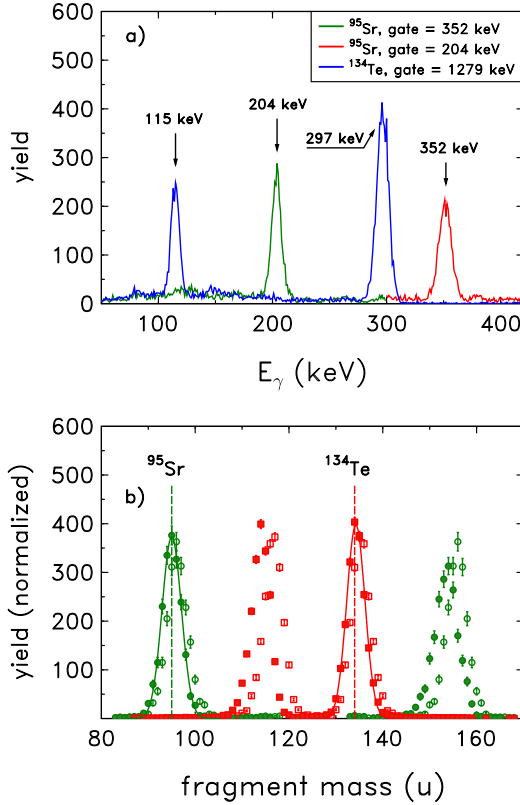


Fig. 4. a) Isomeric γ -rays from ^{95}Sr and ^{134}Te used for calibrating the fragment-mass scale; b) Fragment-mass spectra gated on the isomeric transitions shown in a); open symbols depict pre-neutron masses and full symbols post-neutron masses. The pre- and post-neutron mass resolution is 4.2 and 4.9 u (FWHM), respectively.

3. Data analysis

From each detector, we constructed a set of background-corrected PFG spectra for several mass and TKE bins, $S_{ij}(A_i, TKE_j)$. Those spectra have to be deconvoluted in order to get the correct multiplicities. Deconvolution matrices were calculated from the detector responses, simulated with the GEANT-4 simulation toolkit [41], and from the integral spectra, i.e. $I = \sum S_{ij}$. These calculations were performed through the iterative unfolding method described in Ref. [43], implemented within the RooUnfold framework [42]. From the *deconvoluted* PFG spectra we obtain the number of γ -rays that enter into the solid angle covered by the γ -ray detector for $80 \text{ keV} \leq E_\gamma \leq 8 \text{ MeV}$, denoted as $n_{\gamma,A,TKE}$. In the following the subscript TKE is dropped as it has no bearing on the analysis principle.

We have not performed full efficiency calibrations of the γ -ray detectors used in the experiment. Instead, we have corrected the GEANT-4 simulated efficiency by scaling the total γ -ray multiplicity to results from Ref. [30], taking into account the difference in energy range.

Then, we obtained multiplicity and average total γ energy as functions of single fragment mass utilizing the Doppler shift and relativistic aberration in the laboratory angular distribution of PFG emission. We started from the fission-fragment analysis that provides us with the fragment mass and kinetic energy, from which we calculated on an event-by-event basis the velocity component of the de-exciting fragment in the direction of the γ -ray detector, expressed relative to the speed of light c , β_A or β_{Acn-A} . The indices A and $Acn-A$ denote the mass of the fragment and the complementary fragment, respectively. Since the kinematic anisotropy of the emitted number of γ -rays, $\alpha_N = 2\beta \cos\theta + f(\beta^2)$, has its maximum at $\theta = 0^\circ$ relative to the fission axis, only

the cones of fission-fragment emission towards the γ detectors are taken into account. This cone had a size of $\Delta\theta \approx 25^\circ$, very similar to the one in Ref. [22]. Full details of the concept may be found in Ref. [19], but for the sake of clarity the essential ingredients are recalled in the following. For the sake of traceability we follow very closely the notation employed therein.

The number of γ -rays that enter into the solid angle covered by the γ -ray detector, $n_{\gamma A}$, when a fragment with mass A flies in the direction of the detector and the complementary fragment, with mass $Acn-A$, moves in the opposite direction is

$$n_{\gamma A} = n_A \{M_{\gamma A}(1 + 2\beta_A) + M_{\gamma Acn-A}(1 - 2\beta_{Acn-A})\} \quad (1)$$

where $M_{\gamma A}$ and $M_{\gamma Acn-A}$ denote the mass-dependent γ -ray multiplicities. The number of fission fragments detected in the direction of the γ detector and in the opposite direction are denoted n_A and n_{Acn-A} , respectively. Since A and $Acn-A$ refer to the fragment masses before prompt neutron evaporation, n_A and n_{Acn-A} are equal by definition. However, because of instrumental asymmetry in the detection of fission fragments on either side of the target, the experimentally observed distributions will never be exactly equal.

For the complementary fragment, Eq. (1) turns into

$$n_{\gamma Acn-A} = n_{Acn-A} \{M_{\gamma A}(1 - 2\beta_A) + M_{\gamma Acn-A}(1 + 2\beta_{Acn-A})\} \quad (2)$$

Re-arranging Eqs. (1) and (2) and subsequent simultaneous solution results in

$$M_{\gamma A} = \frac{1 + 2\beta_{Acn-A}}{4(\beta_A + \beta_{Acn-A})} \frac{n_{\gamma A}}{n_A} - \frac{1 - 2\beta_{Acn-A}}{4(\beta_A + \beta_{Acn-A})} \frac{n_{\gamma Acn-A}}{n_{Acn-A}} \quad (3)$$

This is essentially the same result as presented in Ref. [22], except for the fact that here the forward-backward asymmetry of the fission detector is explicitly taken into account. This proved to be an essential difference, which if not taken into account² resulted in different $M_{\gamma A}$ curves for each γ -ray detector. As seen in Eq. (3), the determination of $M_{\gamma A}$ comes down to the ratio of two mass distributions, with and without coincidences. The differences in the mass distributions $n_{\gamma A}$ and $n_{\gamma Acn-A}$ caused by the relativistic aberration, as described by Eqs. (1) and (2), are very small and will be masked by instrumental asymmetry between the detection of fission fragments on the two sides of the fission target. This instrumental asymmetry can, however, be cancelled if the coincident mass distribution is always divided by the non-coincident mass distribution detected on the same side of the target. As a last step one needs to remember that the dependence of the multiplicity on β_A, β_{Acn-A} in Eq. (3) comes down to a dependence on TKE. Therefore, to get the mass-dependent multiplicity, $M_\gamma(A)$, we needed to sum the matrix $M_\gamma(A, TKE)$ over TKE:

$$M_\gamma(A) = \sum_{TKE} M_\gamma(A, TKE) \times [n_A(TKE) + n_{Acn-A}(TKE)] / \sum_{TKE} [n_A(TKE) + n_{Acn-A}(TKE)]. \quad (4)$$

The uncertainties for $n_{\gamma A}$ and $n_{\gamma Acn-A}$ are estimated using the bootstrapping method [44]. This method uses “toys”, which are histograms filled after sampling the original content h_k of each bin assuming a normal distributed error e_k , $\mathcal{N}(\mu = h_k, \sigma = e_k)$.

² By assuming $n_{Acn-A} = n_A$.

We generated 100 toys from the statistical uncertainties of the response functions and of each spectrum S_{ij} . No systematic uncertainties, e.g. uncertainties in the cross-sections, were taken into account. The uncertainty on n_γ is the standard deviation of the set of \bar{n}_γ obtained from the 100 toys. The total uncertainty of $M_\gamma(A, TKE)$ is then calculated by error propagation.

Since fission fragments are gradually stopped in the counting gas, their velocity at the time they emit the γ -rays is not necessarily the velocity they were born with. In order to account for this, we performed energy-loss calculations with the SRIM code [39] to assess the velocity of each fragment after traveling through the gas for 0.1 ns, the average emission time according to Refs. [15,16]. This emission time determines the effective kinetic energy of the fragments and, therefore, the cone of emission. The effect of this reduction in velocity on $M_\gamma(A)$ was added as a systematic uncertainty. The energy loss in the nickel backing was also taken into account.

4. Results

After the treatment of the data we have determined the multiplicity as a function of both fragment mass (A) and corresponding total kinetic energy (TKE). In the following subsections we present the obtained distributions together with other experimental data from literature, when available.

4.1. The mass-dependent emission of prompt fission γ rays

In Fig. 5 a) we show the measured mass dependence of the prompt fission γ -ray multiplicity for all three detectors. The uncertainties correspond to the linear sum of statistical and systematic uncertainty. The systematic uncertainty accounts for about 0.04 γ /fragment mass on average, weakly dependent on the fragment mass, while the average statistical uncertainty from the bootstrapping method is 0.22 γ /fragment mass (see Fig. 5 b) for the corresponding mass dependence).

Obviously, the distributions show a very distinct, saw-tooth like shape, which is independent of the position of the individual detector with respect to the fission chamber. All distributions overlap within the uncertainties in the mass range between 83 and 168. This makes us confident in the quality of our data and that the observed shape is real. In addition, an averaged distribution is depicted as well.

4.2. The TKE-dependent emission of prompt fission γ rays

In Fig. 6 the same physical quantity is exhibited as in Fig. 5 a), but now as a function of TKE in the range from 140 to 220 MeV. Again, all distributions lie very much on top of each other and agree well within the uncertainties. Results from a recent measurement [40] are also shown for comparison.

5. Discussion

Before we started this study, the initially observed structure in the mass-dependent average PFG multiplicity distribution [15,17], $M_\gamma(A)$, had been questioned and attributed to an experimental artifact, e.g. due to an erroneous calibration of the mass scale [22]. Therefore, we explicitly paid attention to this issue as presented in Sect. 2.2. We performed also a data analysis with only provisional masses, i.e. without applying prompt neutron corrections. The effect turned out to be completely negligible and did practically not change the shape of the distribution at all. The time window was a little narrower than that in Ref. [22] assuring complete PFN suppression. FIFRELIN calculations have shown that varying the time

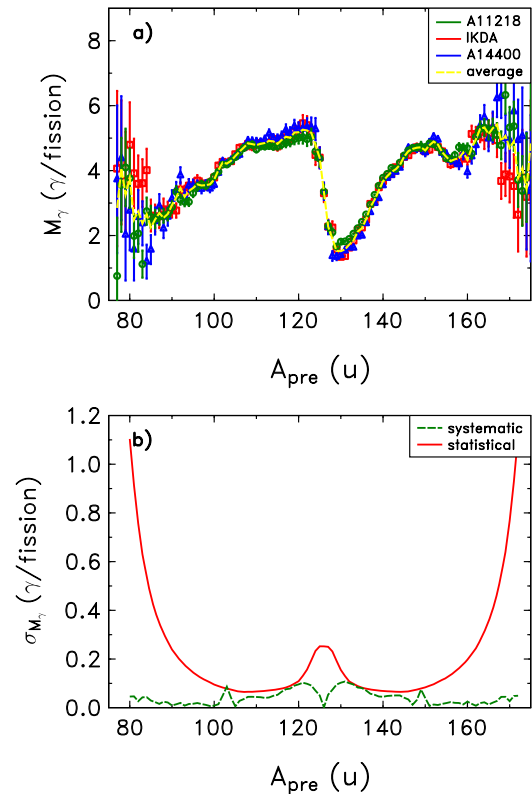


Fig. 5. a) Pre-neutron mass-dependent PFG multiplicity, $M_\gamma(A)$, obtained with each of the three detectors; the mean is depicted with the yellow dashed line; b) Corresponding statistical and systematic uncertainties.

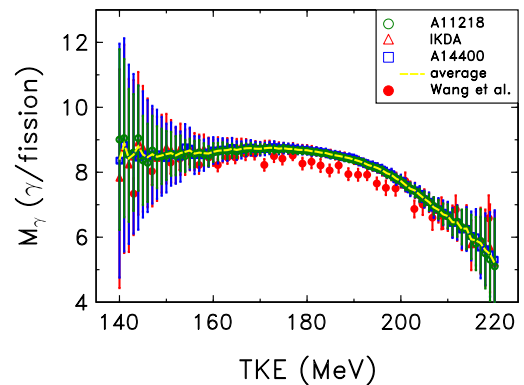


Fig. 6. TKE-dependent PFG multiplicity, $M_\gamma(TKE)$, as obtained with each of the three detectors. The statistical uncertainty accounts for 0.55 γ /MeV on average, while the systematic uncertainty is negligible, i.e. 0.005 γ /MeV. Experimental data from Ref. [40] is shown for comparison.

window within a few nanoseconds does not change notably the mass dependence of M_γ [45].

In Fig. 7 a) we present our result, depicted as a shaded area between the upper and lower boundaries (one sigma) of the distribution, averaged over the three distributions shown in Fig. 5 a). We compare it with the data from the same fissioning system, presented already in Fig. 1. Our data does not leave any doubt about the shape of the multiplicity distribution. The sawtooth shape indicates a positive correlation between the average γ -ray and neutron multiplicities as a consequence from the correlation between fragment deformation at scission and angular momentum, reflected by $\bar{\nu}(A)$ and $M_\gamma(A)$, respectively [46].

In Fig. 7 b) we compare our experimental data with latest FIFRELIN calculations using the latest version of the database RIPL-

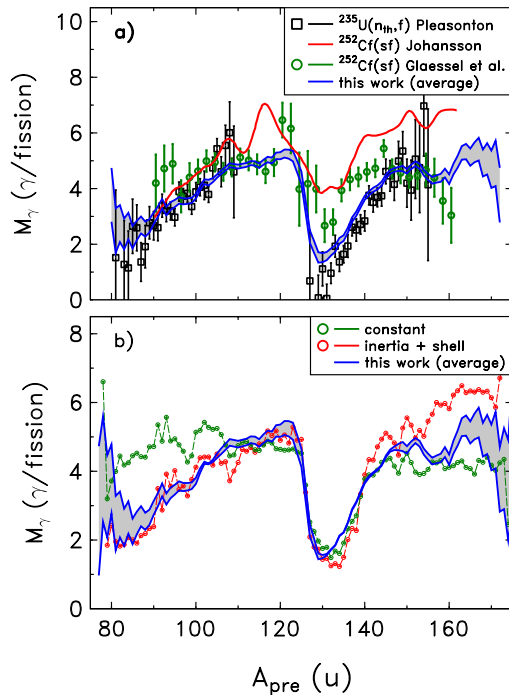


Fig. 7. a) Comparison of our measured pre-neutron mass-dependent PFG multiplicity distribution, $M_\gamma(A)$, from the spontaneous fission of ^{252}Cf , together with previous results from Refs. [15,22] for the same system. Corresponding data from Ref. [19] for $^{235}\text{U}(n_{th}, f)$ were added to support the observed trend; b) Comparison with recent FIFRELIN calculations, with parameters adjusted to reproduce experimental data on $\bar{\nu}_L/\bar{\nu}_H$, considering initial spin distributions driven by two different spin cut-off models. The FIFRELIN data has been normalized to the same average gamma-ray multiplicity as the one obtained in this work, $\bar{M}_\gamma = 8.39 \gamma / \text{fission}$.

3-2020 [47]. In FIFRELIN, the excitation energy sharing among fission fragments is based on an empirical *Temperature Ratio Law*, as explained more detailed in Ref. [48]. The distribution of the angular momentum, J , for a given fragment writes

$$P(J) = \frac{2J+1}{2\sigma^2} \exp \left\{ -\frac{(J+1/2)^2}{2\sigma^2} \right\}, \quad (5)$$

where the parameter σ is the so-called *spin cut-off parameter*. Two different models are presented in Fig. 7 b). The *constant model* uses two different constant parameters, for heavy (H) and light fragments (L), which are then free parameters of the simulation. In the *inertia+shell* model, the spin cut-off parameter depends on the moment of inertia, \mathcal{I} , and the nuclear temperature, T , of the fragment:

$$\sigma^2 = k_{H,L} \times \frac{a}{\bar{a}} \times \mathcal{I} T, \quad (6)$$

where k_H and k_L are free parameters of the simulation. The moment of inertia, \mathcal{I} , is calculated from the rigid-body model including the quadrupole deformation parameter of the nucleus in its ground state and, T is derived assuming that the nucleus is a Fermi-gas (for more details see Ref. [48]). The level density parameter a is following the Ignatyuk prescription as referred in RIPL-3 [49] and, \bar{a} is its asymptotic value. This additional ratio a/\bar{a} is included to take into account the shell effects in nuclei [14,49]. At low excitation energies, a discrete spin cut-off based on known low-lying states of the nuclear level scheme is used as recommended in Ref. [49].

The *inertia+shell* model predicts a sawtooth-like behavior of $M_\gamma(A)$ with minima at $A \approx 80$ and $A = 132$. A constant value of $\sigma(A)$ for the light fragments completely fails to reproduce the structure of $M_\gamma(A)$, while the *inertia+shell* model reproduces the

data remarkably well. However, this model fails in the heavy fragment region, indicating that the average spin is over-predicted in this region. This shows that improvements in the FIFRELIN models and/or their parameters are needed. Presently, shell corrections, moments of inertia and spin distributions from microscopic calculations are being studied. These studies are beyond the scope of the present experimental work.

6. Conclusion

With our recent measurement of the average prompt fission γ -ray multiplicity as a function of pre-neutron fragment mass, $M_\gamma(A_{pre})$, we have unambiguously confirmed the sawtooth-like shape with distinct local minima at $A_{pre} \approx 80$ and $A_{pre} = 130$. The high-statistics data allowed testing model calculations with high sensitivity as demonstrated with the modeling of the spin cut-off parameter used in FIFRELIN.

This was possible by measuring the correlations between M_γ and A_{pre} (and TKE , see below) with three different γ -detectors of different size and position relative to the symmetry axis of the fission detector and assuring proper energy and mass calibration of our setup. In addition, a compact experimental geometry and about three months of data taking provided good statistics for measurements with high precision.

The observed average prompt fission γ -ray multiplicity as a function of TKE , $M_\gamma(TKE)$, exhibits a rather constant behavior from 140 MeV up to about 180 MeV, turning into an almost linear decrease towards 220 MeV. To our knowledge there is only one other experimental set of data available, which agrees well to our result (see Fig. 6).

Declaration of competing interest

The authors declare that they have no known competing financial interests or personal relationships that could have appeared to influence the work reported in this paper.

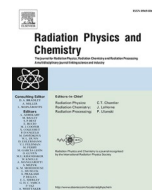
Acknowledgements

This work has been partially supported by the ENEN+ project that has received funding from the EURATOM research and training Work Programme 2016 - 2017 - 1 #755576. MP and JE acknowledge support from BMBF (05P18RDEN9) and HMWK (LOEWE research cluster Nuclear Photonics). AO acknowledges the support from the Extreme Light Infrastructure Nuclear Physics (ELI-NP) Phase II, a project co-financed by the Romanian Government and the European Union through the European Regional Development Fund - the Competitiveness Operational Programme (1/07.07.2016, COP, ID 1334), with which this work had been finalized. We thank D. Szymochko and the groups of T. Aumann and N. Pietralla for the loan of the $\text{LaBr}_3:\text{Ce}$ detector.

References

- [1] B. Becker, P. Talou, T. Kawano, Y. Danon, I. Stetcu, *Phys. Rev. C* **87** (2013) 014617.
- [2] P. Talou, I. Stetcu, T. Kawano, *Phys. Proc.* **59** (2014) 83.
- [3] P. Talou, T. Kawano, I. Stetcu, R. Vogt, J. Randrup, *Nucl. Data Sheets* **118** (2014) 227.
- [4] I. Stetcu, P. Talou, T. Kawano, M. Jandel, *Phys. Rev. C* **90** (2014) 024617.
- [5] R. Vogt, J. Randrup, *Phys. Proc.* **47** (2013) 3.
- [6] R. Vogt, J. Randrup, *Nucl. Data Sheets* **118** (2014) 220.
- [7] J.M. Verbeke, J. Randrup, R. Vogt, *Comput. Phys. Commun.* **191** (2015) 178.
- [8] J. Randrup, P. Talou, R. Vogt, *Phys. Rev. C* **99** (2019) 054619.
- [9] D. Regnier, O. Litaize, O. Serot, *Phys. Proc.* **31** (2012) 59.
- [10] D. Regnier, O. Litaize, O. Serot, *Phys. Proc.* **47** (2013) 47.
- [11] O. Litaize, D. Regnier, O. Serot, *Phys. Proc.* **59** (2014) 98.
- [12] O. Serot, O. Litaize, D. Regnier, *Phys. Proc.* **59** (2014) 132.
- [13] K.-H. Schmidt, B. Jurado, C. Amouroux, Ch. Schmitt, *Nucl. Data Sheets* **131** (2016) 107.

- [14] L. Thulliez, O. Litaize, O. Serot, EPJ Web Conf. 111 (2016) 10003.
- [15] S.A.E. Johansson, Nucl. Phys. 60 (1964) 378.
- [16] K. Skarsvag, Nucl. Phys. A 253 (1975) 274.
- [17] W. John, J.J. Wesolowski, F. Guy, Phys. Lett. B 30 (1969) 340.
- [18] H. Albinsson, Yield of Prompt Gamma Radiation in Slow Neutron Induced Fission of ^{236}U as a Function of the Total Fragment Kinetic Energy, Internal Rep. AE-417, 1971.
- [19] F. Pleasonton, R.L. Ferguson, H.W. Schmitt, Phys. Rev. C 6 (1972) 1023.
- [20] H. Nifenecker, C. Signarbieux, M. Ribrag, J. Poitou, J. Matuszek, Nucl. Phys. A 189 (1972) 285.
- [21] F. Pleasonton, Nucl. Phys. A 213 (1973) 413.
- [22] P. Glässel, R. Schmid-Fabian, D. Schwalm, D. Habs, H.U. von Helmolt, Nucl. Phys. A 502 (1989) 315c.
- [23] Plot Digitizer, J.A. Huwaldt, S. Steinhorst, version 2.6.8 - October 27, <http://plotdigitizer.sourceforge.net/>, 2015.
- [24] A. Göök, W. Geerts, F.-J. Hamsch, S. Oberstedt, M. Vidali, Sh. Zeynalov, Nucl. Instrum. Methods A 830 (2016) 366.
- [25] R. Billnert, S. Oberstedt, E. Andreotti, M. Hult, G. Marissens, A. Oberstedt, Nucl. Instrum. Methods A 647 (2011) 94.
- [26] A. Oberstedt, S. Oberstedt, R. Billnert, W. Geerts, F.-J. Hamsch, J. Karlsson, Nucl. Instrum. Methods A 668 (2012) 14.
- [27] R. Billnert, F.-J. Hamsch, A. Oberstedt, S. Oberstedt, Phys. Rev. C 87 (2013) 024601.
- [28] S. Oberstedt, R. Billnert, F.-J. Hamsch, M. Lebois, A. Oberstedt, J.N. Wilson, Eur. Phys. J. A 51 (2015) 178.
- [29] R. Billnert, T. Belgia, T. Bryś, W. Geerts, C. Guerrero, F.-J. Hamsch, Z. Kis, A. Oberstedt, S. Oberstedt, L. Szentmiklosi, K. Takács, M. Vidali, Phys. Proc. 59 (2014) 17.
- [30] A. Oberstedt, R. Billnert, F.-J. Hamsch, S. Oberstedt, Phys. Rev. C 92 (2015) 014618.
- [31] A. Oberstedt, T. Belgia, R. Billnert, R. Borcea, T. Bryś, W. Geerts, A. Göök, F.-J. Hamsch, Z. Kis, T. Martinez, S. Oberstedt, L. Szentmiklosi, K. Takács, M. Vidali, Phys. Rev. C 87 (2013) 051602(R).
- [32] S. Oberstedt, R. Billnert, T. Belgia, T. Bryś, W. Geerts, C. Guerrero, F.-J. Hamsch, Z. Kis, A. Moens, A. Oberstedt, G. Sibbens, L. Szentmiklosi, D. Vanleeuw, M. Vidali, Phys. Rev. C 90 (2014) 024618.
- [33] C. Budtz-Jørgensen, H.-H. Knitter, Nucl. Phys. A 490 (1988) 307.
- [34] A. Al-Adili, F.-J. Hamsch, S. Pomp, S. Oberstedt, M. Vidali, Phys. Rev. C 93 (2016) 034603.
- [35] A. Göök, C. Eckardt, J. Enders, M. Freudenberger, A. Oberstedt, S. Oberstedt, Phys. Rev. C 96 (2017) 044301.
- [36] A. Göök, F.-J. Hamsch, S. Oberstedt, M. Vidali, Phys. Rev. C 98 (2018) 044615.
- [37] F.-J. Hamsch, J. Van Aarle, R. Vogt, Nucl. Instrum. Methods A 361 (1995) 257.
- [38] F. Gönnewein, in: C. Wagemans (Ed.), The Nuclear Fission Process, CRC, Boca Raton, FL, 1991, pp. 287–473, Chap. 8.
- [39] www.srim.org/SRIM/SRIMLEGL.htm (Stopping and Range of Ions in Matter).
- [40] T. Wang, G. Li, L. Zhu, Q. Meng, L. Wang, H. Han, W. Zhang, H. Xia, L. Hou, R. Vogt, J. Randrup, Phys. Rev. C 93 (2016) 014606.
- [41] S. Agostinelli, et al., Nucl. Instrum. Methods A 506 (2003) 250.
- [42] T. Adye, Unfolding algorithms and tests using RooUnfold, in: Proceedings of the PHYSTAT 2011 Workshop on Statistical Issues Related to Discovery Claims in Search Experiments and Unfolding, 2011. See also <https://gitlab.cern.ch/RooUnfold/RooUnfold>.
- [43] G. D'Agostini, Nucl. Instrum. Methods A 362 (1995) 487.
- [44] B. Efron, R. Tibshirani, An Introduction to the Bootstrap, Chapman & Hall/CRC, Boca Raton, FL, ISBN 0-412-04231-2, 1993.
- [45] O. Litaize, A. Chebboubi, O. Serot, L. Thulliez, T. Materna, M. Rapala, EPJ Nucl. Sci. Technol. 4 (2018) 28.
- [46] G.F. Bertsch, T. Kawano, L.M. Robledo, Phys. Rev. C 99 (2019) 034603.
- [47] <https://www-nds.iaea.org/RIPL-3/>.
- [48] O. Litaize, O. Serot, L. Berge, Eur. Phys. J. A 51 (2015) 177.
- [49] R. Capote, M. Herman, P. Obložinský, P.G. Young, S. Goriely, T. Belgia, A.V. Ignatyuk, A.J. Koning, S. Hilaire, V.A. Plujko, M. Avrigeanu, O. Bersillon, M.B. Chadwick, T. Fukahori, Zhigang Ge, Yinlu Han, S. Kailas, J. Kopecky, V.M. Maslov, G. Reffo, M. Sin, E.Sh. Soukhovitskii, P. Talou, Nucl. Data Sheets 110 (2009) 3107.



Sample matrix influence on the efficiency function modeling for uranium isotopes determination by gamma spectrometry

A. Vraničar^a, J. Nikolov^{a,*}, Đ. Lazarević^b, A. Rikalo^c, N. Todorović^a, D. Arbutina^b, M. Travar^a

^a University of Novi Sad, Faculty of Sciences, Trg Dositeja Obradovića 3, 21000, Novi Sad, Serbia

^b Public Company Nuclear Facilities of Serbia, PO Box 4, 11000, Belgrade, Serbia

^c University of Novi Sad, Faculty of Technical Sciences, Trg Dositeja Obradovića 6, 21000, Novi Sad, Serbia

ARTICLE INFO

Keywords:

Gamma spectrometry
Monte-Carlo simulation
Semi-empirical efficiency transfer method
Iterative procedure
Sample matrix determination

ABSTRACT

The aim of the presented study was to explore the influence of precise determination of sample matrix in order to obtain reliable gamma spectrometry results. The test was done using two different approaches which have the same goal: quantifying the activity concentration of uranium isotopes in different samples found in the former uranium ore deposit Mazdreja. The first approach is based on iterative methodology, which utilizes the characteristic of a sample that can be quantified before gamma spectrometric measurement. Density of the sample and calculated mass fractions of its constituents (which vary in each iteration) can help to obtain the efficiency function from which activity concentrations of ²³⁵U and ²³⁸U can be derived and corresponding masses of uranium for the next iteration. In this approach LabSOCS software is used in order to obtain appropriate efficiency. The second approach that was tested represents semiempirical method which applies Monte-Carlo simulations through Geant4 and EFFTRAN software codes for the purposes of generating the detection efficiency functions needed for further calculations.

The idea was to compare different methods for uranium activity concentration determination in sample matrices with high uranium mass content and also establish the need for precise calculation (described within the iterative method) by quantifying the relative deviation in activities, calculated by using different methods.

From the obtained results, it can be seen that it is very important to adjust the sample matrix to correct composition if we need a precise gamma spectrometry result. But if there is a need to get results in a short period of time, then for the estimation of the activity concentration of the analyzed sample an approximate sample composition can be used. All three tested analyzed methods gave comparable results inside 15% of difference. The major difference was obtained by EFFTRAN software, but on the other side this software is user-friendly and the results can be obtained faster than by using other analysis methods presented in this study.

1. Introduction

Sample matrices containing elements from the actinide series, especially uranium, are found to be a very important topic for research due to the facts that they present hazards associated with TENORM [Dowdall et al., 2004], the use of depleted uranium, and illegal trafficking of nuclear and other radioactive materials.

In the past, when technology for HPGe detectors with high detection efficiency in the higher energy spectrum wasn't available, the measurement of ²³⁸U activity was mostly based on the analysis of the 63.3 keV peak of ²³⁴Th (with an intensity of 3.7%). This was due to the poor counting statistics of the less intense 1001.03 keV peak of ^{234m}Pa

(0.84%) which has less spectral interferences. Nowadays, when adequate HPGe technology is present, the 1001.03 keV peak is widely used for ²³⁸U activity determination [Dowdall et al., 2004] [Yücel et al., 1998]. As it can be seen, in gamma spectrometry the uranium activity is determined indirectly through gamma lines of the daughter nuclides. When analyzing gamma spectra from high uranium content samples, one must take into consideration the high spectral interferences and high self-attenuation in the measured sample on 63.3 keV peak of ²³⁴Th which lies on the high-background continuum. It is shown that ignoring the spectral contributions of ²³⁵U and ²³²Th on the 63.3 keV gamma peak can lead to great deviation (0.8–122%) in calculated ²³⁸U activity, while in the instance of disregarding the contribution of ²³²Th (via

* Corresponding author.

E-mail address: jovana.nikolov@df.uns.ac.rs (J. Nikolov).

<https://doi.org/10.1016/j.radphyschem.2021.109891>

Received 6 September 2021; Received in revised form 3 November 2021; Accepted 16 November 2021

Available online 23 November 2021

0969-806X/© 2021 Elsevier Ltd. All rights reserved.

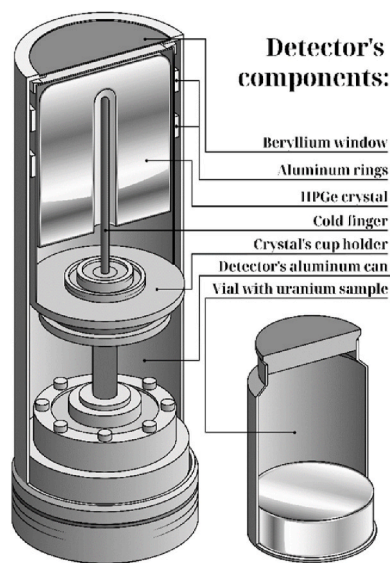


Fig. 1. Detector 1 and a representation of sample.

^{228}Ac) to the peak at 1001 keV of $^{234\text{m}}\text{Pa}$, results in a relatively smaller systematic influence of 0.05–3%, depending on thorium contents in the samples [Yücel et al., 2009]. Therefore, if the technical terms are met, one should take the high-energy uranium peak (1001 keV) for activity calculation, due to the lesser sample matrix influence on the accuracy of the final result.

The aim of this study was to compare different approaches for uranium activity concentration determination in sample matrices with high uranium mass content and also establish the need for precise calculation (described within the iterative method) by quantifying the relative deviation in activities, calculated by using different methods. In this paper, two different approaches for calculating the activity concentration of uranium isotopes are presented. One is an iterative method which uses comprehensive analysis involving the calculation of uranium mass in each iterative step and multiple correction factors for the activity calculation, and the other is a semi-empirical approach, described in [Vranićar et al., 2021], which uses two different software (EFFTRAN and Geant4).

2. Materials and methods

2.1. Detectors

Samples that are analyzed in this work were measured on two detectors. Detector 1 is a High Purity Germanium (HPGe) low background extended range coaxial detector. It is made by ORTEC with a serial mark GMX-20190. It is an N-type coaxial detector, with a crystal that has a radius of 28.0 mm, a height of 65.2 mm, and an active volume of 160 cm^3 . Being extended range type, it has a beryllium window which is 99.8% pure and is 0.5 mm thick. The detector has a 32.4% relative efficiency, an energy resolution (FWHM) of 1.92 keV at 1.33 MeV, and a Peak to Compton ratio of 54.1. Detector 1 is shielded with multi-layer lead, tin, and copper shielding. The shielding is composed of an outer 120 mm layer of refined low background Pb, 3.5 mm of Sn, and an inner layer of 0.5 mm of a high purity Cu (Fig. 1). Measurements of samples 1 and 2 using Ge detector 1 were made for a distance of 0.5 cm between the bottom of the sample containers and the Be window.

Detector 2 is also a High Purity Germanium (HPGe) detector, made by CANBERRA with a serial mark GX5020. Its crystal has a radius of 31.8 mm and a height of 63.95 mm with an active volume of 200 cm^3 . The adjusted geometry model of the detector 2 was achieved by optimising the dead layer thickness in Monte Carlo simulations, the values



Fig. 2. Sample 1 and sample 2 in their containers.

are: top dead layer of 0.005 mm, side dead layer of 1.2 mm and a beryllium window 0.5 mm thick. It has a 50% relative efficiency and an energy resolution (FWHM) of 2.0 keV at 1.33 MeV. Detector 2 is encased in lead shielding of 16.5 cm thickness which ensures low background interference (around 1 cps). Measurements of samples 1 and 2 using Ge detector 2 were made for a distance of 6.6 cm between the bottom of the sample containers and the Be window. The samples were placed on an empty Marinelly beaker which was placed on the detector, providing the 6.6 cm distance.

2.2. Samples

In this study, 2 samples were analyzed. Both samples were taken from an abandoned mine shaft in the former uranium ore deposit Mazdreja, in the eastern part of Serbia. Sample 1 was a soil, orange in color, with a measured density of 0.801 g cm^{-3} and a mass of 20.72 g. Sample 2 was dark grey, almost black in color soil, with a measured density of 2.25 g cm^{-3} and a mass of 49.59 g (Fig. 2).

2.3. Iterative method

Iterative procedure is based on the constant density of the sample, while mass fractions of its constituents vary in each iteration. Iterative method is directly related to the variations of the mass fractions of different sample matrix constituents. The only value concerning sample composition that can be measured is its density. In order to determine mass fractions of sample constituents only one equation with one variable can be set up.

In sample 1 spectrum ^{232}Th series gamma peaks were completely missing and only gamma peaks from the first few radionuclides from the ^{238}U series were present. Based on this it was assumed that present radionuclides are not in their natural form and that they are most likely present as constituents of the industrially made yellowcake. However due to low sample density and the fact that only one equation with one unknown variable can be set up in the first iteration it was assumed that the sample consists of only air and soil.

Theoretical values used for soil and air were 1.4 g cm^{-3} and 0.00125 g cm^{-3} , respectively. Multiplying it with sample volume and dividing it with sample mass it is possible to determine mass fractions of sample constituents.

In sample 2 spectrum gamma lines from both ^{232}Th and ^{238}U series are present in their entirety. This means that soil is rich with radionuclides in the natural form. Based on the sample density it was assumed that the sample consists of industrially produced yellowcake and wet soil rich with radionuclides in their natural form.

It was determined that yellowcake mass is 22.55 g and soil mass is 27.04 g. It was approximated that wet soil consists of 30 % water and

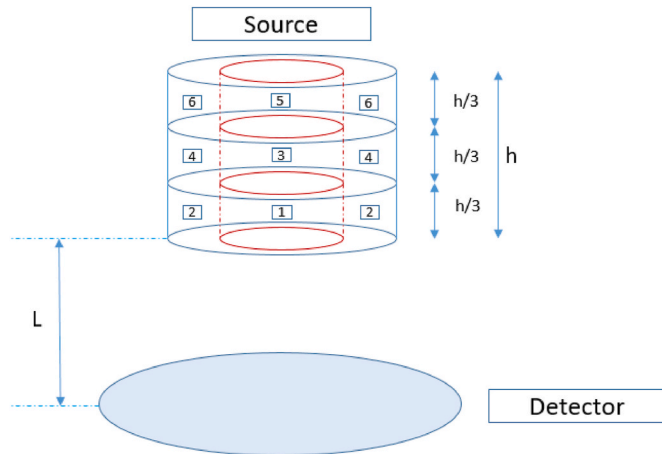


Fig. 3. Sample divided to 6 zones used in calculation.

70 % dry soil which means that it consists of 18.930 g of dry soil and 8.113 g of water. After determining mass fractions, samples can be defined in the LabSOCS library.

Coincidence summing correction factors for voluminous sources were determined by equation (1), derived from the method described in reference [Kolotov et al., 1996]. This method requires the source to be divided into several zones, equal in volume.

$$F_g = \frac{\sum_{i=1}^n \varepsilon_{i,g} V_i}{\sum_{i=1}^n f_g(z_i) V_i} \quad (1)$$

Factor F_g represents correction factor for coincidence summing at specific energy g for voluminous source, $\varepsilon_{i,g}$ is the efficiency of the detector on energy g for a zone enumerated with index i and $f_g(z_i)$ is experimentally determined coincidence summing correction factor for a point source at energy g (Fig. 3).

Detector efficiencies for each zone $\varepsilon_{i,g}$ are determined by calibration software LabSOCS. It is necessary to properly define the dimensions of each zone and its distance from the detector. The problem arises when it comes to defining zones enumerated with numbers 2, 4, and 6 because it is impossible to define its shape in LabSOCS software. In order to circumvent this setback instead of determining detector efficiency for zone 2, the efficiency of the bigger cylindrical zone that contains both zones 1 and 2 was determined. This bigger zone has the same contribution to the count rate as zones 1 and 2 combined. Detector efficiency for zone 2 can be calculated from the equation:

$$\varepsilon_2 = \frac{\varepsilon_{12}(V_1 + V_2) - \varepsilon_1 V_1}{V_2} \quad (2)$$

where ε_{12} represents detector efficiency for the zone containing zones 1 and 2. Detector efficiencies for other even zones can also be determined in the same way using LabSOCS software.

Correction factors as a function of the distance between detector and point sources $f_g(z_i)$ were determined in reference [Milošević et al., 2014; Djordjević, Milošević, 2012] using ^{235}U and ^{238}U point standards. Unlike point source standards, zones in this paper have a substantial volume that means that some parts of zones will be further from the detector than other parts. In order for functions $f_g(z_i)$ to be used correctly it is necessary to determine the average distance between each zone and the detector. This is achieved by determining the distance between two randomly chosen points, one is within the volume of the sample, and the second one is on the detector surface. Afterward, this expression is averaged by using integration across sample volume and detector surface. Potential problem with accurately computing detection efficiency is interference with self fluorescence x-rays on energy 92.59 keV that was reported by several authors [Murray et al., 1987]. As a consequence

of beta decay electron is emitted from the atom core. These electrons can interact with other atoms, decelerate and emit continuous bremsstrahlung radiation. Additionally, in thorium-rich samples these beta particles can eject an electron from the inner K shell of thorium atoms, a more loosely bound electron from the L shell then fills this vacancy. As a result of this, a deexcitation $K\alpha_1$ photon with an energy of 93 keV is emitted. This creates interference with the 92.59 keV peak [Kaste et al., 2006].

Due to interference with self-fluorescence X-rays on energies 92.59 keV and 63.29 keV, it is necessary to divide correction factors determined for these energies with a factor of 1.125. The activity of ^{238}U was determined in the equation below by using peaks at 63.29 keV, 92.59 keV, and 1001.03 keV

$$A = \frac{N}{t_m \varepsilon p_\gamma F} \quad (3)$$

A denotes the sample activity determined by a gamma peak at a specific energy, N represents count rates, t_m is acquisition time, p_γ is the yield of detected gamma rays and F is the correction factor for gamma peak of interest.

2.4. Semiempirical method

This method is also based on constant density of the samples. Using the methodology developed and described in [Vranićar et al., 2021], we used EFFTRAN and Geant4 software to obtain the detection efficiency function. Apart from the means of acquiring the efficiency function (separately and in different processes via EFFTRAN and Geant4 software), the method of calculating the mass activity of ^{238}U and ^{235}U are identical.

Initially, it was assumed that the uranium activity in the measured samples may come from uranium in different chemical forms - pure U, UO_2 , and U_3O_8 (if one does not have any prior knowledge of the origin or the chemistry of the samples, and also to test the impact of different matrix on the detection efficiency). In addition to this, the impact of different uranium mass contents in the sample on the efficiency function was tested, using Geant4 package.

In the sample 1, due to its density of 0.81 g cm^{-3} and intense orange color, as well as, the absence of ^{232}Th series gamma peaks, it was assumed that the uranium in this sample was in the form of yellowcake, i.e. U_3O_8 . The mass fraction of U_3O_8 was calculated to amount to 45.4%. Density of soil was taken to be 1.4 g cm^{-3} .

In the sample 2, considering its greater density of 2.25 g cm^{-3} and darker colour, it was assumed that the uranium could be present in different forms - i.e. U, UO_2 , and U_3O_8 . As noted in the section covering the iterative method, in sample 2 spectrum gamma lines from both ^{232}Th and ^{238}U series are present in their entirety. In this method, it was assumed that the sample consists of one form of uranium and soil. The mass fractions of different constituents are calculated based on the difference of the sample 2 density and the density of pure soil matrix, which is taken to be 1.4 g cm^{-3} . During every calculation it was assumed that each one of the constituents (U, UO_2 , and U_3O_8) is responsible for added sample density, and based on the densities of these three constituents (19.0 , 10.9 and 8.3 g cm^{-3} respectively) and the sample density, it was calculated that the mass fractions of U, UO_2 , and U_3O_8 are 40.8%, 43.4% and 45.4% respectively.

Taking into account that the discrepancies within resulting specific activities of ^{238}U and ^{235}U with this choice of sample matrices are not negligible (further discussion will be presented in *Results and Discussion*), sample matrix corrections had to be performed. Having this in mind, sample compositions obtained in second iteration in Iterative method were used and applied in further EFFTRAN and Geant4 calculation.

For the calibration purposes, certified Czech Metrology Institute standard type CBSS 2 was used as a reference material. It consists of a mixture of various radionuclides, with an energy interval of 59–1846 keV. These radionuclides are implanted in a silicon resin with known composition and a density of 0.985 g cm^{-3} . The Czech Metrology

Institute standard type CBSS 2 was packed in a cylindrical geometry with a diameter of 70 mm and a height of 69 mm.

2.5. Software

In this study, EFFTRAN, Geant4 and LabSOCS computer codes were used.

EFFTRAN is a mathematical software code that represents an implementation of the efficiency transfer method (ET) for cylindrical samples in gamma-ray spectrometry, based on a Monte Carlo integration of the interaction probabilities of gamma rays throughout the detector and sample volumes [Vidmar, 2005; Vidmar et al., 2010]. EFFTRAN software automatically calculates correction factors for true coincident summing effects, based on a sample geometry, detector model, and radionuclide of interest input [Vranicar et al., 2021].

Monte Carlo simulation, based on Geant4 simulation package [Agostinelli et al., 2003], has been developed to obtain the response of germanium detectors, with the aim to reproduce experimental spectra of detectors in a wide range of applications in gamma spectroscopy measurements [Joković et al., 2009; Krmar et al., 2013]. Geant4 allows the description of an experimental setup represented by a structure of geometrical volumes filled by given materials and associated with tracking media. In the simulation, germanium detectors, together with the whole detector assembly, are constructed in great detail, according to the manufacturer's data specifications. In the present work, the Geant4 software (version 4.9.5.) [Agostinelli et al., 2003] was used to obtain the detection efficiencies for different geometries of voluminous sources placed in front of the HPGe detector. In order to perform the simulations, the detector was modeled taking into account the technical features obtained from the manufacturer, except for the central void, whose size parameters were estimated [Nikolic et al., 2014]. For each gamma energy, 10^6 photons were generated isotropically from a certain source. The elemental composition, as well as density of the source matrices, were taken into account in simulations. The photopeak efficiency for each gamma energy was found as the ratio of the number of photons detected under photo-peak of given energy and the number of generated photons.

LabSOCS (Laboratory SOURCEless Calibration Software) is a commercial software used for mathematically determining the detection efficiency function of High Purity Germanium detectors [LabSOCS user manual, 2002]. Typically, LabSOCS software comes pre-paired with your Canberra detector, having all its parameters already predefined by its manufacturer. In our practice [Djordjevic, Milosevic, 2012], it has been shown that for cylindrical samples the difference in efficiency between the values obtained by this software and experimentally is less than 3%.

Spectrum analysis was done with GENIE 2000 software. It contains multiple packages, but in this work, Gamma Analysis Software and Interactive Peak Fit packages were used. Gamma Analysis Software is a package that contains a set of advanced algorithms for gamma spectrum analysis that are acquired by GENIE 2000 software. Interactive Peak Fit is a package that provides various tools for analyzing peaks in a given spectrum. This package is useful when acquiring complex spectrums, because of its capability of singlet or multiplet peak analysis, independently of the rest of the spectrum. It also provides the user with an option to manually fit any gamma peak (singlet or multiplet) [Vranicar et al., 2021].

2.6. Uncertainty budget

The combined relative measurement uncertainty for calculated sample activity, $u(A)$ was obtained according to the following equation:

$$u(A) = \sqrt{(\delta\varepsilon)^2 + (\delta N)^2 + (\delta p_\gamma)^2} \quad (4)$$

where $\delta\varepsilon$ represents relative uncertainty of the efficiency function fit

combined with the relative uncertainty of the radioactive solution of the secondary reference material and the uncertainty introduced in the process of production of the secondary reference material given by the manufacturer, used in efficiency transfer method, δN is the relative counting uncertainty, δp_γ is the yield uncertainty. The uncertainty introduced via t is negligible. Relative measurement uncertainty $u(A)$ for all energies did not exceed 10% at 2σ of confidence level.

In Geant4, during the calculation of measurement uncertainty, the following assumption was taken into account. The main variables that have been input into the simulation are 9 characteristic dimensions of the detector (crystal diameter and length, crystal cavity diameter and length, top and side dead layer, end-cap diameter, window thickness, and window to crystal gap) and 4 characteristics related to the sample (sample volume, sample and container material, namely density and chemical composition, and container to detector window gap). For these variables, except for the chemical composition of sample and container, the uncertainty can be estimated to be 1% for the geometry of crystal and container to detector window gap and 10% for window thickness and window to crystal gap. To minimize the discrepancy between simulated and measured values, bulletization, dead layer, and window to crystal gap was varied in the simulation, and the uncertainty was lowered to an estimated 1%. The chemical composition of the container is well defined, but for the sample, the situation is more complicated, and inadequate knowledge of the chemical composition of uranium ore, metallic plate, and UO_2 pellet can be the source of larger uncertainty. This is estimated to be 10% [Nikolic et al., 2014]. Regarding simulation, the relative uncertainty $u_{simulation}$ was calculated according to the following equation:

$$u_{simulation} = \sqrt{\sum (\delta x_i)^2} \quad (5)$$

where δx_i stands for the relative uncertainty of the value. In the calculation of the relative measurement uncertainty of the simulation, the variable x_i represents the Full Energy Peak Efficiencies (FEPE) that were individually simulated within Geant4 code for each energy, whereas δx_i represents the relative deviation of FEPE values calculated from simulation runs with a different number of generated events per run. The optimum number of events per run which yields good statistics with favorable uncertainty was found to be 10^6 events per run while keeping this uncertainty in the range of the mentioned 5%. Taking into account what is stated, the overall uncertainty of the simulated results is estimated to be 5%.

3. Results and discussion

3.1. Iterative method

3.1.1. Sample 1

The most reliable peak for determining uranium activity proved to be the "pure peak" at 1001.03 keV where only the true coincidence summing (TCS) correction factors had to be determined. It originates from the decay of ^{234m}Pa , the second daughter of ^{238}U .

Contributions to gamma peak 92.59 keV originate from the decay of ^{234}Th (^{238}U series) and ^{231}Th (^{235}U series). With the decay of ^{234}Th gamma rays 92.38 keV (2.31%) and 92.80 keV (2.1%) are emitted, alongside emission of gamma rays, X-ray 92.28 (0.0171%) is also emitted as a consequence of ^{234}Th decay. Decay of ^{231}Th is followed by emission of 93.02 keV (0.047%) gamma-ray and 92.282 keV x-ray which causes interference with photons emitted with the decay of ^{234}Th . It is necessary to subtract the ^{235}U series contribution from the total peak area. This contribution is calculated below:

$$N[92.59keV; 231Th] = A_{235U} \cdot t_m \cdot \varepsilon_{92.59} \cdot p_\gamma \quad (6)$$

where $\varepsilon_{92.59}$ is detector efficiency at 92.59 keV, p_γ is combined gamma-ray and x-ray emission probability and A_{235U} is the activity of ^{235}U .

Table 1
The activity concentration of Sample 1, iteration 1.

Radionuclide	Energy [keV]	Activity concentration [MBq kg ⁻¹]	Weighted activity [MBq kg ⁻¹]
²³⁸ U	63.29	1.66 ± 0.01	2.58 ± 0.21
	92.59	2.66 ± 0.17	
	1001.03	3.75 ± 0.23	
²³⁵ U	143.76	0.11 ± 0.01	0.119 ± 0.003
	163.33	0.12 ± 0.01	
	185.72	0.13 ± 0.01	

There are multiple methods for determining this activity, one of them is described in reference [Yücel et al., 2009]. However, we took a different approach and used the equation below:

$$A_{235U} = \frac{0.007204\lambda_{235}}{0.992742\lambda_{238}} A_{238U} (1001 \text{ keV}) \quad (7)$$

where 0.007204 and 0.992742 represent the natural abundance of ²³⁵U and ²³⁸U respectively, λ_{235} and λ_{238} are their decay constants and A_{238U} is ²³⁸U activity which was calculated by using a peak at 1001.03 keV.

²³⁸U series contributes to peak at 63.29 keV with the decay of ²³⁴Th, ²³⁴Pa, and ^{234m}Pa. Decay of ²³⁴Th produces gamma rays 62.86 keV (0.016%) and 63.29 keV (3.7%). Decays of ²³⁴Pa and ^{234m}Pa emit gamma-rays of 62.70 keV (0.0012% and 1.6% respectively). Interference is present due to decay of ²³¹Th, daughter of ²³⁵U. In this decay gamma-ray, 63.86 keV (0.023%) is emitted, its contribution is calculated below and it is necessary to be subtracted from the peak area.

$$N[63.29 \text{ keV}; ^{231}\text{Th}] = A_{235U} \cdot I_m \cdot \epsilon_{63.29} \cdot p_\gamma \quad (8)$$

where A_{235U} is the activity of ²³⁵U determined from equation (²³⁵U activity) and p_γ is emission probability of 63.86 keV gamma-rays.

²³⁵U activity can be calculated by using peaks at 143.76 keV, 163.33 keV, and 185.72 keV. Contributions to 143.76 keV peak in gamma spectrum originate from the decay of ²³⁵U and its daughters ²²³Ra and ²³¹Pa. With decay of ²³⁵U gamma rays 142.40 keV (0.005%) and 143.76 keV (10.96%) are emitted. With decay of ²²³Ra and ²³¹Pa gamma rays 144.4 keV (0.015%) and 144.235 keV (0.0327%) are emitted respectively. Additionally, with the decay of ²³⁴Pa, the daughter of ²³⁸U gamma-ray at 143.78 keV is emitted which causes interference with gamma rays from ²³⁵U and its daughters. This contribution needs to be subtracted from the spectrum count rate to obtain ²³⁵U chain contribution from equation (activity). ²³⁴Pa contribution is calculated below:

$$N[143.76 \text{ keV}; ^{234}\text{Pa}] = A_{238U} \cdot I_m \cdot \epsilon_{143.76} \cdot p_\gamma \quad (9)$$

where A_{238U} is the weighted activity of ²³⁸U based upon all 3 gamma peaks.

With the decay of ²³⁵U and its daughter, ²³¹Th gamma rays 163.356 keV (5.08%) and 163.1 keV (0.154%) are emitted respectively. Additionally, there is a small contribution from gamma line 164.94 keV which originates from the decay of ²³⁴Pa. Its contribution is calculated below and it needs to be subtracted from the 163.33 keV peak count rate from the spectrum.

$$N[163.33 \text{ keV}; ^{234}\text{Pa}] = A_{238U} \cdot I_m \cdot \epsilon_{163.33} \cdot p_\gamma \quad (10)$$

With the decay of ²³⁵U gamma-ray 185.72 keV (57.2%) is emitted and gives contribution to 185.72 keV peak in gamma spectrum. With the decay of ²³⁴Pa gamma-ray, 186.15 keV is emitted which causes interference. The contribution of ²³⁴Pa is calculated below and it needs to be subtracted from the peak area.

$$N[185.72 \text{ keV}; ^{234}\text{Pa}] = A_{238U} \cdot I_m \cdot \epsilon_{185.72} \cdot p_\gamma \quad (11)$$

Table 1 represents the activities of ²³⁵U and ²³⁸U determined using gamma peaks originating from their descendant, and their averaged weighted activity. A big discrepancy between these activities is present

which means our initial assumption concerning sample constituents was wrong. It is necessary to define the new sample composition in the second iteration to eliminate these discrepancies.

The activity of ²³⁸U that was used determined by using 1001.03 keV peak was used to determine the mass of ²³⁸U and U₃O₈ in the sample in the following equations:

$$m'_{238U} = \frac{A_{238U} (1001 \text{ keV}) \cdot A_m(^{238}\text{U})}{\lambda_{238} \cdot N_A} = 6.24 \text{ g} \quad (12)$$

$$m_{U_3O_8} = \frac{m'_{238U} (3 \cdot A_m(^{238}\text{U}) + 8 \cdot A_m(^{16}\text{O}))}{3 \cdot A_m(^{238}\text{U})} = 7.35 \text{ g} \quad (13)$$

Using U₃O₈ mass defined by equation (15) it is possible to calculate the mass of soil in the sample. Sample 1 in the second iteration was defined as 35.6% yellowcake and 64.4% dry soil in the LabSOCS library. It was necessary to repeat the entire procedure which consists of determining detector efficiency using the LabSOCS software, calculating correction factors, and calculating activities of ²³⁵U and ²³⁸U. The results of the second iteration are shown in Table 2. Activities determined from different peaks have similar values and their discrepancies from the weighted averaged activity are within borders of measurement uncertainty.

Table 2
Activity concentrations of Sample 1, iteration 2.

$$m'_{238U} = \frac{A'_{238U} \cdot A_m(^{238}\text{U})}{\lambda_{238} \cdot N_A} = 5.982 \text{ g} \quad (14)$$

$$m'_{235U} = \frac{A'_{235U} \cdot A_m(^{235}\text{U})}{\lambda_{235} \cdot N_A} = 0.043 \text{ g} \quad (15)$$

Radionuclide	Energy [keV]	Activity concentration [MBq kg ⁻¹]	Weighted activity concentration [MBq kg ⁻¹]
²³⁸ U	63.29	3.56 ± 0.22	3.59 ± 0.08
	92.59	3.65 ± 0.23	
	1001.03	3.59 ± 0.23	
²³⁵ U	143.76	0.16 ± 0.01	0.166 ± 0.005
	163.33	0.16 ± 0.01	
	185.72	0.17 ± 0.01	

3.1.2. Sample 2

In the sample 2, there are additional interferences that originate from the ²³²Th day chain and the remaining members of the ²³⁸U chain that weren't present in sample 1. These contributions also need to be taken into account when calculating uranium activity by subtracting them from the peak count rate in the spectrum. In order to determine the contribution of these radionuclides to various peaks, it was necessary to determine their activity first. These radionuclides are present in sample 2 in their natural form so it was assumed that radioactive equilibrium exists between members of the ²³²Th series and between members of the ²³⁸U series that are not present in yellowcake. The activity of the ²³²Th series members was determined using reference peaks of ²²⁸Ac at 338.3 keV, 911.3 keV, and 969.9 keV. The activity of ²²⁸Ac was determined by using the weighted averaged activity of these three peaks and activity of other radionuclides from the ²³²Th day chain was determined based upon radioactive equilibrium between them and ²²⁸Ac. An identical technique was employed in determining the activity of remaining radionuclides from the ²³⁸U chain, with three reference peaks of ²¹⁴Bi at 609.3 keV, 1120.3 keV, and 1764.5 keV.

Additional contributions were taken into account during activity calculations of ²³⁸U with the help of peaks at 63.29 keV (decay of ²³²Th which produced gamma-ray at 63.81 keV) and 92.59 keV (decay of ²²⁸Ac which produced gamma-ray at 93.35 keV). While calculating the activity of ²³⁵U with help of 185.72 keV peak it was necessary to

Table 3
Activity concentrations of Sample 2, iteration 1.

Radionuclide	Energy [keV]	Activity concentration [MBq kg ⁻¹]	Weighted activity concentration [MBq kg ⁻¹]
²³⁸ U	63.29	4.92 ± 0.31	5.96 ± 0.11
	92.59	5.38 ± 0.33	
	1001.03	6.63 ± 0.41	
²³⁵ U	143.76	0.25 ± 0.02	0.26 ± 0.06
	163.33	0.24 ± 0.01	
	185.72	0.30 ± 0.02	

additionally subtract contributions from ²²⁶Ra (186.21 keV) and ²²⁸Ac (184.54 keV). Based on the observations obtained from gamma spectra of the samples—the absence of post-radon gamma peaks (mainly 295.2 keV, 351.9 keV, and 609.3 keV) indicated that there is little to none ²²⁶Ra contribution to the 185.72 peak. The influence is negligible.

In the first iteration constituents of sample 2 were defined as 45.47% yellowcake, 38.17% soil, and 16.36% water. After detector efficiency and correction factors were determined the activity of sample 2 was calculated while taking into account all interference effects. Calculated activities in the first iteration are presented in Table 3.

Calculated activities for ²³⁸U for different peaks were not in alignment with each other so it was necessary to define new sample composition based upon activity determined using 1001.03 keV peak. New yellow cake mass was determined by equations (18) and (19) and based upon it new sample composition for the second iteration was determined as: 63.33% yellowcake, 25.67% soil, and 11% water.

$$m'_{238U} = \frac{A_{238U}(1001keV) \cdot A_m(^{238}U)}{\lambda_{238} \cdot N_A} = 26.47g \quad (16)$$

$$m_{U_3O_8} = \frac{m'_{238U} (3 \cdot A_m(^{238}U) + 8 \cdot A_m(^{16}O))}{3 \cdot A_m(^{238}U)} = 7.35g \quad (17)$$

After repeating the process, new activities were calculated and presented in Table 4.

Table 4
Activity concentrations of Sample 2, iteration 2.

$$m'_{238U} = \frac{A'_{238U} \cdot A_m(^{238}U)}{\lambda_{238} \cdot N_A} = 26.54g \quad (18)$$

$$m'_{235U} = \frac{A'_{235U} \cdot A_m(^{235}U)}{\lambda_{235} \cdot N_A} = 0.195g \quad (19)$$

Radionuclide	Energy [keV]	Activity concentration [MBq kg ⁻¹]	Weighted activity concentration [MBq kg ⁻¹]
²³⁸ U	63.29	6.61 ± 0.41	6.65 ± 0.12
	92.59	6.74 ± 0.42	
	1001.03	6.65 ± 0.41	
²³⁵ U	143.76	0.32 ± 0.02	0.315 ± 0.008
	163.33	0.31 ± 0.02	
	185.72	0.32 ± 0.02	

3.2. Semiempirical method

To make sure that the detection efficiency values acquired with Geant4 software are good enough, the efficiency transfer method was conducted in the following manner: the manufacturer characteristics of the detector were used with additional geometry adjustment (such as the

thickness of dead layers [Tsang et al., 2019], crystal distance from the window, etc.) with a goal to validate simulation results. The measured and simulated efficiency curves of the certified reference material CBSS 2 are presented in Fig. 4. On average, the deviation of the efficiency curve experimentally obtained from the certified standard source range falls under 8%. The adjusted detector characteristics were then used for all further calculations for investigated samples [Vranićar et al., 2021].

In Fig. 5, the results of the impact of different uranium mass contents in the sample on the efficiency function, using Geant4 package are presented. To test and see the influence of different uranium concentrations in sample matrices on detection efficiency curves, a set of arbitrary uranium concentration values was applied within the Geant4 code.

Uranium concentration values in sample matrices were taken to be 0–30% in various increments. From Fig. 5, one can derive that uranium concentration has a stronger impact in the low-energy of spectrum in regards to the high-energy region. A sudden drop in efficiency values that can be observed at 115 keV represents uranium's K-edge. The energies that are included in the analysis performed in this research lie out of the K-edge zone, so it is safe to assume that efficiencies used are unaffected by this phenomenon.

The results from the first approximation, i.e. that the uranium activity observed in gamma spectra of the two samples, comes from uranium in various chemical forms (U, UO₂, and U₃O₈), are given in Tables 5 and 6.

In Table 5, the first approximation for the activity concentrations of ²³⁵U and ²³⁸U for Sample 1 is presented. Taking into consideration its orange color and the lower density, it was assumed that the uranium in this sample comes in the form of U₃O₈. It can be seen that there is a significant discrepancy between activity concentrations calculated for energies 63.3 and 1001.03 keV, which indicates that the sample matrix is not well defined.

In Table 6, the first approximation for the activity concentrations of ²³⁵U and ²³⁸U for Sample 2 is presented. In this instance, having in mind the darker color, greater density as well as the presence of gamma lines from both ²³²Th and ²³⁸U series, it was presumed that the uranium activity in this sample may come in the form of U, UO₂ and U₃O₈. Significant discrepancy between activity concentrations calculated for energies 63.3 and 1001.03 keV is also present in this instance, as well as the difference in activity concentration values for different matrices, which depicts the influence of form and therefore, the concentration of uranium in the sample matrix.

Since there is a great discrepancy between the calculated ²³⁸U specific activity from low and high energies for Sample 1 and Sample 2, a different sample matrix had to be defined. Sample matrices from the second iteration in the iterative method were taken for calculation, in order to test and quantify the relative deviation in ²³⁵U and ²³⁸U specific activities, calculated by using different methods. These results are presented in Figs. 6 and 7 and Tables 7 and 8.

From Tables 7 and 8, it can be seen that even though calculated ²³⁸U activities from 63.3 to 1001.03 keV by both EFFTRAN and Geant4 software slightly differ from the ones obtained by the iterative method for Sample 2 if one observes the values of calculated ²³⁸U activities from 63.3 to 1001.03 keV by individual software, a good agreement between activity values for mentioned energies is found. From Fig. 7, it can be seen that EFFTRAN software gives underestimated activity concentration values, although judging from the activity values from 63.3 to 1001.03 keV, it is observed that a good sample matrix was defined. In the case of sample 1, a good agreement between all methods is observed. Discrepancies between activity values are not greater than 15%.

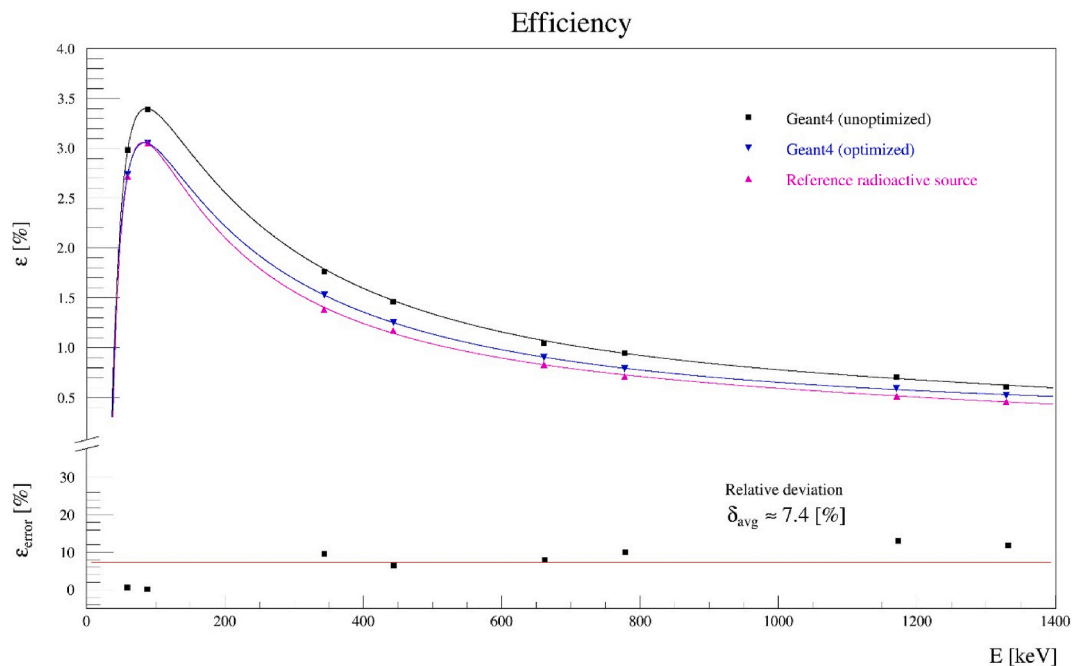


Fig. 4. Efficiency curves for experimental and simulated certified reference material CBSS 2.

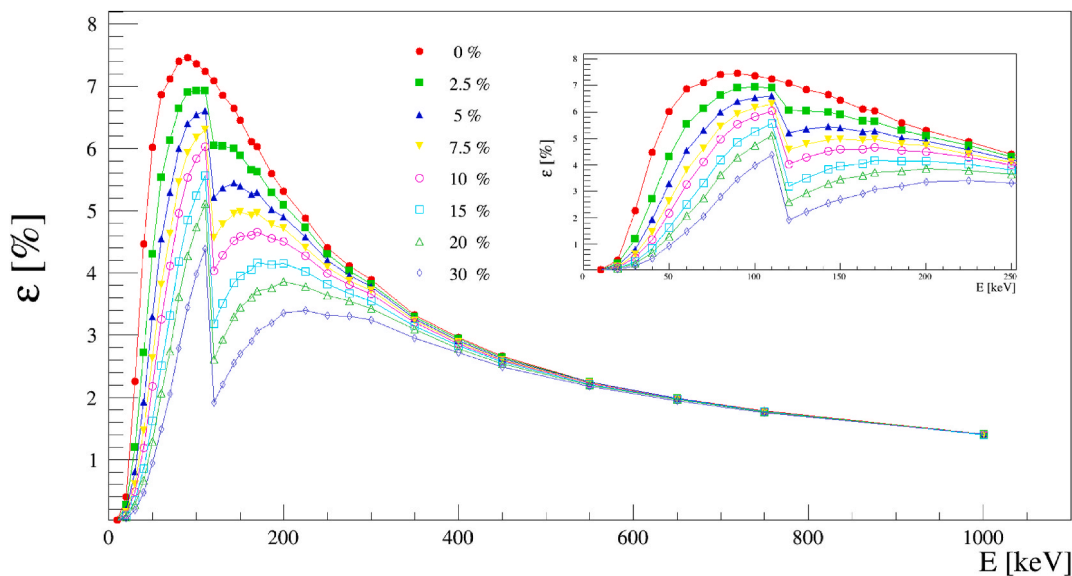


Fig. 5. Influence of different uranium mass content in the sample on the efficiency curve in Geant4.

Table 5
Activity concentrations of ²³⁵U and ²³⁸U for Sample 1 (0.81 g cm⁻³) in first approximation.

Matrix	Software	Radionuclide	Energy [keV]	Activity concentration [MBq kg ⁻¹]
U ₃ O ₈	EFFTRAN	²³⁸ U	63.3	3.93 ± 0.23
			1001.03	3.33 ± 0.20
		²³⁵ U	143.8	0.18 ± 0.01
			163.3	0.19 ± 0.01
			185.7	0.19 ± 0.01
			185.7	0.18 ± 0.01
	Geant4	²³⁸ U	63.3	4.39 ± 0.26
			1001.03	3.58 ± 0.21
		²³⁵ U	143.8	0.19 ± 0.01
			163.3	0.18 ± 0.01
			185.7	0.18 ± 0.01
			185.7	0.18 ± 0.01

4. Conclusion

In this study, for the purpose of determining the specific activity of ²³⁸U, gamma peaks on 63.3 keV (²³⁴Th), and 1001.03 keV (^{234m}Pa) with the addition of 92.6 keV gamma peak (²³⁴Th) in iterative method were used, while for the specific activity of ²³⁵U, we used the gamma peaks on 143.8 keV, 163.3 keV and 185.7 keV and using the information about natural abundance of ²³⁵U and ²³⁸U. Samples analyzed within this research were found in the former uranium ore deposit Mazdreja in Eastern Serbia, and deducted to be yellowcake and either dry or wet soil mixture.

Obtained results proved that it is of great importance to adjust the sample matrix in order to obtain correct results. As seen in Tables 7 and 8 and Figs. 6 and 7, all three methods gave comparable results, with a margin of error between Activity concentration results not greater than

Table 6
Activity concentrations of ²³⁵U and ²³⁸U for Sample 2 (2.25 g cm⁻³) in first approximation.

Matrix	Software	Radionuclide	Energy [keV]	Activity concentration [MBq kg ⁻¹]	
U	EFFTRAN	²³⁸ U	63.3	3.75 ± 0.23	
			1001.03	5.65 ± 0.34	
		²³⁵ U	143.8	0.24 ± 0.01	
			163.3	0.24 ± 0.01	
			185.7	0.27 ± 0.02	
	Geant4	²³⁸ U	63.3	4.84 ± 0.30	
			143.8	0.24 ± 0.01	
		²³⁵ U	163.3	0.24 ± 0.01	
			185.7	0.24 ± 0.01	
			1001.03	6.09 ± 0.37	
	UO ₂	EFFTRAN	²³⁸ U	63.3	3.55 ± 0.22
				1001.03	5.67 ± 0.35
			²³⁵ U	143.8	0.23 ± 0.01
				163.3	0.23 ± 0.01
				185.7	0.26 ± 0.02
Geant4		²³⁸ U	63.3	4.56 ± 0.28	
			1001.03	6.07 ± 0.38	
		²³⁵ U	143.8	0.23 ± 0.01	
			163.3	0.23 ± 0.01	
			185.7	0.24 ± 0.01	
U ₃ O ₈		EFFTRAN	²³⁸ U	63.3	3.57 ± 0.22
				1001.03	5.67 ± 0.35
			²³⁵ U	143.8	0.23 ± 0.01
				163.3	0.23 ± 0.01
				185.7	0.26 ± 0.02
	Geant4	²³⁸ U	63.3	4.60 ± 0.28	
			1001.03	6.07 ± 0.36	
		²³⁵ U	143.8	0.23 ± 0.01	
			163.3	0.23 ± 0.01	
			185.7	0.24 ± 0.01	

Table 7
Activity concentrations of ²³⁵U and ²³⁸U for Sample 1 (0.81 g cm⁻³) in second approximation.

Software	Radionuclide	Energy [keV]	Activity concentration [MBq kg ⁻¹]
LabSOCS	²³⁸ U	63.3	3.56 ± 0.19
		1001.03	3.59 ± 0.20
	²³⁵ U	143.8	0.16 ± 0.01
		163.3	0.16 ± 0.01
		185.7	0.17 ± 0.01
EFFTRAN	²³⁸ U	63.3	3.30 ± 0.19
		1001.03	3.44 ± 0.20
	²³⁵ U	143.8	0.16 ± 0.01
		163.3	0.17 ± 0.01
		185.7	0.18 ± 0.01
Geant4	²³⁸ U	63.3	3.65 ± 0.18
		1001.03	3.63 ± 0.21
	²³⁵ U	143.8	0.17 ± 0.01
		163.3	0.17 ± 0.01
		185.7	0.18 ± 0.01

Table 8
Activity concentrations of ²³⁵U and ²³⁸U for Sample 2 (2.25 g cm⁻³) in second approximation.

Software	Radionuclide	Energy [keV]	Activity concentration [MBq kg ⁻¹]
LabSOCS	²³⁸ U	63.3	6.61 ± 0.41
		1001.03	6.65 ± 0.42
	²³⁵ U	143.8	0.32 ± 0.02
		163.3	0.31 ± 0.02
		185.7	0.32 ± 0.02
Geant4	²³⁸ U	63.3	6.11 ± 0.38
		1001.03	6.19 ± 0.38
	²³⁵ U	143.8	0.29 ± 0.02
		163.3	0.29 ± 0.02
		185.7	0.30 ± 0.02
EFFTRAN	²³⁸ U	63.3	5.41 ± 0.34
		1001.03	5.83 ± 0.35
	²³⁵ U	143.8	0.29 ± 0.02
		163.3	0.28 ± 0.01
		185.7	0.30 ± 0.02

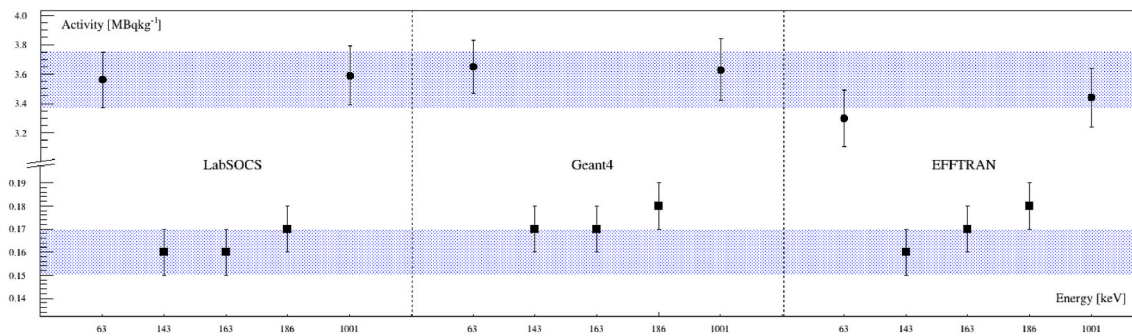


Fig. 6. Activity concentrations of ²³⁵U and ²³⁸U for Sample 1 obtained by Iterative and semiempirical methods.

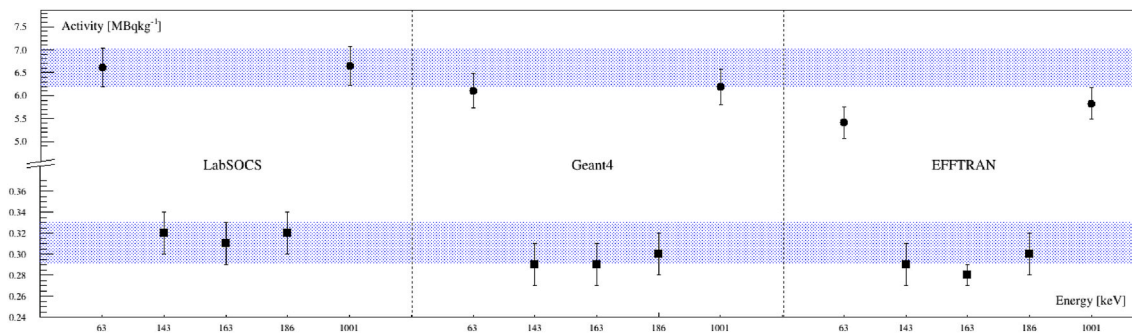


Fig. 7. Activity concentrations of ²³⁵U and ²³⁸U for Sample 2 obtained by iterative and semiempirical methods.

15%. Although EFFTRAN results slightly differ from the ones of iterative method and Geant4 software, it should be noticed that this software obtains the results in a quicker manner than the mentioned two. In that light, it presents a good tool for a quick screening method, which gives fast activity concentration results with satisfying confidence levels.

The overall conclusion is that if we need a precise results of activity concentration of an unknown sample, the more thorough study must be conducted as it was shown by iterative method. Contrary to this, if the fast determination of result is needed while precision in activity concentration is not of great importance, then the efficiency transfer method can give a valuable contribution.

In order to perform more detailed validation of the obtained results, the chemical composition of the samples should be measured by some more precise methodology and that could be a next step in the future investigation of this topic.

CRedit author statement

Andrej Vranić: Methodology, Formal analysis, Investigation, Writing - Original Draft; Jovana Nikolov: Conceptualization, Writing - Review & Editing, Supervision; Đorđe Lazarević: Methodology; Aleksandar Rikalo: Formal analysis, Writing - Original Draft; Nataša Todorović: Validation, Methodology; Dalibor Arbutina: Resources, Conceptualization; Miloš Travar: Software, Formal analysis, Investigation, Writing - Original Draft.

Declaration of competing interest

The authors declare that they have no known competing financial interests or personal relationships that could have appeared to influence the work reported in this paper.

Acknowledgment

The authors acknowledge the financial support of the International Atomic Energy Agency (IAEA) via IAEA Research Contract No. 23159/R0 and of the Ministry of Education, Science and Technological Development of the Republic of Serbia (Grant No. 51-03-9/2021-14/200125).

References

- Agostinelli, S., et al., 2003. Geant 4—a simulation toolkit. *Nucl. Instrum. Methods A* 506, 250–303.
- Djordjević, I., Milošević, M.J., 2012. Numerical calibration of Ge detector for coincidence summing effect determination. In: *Proceedings of 56th Conference ETRAN. NT1.5, Zlatibor, Serbia, pp. 1–4. June 11- 14 (in serbian)*.
- Dowdall, M., et al., 2004. Simultaneous determination of ^{226}Ra and ^{238}U in soil and environmental materials by gamma-spectrometry in absence of radium progeny equilibrium. *J. Radioanal. Nucl. Chem.* 261, 513–521.
- Kaste, James M., Bostick, Benjamin C., Heimsath, Arjun M., 2006. Determining ^{234}Th and ^{238}U in rocks, soils, and sediments via the doublet gamma at 92.5 keV. *Analyst* 131 (6), 757–763.
- Kolotov, V., Atrashkevich, V., Gelsema, S., 1996. Estimation of true coincidence corrections for voluminous sources. *J. Radioanal. Nucl. Chem.* 210 (1), 183–196. <https://doi.org/10.1007/bf02055417>.
- Milošević, M., Maksimović, I., Cekerevac-Mirković, D., 2014. Merenje aktivnosti uranijuma, Zbornik 58. konferencije za elektroniku, telekomunikacije, računarstvo, automatiku i nuklearnu tehniku (in Serbian) proc. 58th ETRAN Conference, Vrnjačka Banja. ISBN 978-86- 80509-69-3.
- Murray, A., et al., 1987. Analysis for naturally occurring radionuclides at environmental concentrations by gamma spectrometry. *J. Radioanal. Nucl. Chem.* 115 (2), 263–288. <https://doi.org/10.1007/bf02037443>.
- Nikolic, J., Vidmar, T., Jokovic, D., Rajacic, M., Todorovic, D., 2014. *Nucl. Instrum. Methods Phys. Res.* 763, 347–353.
- Tsang, R.H.M., Piepke, A., Auty, D.J., Cleveland, B., Delaquis, S., Didberidze, T., MacLellan, R., Meng, Y., Nusair, O., Tolba, T., 2019. GEANT4 models of HPGe detectors for radioassay. *Nucl. Instrum. Methods Phys. Res.* 935 <https://doi.org/10.1016/j.nima.2019.04.085>. ISSN 0168-9002 2019.
- Vidmar, T., 2005. EFFTRAN—a Monte Carlo efficiency transfer code for gamma-ray spectrometry. *Nucl. Instrum. Methods Phys. Res. Sect. A Accel. Spectrom. Detect. Assoc. Equip.* 550 (3), 603–608. <https://doi.org/10.1016/j.nima.2005.05.055>.
- Vidmar, T., et al., 2010. Testing efficiency transfer codes for equivalence. *Appl. Radiat. Isot.* 68, 355–359. ISSN: 0969-8043.
- Vranićar, A., Nikolov, J., et al., 2021. Testing of EFFTRAN and Angle software in comparison to GEANT 4 simulations in gamma spectrometry of cylindrical and noncylindrical sample geometries. *Nucl. Instrum. Methods Phys. Res. A* 986. <https://doi.org/10.1016/j.nima.2020.164768>. ISSN 0168-9002.
- Yücel, H., Çetiner, M.A., Demirel, H., 1998. Use of the 1001 keV peak of $^{234\text{m}}\text{Pa}$ daughter of ^{238}U in measurement of uranium concentration by HPGe gamma-ray spectrometry. *Nucl. Instrum. Methods A* 413 (1), 74–82.
- Yücel, H., Solmaz, A.N., Köse, E., Bor, D., 2009. Spectral interference corrections for the measurement of ^{238}U in materials rich in thorium by a high resolution γ -ray spectrometry. *Appl. Radiat. Isot.* 67 <https://doi.org/10.1016/j.apradiso.2009.07.011>. ISSN 0969-8043.

Forbush decrease events associated with coronal mass ejections: Classification using machine learning

M.R. Savić[✉], N.B. Veselinović, A.L. Dragić, D.M. Maletić,
R.M. Banjanac, D.R. Joković, D.Knežević, M.Travar and
V.I. Udovičić

*Institute of Physics Belgrade, University of Belgrade, Pregrevica 118,
11080 Belgrade, Serbia (E-mail: msavic@ipb.ac.rs)*

Received: September 27, 2023; Accepted: October 22, 2023

Abstract. In presented work we further explore previously indicated possibility of the existence of two classes of Forbush decrease events, established by the prior analysis of the correlation between the shape of energetic proton fluence spectra and Forbush decrease properties. In an attempt to increase statistical robustness of the analysis and potentially reduce the uncertainties, we have developed an alternative classification procedure that employs machine learning and utilizes space weather parameters as input variables. Based on the overall performance, efficiency and flexibility of different machine learning methods we selected the best performing algorithm and established the optimal boundary value of Forbush decrease intensity to be used for class separation. A subset of good input variables was selected based on their predictive power.

Key words: cosmic rays – Forbush decrease – coronal mass ejection – solar energetic particles

1. Introduction

The dynamic activity of the Sun's coronal magnetic field can give rise to complex space weather events. These events may include solar flares (SFs), coronal mass ejections (CMEs), their interplanetary counterparts known as interplanetary coronal mass ejections (ICMEs), the emission of solar energetic particles (SEPs), and similar phenomena (Kahler, 1992; Yashiro & Gopalswamy, 2008; Gopalswamy, 2022).

One such complex event can produce a number of effects in the heliosphere, one of which is the acceleration of solar wind particles. There is a distinction between particles accelerated by a SF in the lower Sun's atmosphere and those accelerated locally by the CME shock. The later are often referred to as energetic storm particles (ESPs) (Desai & Giacalone, 2016).

Additionally, the passage of a CME can affect the primary cosmic rays (CRs) potentially resulting in a sudden drop in the observed CR flux, followed by a

recovery phase that takes place over the several following days. This effect is known as a Forbush decrease (FD) and can be observed by Earth-based CR detectors.

A previous study of the relationship between transient modulations in the fluxes of energetic protons and cosmic rays (measured near and at Earth respectively) indicated an existence of two classes of FD events (Savić et al., 2023). The main objective of this work is to expand this analysis and investigate whether a specific set of space weather (SW) parameters can be successfully used as input parameters for classification. The proposed procedure would aim to separate FD events into classes as indicated by the aforementioned analysis, while increasing the statistical significance and potentially the reliability of the analysis. Additional positive outcome of a successful classification would be the selection of a subset of SW parameters that prove to be good input variables. These variables could then be further used for the prediction of FD magnitudes utilizing some regression algorithm.

2. Motivation

As simultaneous ESP and FD events are very likely a consequence of the passage of an ICME, a relationship between them was assumed. To establish this possible connection, correlation of characteristics of proton fluence spectra and FD parameters was investigated (as described in more detail in Savić et al. (2023)).

The proton fluence spectra were calculated from in situ measurements at L1 by SOHO/ERNE instrument (Torsti et al., 1995), and fitted by a double-power law, as shown for one selected event on Figure 1.

Exponents obtained from these fits were used to parameterize the spectra shape, and some degree of correlation between these exponents and FD magnitudes was established. However, this analysis also indicated a possible existence of two classes of FD events, as illustrated in Figure 2. The plot shows the dependence of the FD magnitude corrected for the magnetospheric effect on one of the proton fluence spectra exponents. The green oval indicates a supposed class of events that exhibit a stronger correlation between these two variables, while the red oval indicates a class of events where this correlation is apparently weaker. One possible way to define the boundary between these two classes could be by introducing a cut on the intensity of the event.

Due to relatively low statistics of events where proton fluence can be reliably determined, one idea for extending this analysis is to try and utilize other space weather parameters in order to increase statistics and more strongly establish the assumed existence of two classes of FD events.

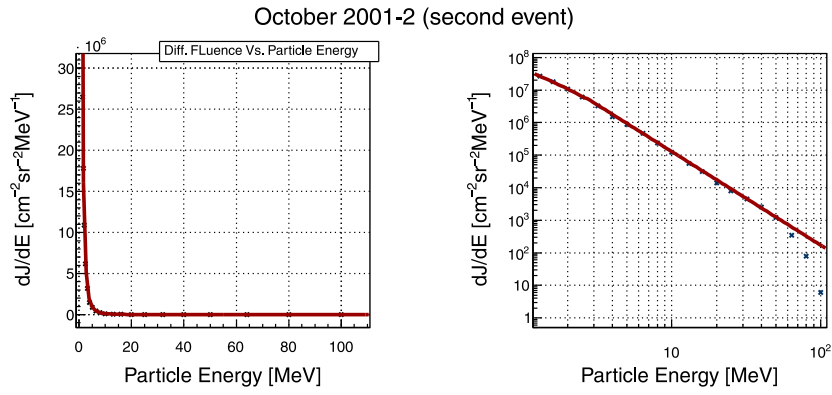


Figure 1. Proton fluence spectra at L1 for one event during October 2001, in linear (left) and logarithmic scale (right).

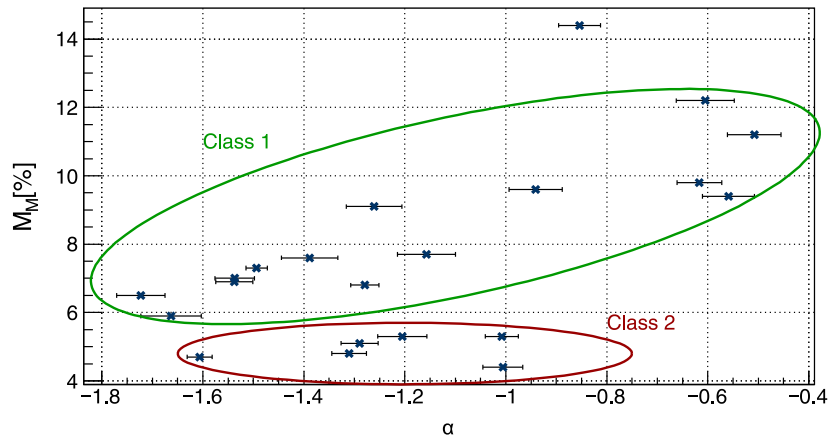


Figure 2. The dependence of the FD magnitude corrected for the magnetospheric effect (M_M) on one of the exponents used to parameterize the proton fluence spectra (α). Two assumed classes of FD events are indicated by the green and red ovals.

3. Methods and Results

IZMIRAN catalogue of Forbush effects (IZMIRAN, 2016) was used as the source of SW related data, as it contains an extensive list of FD events and associated SW parameters. The parameters selected from the IZMIRAN catalogue to be used in the analysis presented here fall into several categories: parameters describing the source (Otype, Stype) or the characteristics of the CME (Vmean, CMEwidth); solar wind parameters (Vmax, KTmax, KTmin); parameters describing interplanetary or geomagnetic field (Bzmin, Kpmax, Apmag, Dstmin); and parameters related to the associated solar flare (Xmagn, Sdur, SSN).

Several machine-learning-based classification methods implemented in the TMVA analysis network (Hoecker et al., 2007) were employed in order to establish the optimal FD magnitude for the separation of two classes (boundary criteria mentioned in Section 2), as well as to determine the optimal classification algorithm. Comparing the efficiency of various methods available in the TMVA (shown of Figure 3), it was found that the optimal separation between two classes is achieved with FD magnitude cut set to 6%, as separation efficiency seems to drop-off beyond that for most methods. Support vector machine (SVM) (Cortes & Vapnik, 1995) was identified as the overall best-performing algorithm.

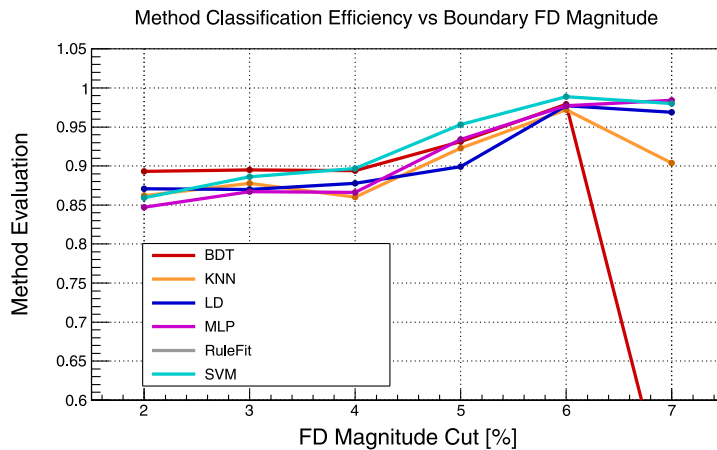


Figure 3. Comparison of the classification efficiency of various TMVA methods dependence on the FD magnitude cut used for class separation.

SVM implementation in the scikit-learn package (Pedregosa et al., 2011) was utilized to identify which of the SW parameters could reliably classify FD events. Third-degree polynomial kernel was found to have the most flexible and efficient performance.

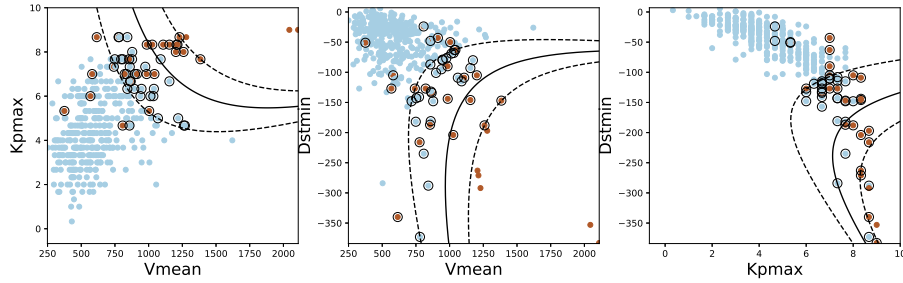


Figure 4. Example of SVM classification using some of SW parameters (mean CME velocity, maximum Kp index and minimal Dst index over the event's duration) that proved to be good input variables for FD classification.

Obtained results appear to confirm the assumption regarding the existence of two classes of FD events. Furthermore, a subset of SW parameters that provide a more reliable classification of FD events was determined. These include mean CME velocity (V_{mean}) and geomagnetic indices (K_{pmax} , A_{pmax} , D_{stmin}), with a possible inclusion of the solar wind speed (V_{max}) and minimal hourly component of the interplanetary magnetic field (B_{zmin}). Decision boundaries between some pairs of mentioned good input variables are showed on Figure 4. Other SW variables proved to be less well suited for classification (as illustrated in Figure 5, for K_{Tmin} and K_{Tmax}).

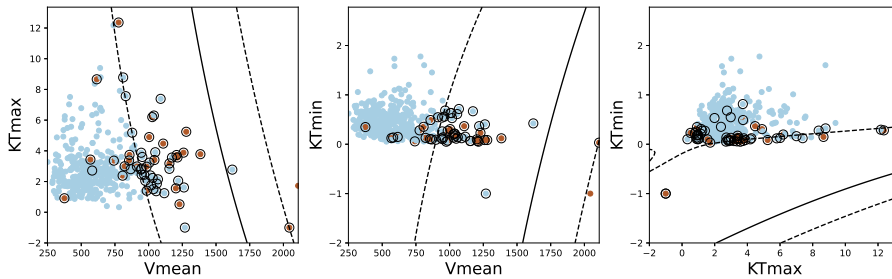


Figure 5. Example of SVM classification using some of SW parameters (K_{Tmax} , K_{Tmin}) that proved to be less well suited input variables for FD classification.

The identified good variables could prove useful in a potential future extension of the analysis. More specifically, they could serve as an input for a regression procedure that would potentially allow the prediction of FD magnitudes.

This prediction would provide either estimates of FD magnitude as measured by Earth-based detectors or, more importantly, estimates of FD magnitudes corrected for the magnetospheric effect.

4. Conclusions

The potential existence of two classes of FD events was investigated. To increase statistical robustness and reduce uncertainties, the analysis was expanded to include a wider set of various space weather parameters. Machine learning techniques were employed in an attempt to separate FD events into two assumed classes, using a number of selected SW parameters as input variables. We compared the efficiency of different machine learning algorithms, and established the optimal boundary value of FD intensity to be used for class separation. The SVM algorithm was selected for the analysis based on its overall performance, efficiency and flexibility, and used to select a subset of space weather variables to be used for reliable classification of FD events. This subset of good variables could prove useful for a future extension of the analysis, where they would provide an input for a regression procedure used to predict FD magnitudes.

Acknowledgements. This work was funded by the Institute of Physics Belgrade, University of Belgrade, through a grant by the Ministry of Science, Technological Development and Innovations of the Republic of Serbia.

We kindly acknowledge the usage of data from the SOHO experiment, as well as data from the catalogue of Forbush effects and interplanetary disturbances provided by the IZMIRAN Space Weather Prediction Center.

References

- Cortes, C. & Vapnik, V., Support Vector Networks. 1995, *Machine Learning*, **20**, 273
- Desai, M. & Giacalone, J., Large gradual solar energetic particle events. 2016, *Living Reviews in Solar Physics*, **13**, 3, DOI: 10.1007/s41116-016-0002-5
- Gopalswamy, N., The Sun and Space Weather. 2022, *Atmosphere*, **13**, DOI: 10.3390/atmos13111781
- Hoecker, A., Speckmayer, P., Stelzer, J., et al., TMVA - Toolkit for Multivariate Data Analysis. 2007, *arXiv e-prints*, physics/0703039, DOI: 10.48550/arXiv.physics/0703039
- IZMIRAN. 2016, Space weather prediction center (IZMIRAN), <http://spaceweather.izmiran.ru/eng/index.html>
- Kahler, S. W., Solar flares and coronal mass ejections. 1992, *Annual Review of Astronomy and Astrophysics*, **30**, 113, DOI: 10.1146/annurev.aa.30.090192.000553
- Pedregosa, F., Varoquaux, G., Gramfort, A., et al., Scikit-learn: Machine Learning in Python. 2011, *Journal of Machine Learning Research*, **12**, 2825

- Savić, M., Veselinović, N., Dragić, A., et al., New insights from cross-correlation studies between solar activity indices and cosmic-ray flux during Forbush decrease events. 2023, *Advances in Space Research*, **71**, 2006, DOI: 10.1016/j.asr.2022.09.057
- Torsti, J., Valtonen, E., Lumme, M., et al., Energetic Particle Experiment ERNE. 1995, *Solar Physics*, **162**, 505, DOI: 10.1007/BF00733438
- Yashiro, S. & Gopalswamy, N., Statistical relationship between solar flares and coronal mass ejections. 2008, *Proceedings of the International Astronomical Union*, **4**, DOI: 10.1017/S1743921309029342

Analyzing solar activity with Belgrade muon station: case study of 2021 November 4th Forbush decrease

N.B. Veselinović^{ORCID}, M.B. Savić, D.M. Maletić, A.L. Dragić,
R.M. Banjanac, D.R. Joković, D. Knežević, M. Travar and
V.I. Udovičić

*Institute of Physics Belgrade, University of Belgrade, Pregrevica 118,
11080 Belgrade, Serbia, (E-mail: veselinovic@ipb.ac.rs)*

Received: September 19, 2023; Accepted: October 16, 2023

Abstract. The first significant Forbush decrease of the solar cycle 25 was recorded on November 4th, 2021. The Forbush decrease was observed with numerous ground based cosmic rays stations including Belgrade cosmic rays muons' station. Series of coronal mass ejections during October 28–November 4 2021. produce conditions for this Forbush decrease. We discuss here the variation of cosmic rays' flux detected with ground-based detectors and connection with conditions, measured in-situ, in interplanetary space around Earth, flux of solar wind protons measured with SOHO probe to assess implication for solar-terrestrial coupling processes.

Key words: Cosmic rays – Forbush decrease – Space weather – muon detector

1. Introduction

One of the methods of researching solar-terrestrial coupling processes is observing the response of the flux of cosmic rays (CR) to various types of disturbances (or drivers) in the heliosphere. Transient phenomena detected in CR flux due to modulation in the heliosphere is the Forbush decrease: a sudden drop in CR flux followed by a gradual return to the previous level. It occurs as CR interact with irregularities in the interplanetary magnetic field (IMF), usually connected with the emission of coronal plasma known as a coronal mass ejection (CME) and its interplanetary counterpart (ICME) (Yermolaev et al., 2021). In recent decades, space probes have measured IMF parameters in-situ as well as particle flux. The detected particles can be fast-moving particles, known as solar energetic particles (SEPs), related to violent eruptions from the Sun that can cause a sudden increase in measured CR flux at the surface - a ground level enhancement (GLE). The other particles detected with probes, aside from solar wind particles and SEPs, are energetic storm particles (ESP) accelerated locally by shocks driven by fast ICMEs (Desai & Giacalone, 2016) and low-energy CR

(Veselinović et al., 2021). It has been shown (Koldobskiy et al., 2019; Savić et al., 2023; Kolarski et al., 2023) that parameters measured in-situ correlate with the magnitude and time evolution of FD. The end of October and the beginning of November 2021 marked extreme activity with a strong X-class solar flare (CIT), accompanied by the first Ground Level Enhancement (GLE) event in this cycle on October 28th, measured by several ground stations (Papaioannou, A. et al., 2022). There were several typical CMEs during this period. Most pronounced were two halo CMEs on October 28th and November 2nd. The second halo CME, due to its speed, caught up with previous ICMEs and produced a CME-CME interaction (Li et al., 2022). These disturbances created additional modulation of CR, producing the first strong FD in the present solar cycle, detected by multiple ground stations around the globe (Chilingarian et al., 2022).

The present case-study combines in-situ measurements of solar wind parameters and proton flux in near-Earth space with measurements on the ground to analyze how these parameters affect parameters of the FD detected on November 4th, 2021.

2. Ground level cosmic ray observations

The most widely method of detecting CR use detectors that are part of the worldwide network of Neutron Monitors (NM) (<https://www.nmdb.eu/nest/>). One of the other species of these secondary CR that can be detected and used for monitoring primary CR are muons.

2.1. Belgrade muon detector

The ground level Belgrade muon station (GLL) is a part of the Low-Background Laboratory for Nuclear Physics at the Institute of Physics, Belgrade, Serbia. The energy range of the observed primary CR extends and complements the energy ranges detected by the NM network, but is still sensitive to CR modulation of the heliosphere. Details of the experimental setup, as well as the calculated response function of the detectors, are presented in (Veselinović et al., 2017).

2.2. Ground level data analysis

Both NM and muon detectors measure integral flux over different energy ranges, so the median energy of the detected primary CR is used in the analysis of the measured data. Another property of the detector system is Cut-off rigidity, the minimal magnetic rigidity that the CR must have in order to penetrate the IMF and geomagnetic field. To determine the amplitude of the FD for each station, which differs in median energy and asymptotic direction, a baseline was established using the average hourly count rate during mid-October 2021 when solar activity was low. For this study, we utilized 1-hour time series of CR flux detected at 17 NM stations and GLL data (Table 1).

Table 1. Cut-off rigidity (R_c) and median energy (E_m) of primary CR for several stations.

Stations	R_c (GV)	E_m (GeV)	Stations	R_c (GV)	E_m (GeV)
Belgrade	5.3	63	Kerguelen	1.14	10.4
Athens	8.53	17.8	Oulu	0.8	10.3
Guadalajara	6.95	15.4	Apatity	0.65	10.3
Baksan	5.6	13.7	Norilsk	0.63	10.3
Jungfrauoch	4.5	12.6	Tixie Bay	0.5	10.2
Lomnický štít	3.84	12	Fort Smith	0.3	10.2
Dourbes	3.18	11.5	Inuvik	0.3	10.2
Kiel	2.36	11	S. Pole bare	0.1	10.1
Yakutsk	1.65	10.6	S. Pole	0.1	10.1

Median energy for NM was found using formula given in [Li et al. \(2023\)](#) and median energy for GLL was found using Monte Carlo method of CR transport. Dependence of FD amplitude on CR median energy is given by power law ([Cane, 2000](#))

$$\frac{\Delta N}{N} = E^{-a} \quad (1)$$

Here N is CR flux, E is median energy and a is power exponent that depends on heliospheric conditions.

A scatter plot of the selected event is given ([Figure 1](#)) plotted in log-log scale and it shows clear median rigidity dependence of the amplitude of FD.

Steeper spectrum during this event shows greater modulation of primary CR. If GLL data is included in the plot, the power exponent is not so large so that can be interpreted as stronger modulation of the lower energy CR due to CME-CME interaction. Linear regression is performed to find power indices corresponding to November 2021 event. Power index for NM only is 1.23 ± 0.22 and for NM and GLL power index is 0.62 ± 0.10 . This is, in general, in good agreement with some previous studies ([Lingri et al. \(2016\)](#) and references within).

3. Relation to in-situ measured data

In this study we used measured in-situ parameters relevant for heliospheric studies which are available at GSFC/Space Physics Data Facility, in the form of 1-hour resolution OMNI data (<https://spdf.gsfc.nasa.gov/pub/data/omni/lowresomni/>). Also we used proton flux data gathered by SOHO probe with two detectors, ERNE and EPHIN, onboard SOHO probe ([Torsti et al., 2000](#); [Kühl & Heber, 2019](#)) at Lagrange point 1 in vicinity of Earth. Comparison between 1-hour time series of selected parameters of IMF from OMNI data and

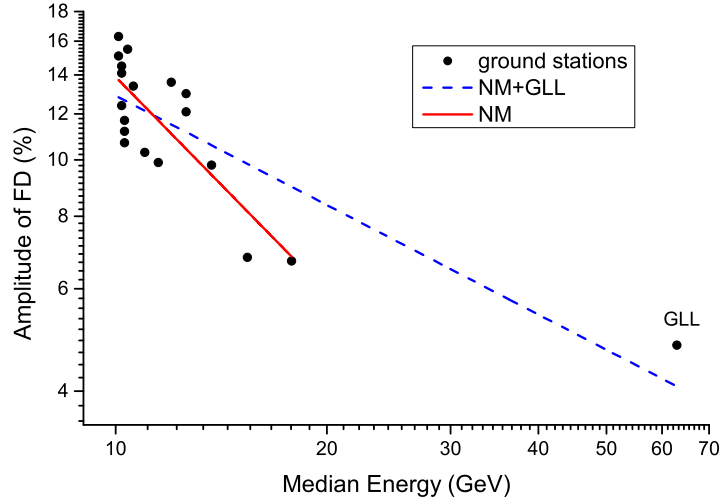


Figure 1. Rigidity spectrum of FD from November 4th 2021. Points represent the amplitude of the Forbush decrease as seen by 18 NMs and Belgrade GLL muon station.

relative detected CR flux of NM with low cut-off rigidity at South Pole and Belgrade muon detector and similar comparison for the same time interval between CR flux detected with two ground level detectors and selected channels of SOHO/ERNE and SOHO/EPHIN proton flux data is shown in Figure 2.

The discrepancies between time series of CR flux detected with ground stations and parameters of the IMF shows that CR was influenced by complex interactions in the heliosphere where low energy proton flux detected in-situ with detectors on board SOHO does not contribute substantially either to condition in heliosphere or CR flux. Increase of SEP flux, apparent in all detected proton flux from SOHO/ERNE and SOHO/EPHIN, produce GLE event detected with NM with low cut-off rigidity. Shape of detected FD on different stations varied, as expected due to difference cut-off rigidity, median energy, detector design, and sensitivity.

Correlation between respective time series was found using Pearson correlation coefficient using 2-tail test for significance is given at Table 2.

As expected correlation of CR flux is greater for NM detector at South Pole due to lower energy of detected CR which are more sensitive to disturbances of IMF. Inverse correlation of average magnetic field and solar wind plasma speed with CR flux is expected due to scattering of CR on turbulent magnetic field that produce a decrease in detected CR flux. The lack of correlation between proton fluxes and higher energy CR flux detected with GLL shown that monitor only some of the proton energy channel is not sufficient to model FD over range of CR energies during complex event with CME-CME interaction. Modeling of

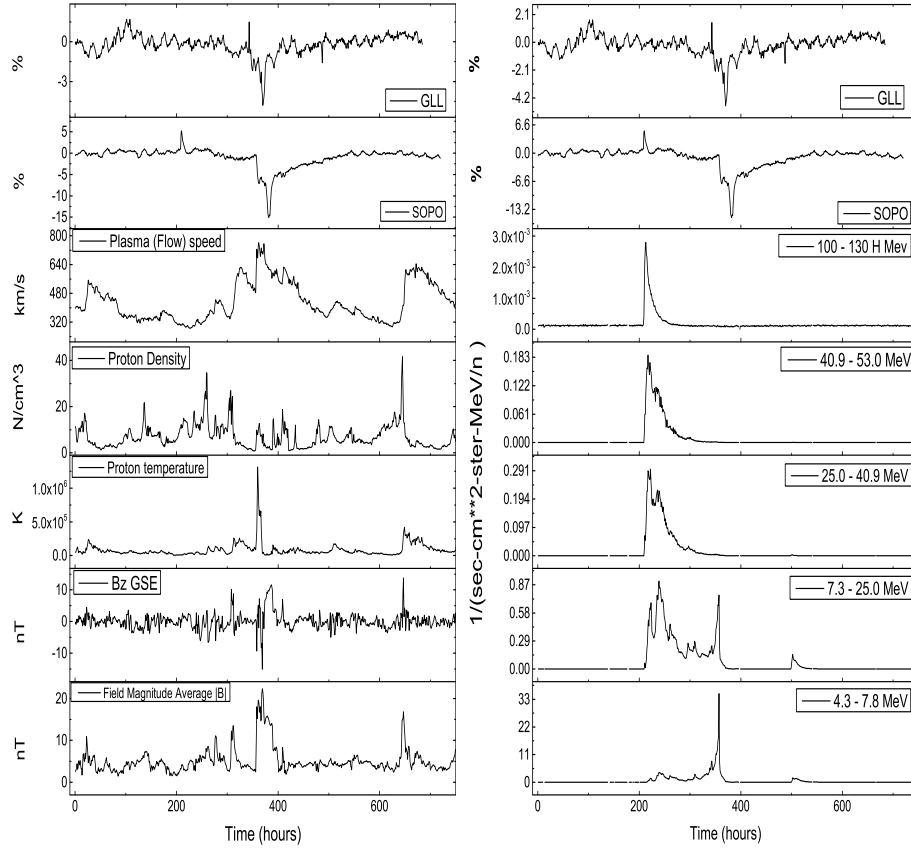


Figure 2. Left: Time series for plasma parameters (taken from OMNI database) and cosmic ray flux (measured at South Pole NM and GLL) from October 20th until November 20th, 2021. Right: Hourly time series for different proton energy channels from SOHO/ERNE and SOHO/EPHIN and two CR detectors time series for the same period.

this complicated shock-associated ICME disturbance where multiple shocks and transient flows merged is challenging and other studies (Zhao & Zhang, 2016; Werner et al., 2019) showed similar complex dependence of CR flux on different parameters of the IMF condition.

4. Summary

In this work we studied the FD occurred in November 4th, 2021, using data from Belgrade muon station and other multiple sources. Increased solar activity at the beginning of the November 2021 had a measurable effect on CR, observed as a

Table 2. Pearson correlation coefficients for the correlation between CR flux detected at Belgrade CR station (GLL), at South pole (SOPO), flux of protons of different energies from SOHO/ERNE and SOHO/EPHIN and plasma parameters (from OMNI database) for the period from October 20th until November 20th, 2021.

	SOPO		GLL	
	Pearson Corr.	p-value	Pearson Corr.	p-value
SOPO	1		0.52	$<10^{-5}$
GLL	0.52	$<10^{-5}$	1	
B Average	-0.55	$<10^{-5}$	-0.48	$<10^{-5}$
Bz	-0.4	$<10^{-5}$	-0.15	$<10^{-4}$
Proton temperature	-0.18	$<10^{-5}$	-0.23	$<10^{-5}$
Proton Density	0.23	$<10^{-5}$	0.14	$<10^{-4}$
Plasma (Flow) speed	-0.61	$<10^{-5}$	-0.53	$<10^{-5}$
7.3-25.0 MeV p	0.17	$<10^{-5}$	-0.12	0.002
4.3-7.8 MeV p	0.01	0.67	-0.29	$<10^{-5}$
25.0-40.9 MeV p	0.21	$<10^{-5}$	0.02	0.5
40.9-53.0 MeV p	0.21	$<10^{-5}$	0.03	0.45
80-100 H MeV p	0.22	$<10^{-5}$	0.03	0.37

decrease in measured flux by all relevant CR stations. Energy range of affected primary CR was wide enough so effect was detected by neutron monitors but also muon detectors. Rapid decrease was detected with CR detectors around the world and it was one of the consequence, along with the strong G3-class geomagnetic storm, auroras and GLE event, of series of overlapping CMEs. We showed that based on measured amplitude of FD of the range of ground station that higher energy CR was less affected with heliospheric disturbance. Cross correlations between time series of CR flux and IMF and solar wind characteristics during these strongly disturbed heliospheric conditions were presented. Lack of strong correlation is also apparent for higher energy CR flux time series and time series of the heliospheric parameters and proton flux of certain energy ranges. This proves that, in order to better understand solar-terrestrial coupling processes, particularly its effect for higher energy particles requires more data from various sources and various probes and this analysis can be done in the future.

Acknowledgements. The authors acknowledge funding provided by the Institute of Physics Belgrade, through the grant by the Ministry of Science, Technological Development and Innovations of the Republic of Serbia. We also acknowledge use of NASA/GSFC's Space Physics Data Facility's OMNIWeb (or CDAWeb or ftp) service, and OMNI data as well as team behind SOHO, which is a project of international collaboration between ESA and NASA. We acknowledge the NMDB database, founded under the European Union's FP7 program (contract no.213007) for providing data.

References

- Cane, H. V., Coronal Mass Ejections and Forbush Decreases. 2000, *Space Science Reviews*, **93**, 55, DOI: 10.1023/A:1026532125747
- Chilingarian, A., Hovsepyan, G., Martoyan, H., et al. 2022, Forbush decrease observed by SEVAN particle detector network on November 4, 2021
- Desai, M. & Giacalone, J., Large gradual solar energetic particle events. 2016, *Living Reviews in Solar Physics*, **13**, 3, DOI: 10.1007/s41116-016-0002-5
- Kühl, P. & Heber, B., Revising More Than 20 Years of EPHIN Ion Flux Data-A New Data Product for Space Weather Applications. 2019, *Space Weather*, **17**, 84, DOI: <https://doi.org/10.1029/2018SW002114>
- Kolarski, A., Veselinović, N., Srećković, V. A., et al., Impacts of Extreme Space Weather Events on September 6th, 2017 on Ionosphere and Primary Cosmic Rays. 2023, *Remote Sensing*, **15**, DOI: 10.3390/rs15051403
- Koldobskiy, S. A., Bindi, V., Corti, C., Kovaltsov, G. A., & Usoskin, I. G., Validation of the Neutron Monitor Yield Function Using Data From AMS-02 Experiment, 2011-2017. 2019, *Journal of Geophysical Research: Space Physics*, **124**, 2367, DOI: <https://doi.org/10.1029/2018JA026340>
- Li, W.-h. et al., A study of Forbush Decreases effects with DAMPE experiment. 2023, *PoS, ICRC2023*, 1311, DOI: 10.22323/1.444.1311
- Li, X., Wang, Y., Guo, J., & Lyu, S., Solar Energetic Particles Produced during Two Fast Coronal Mass Ejections. 2022, *The Astrophysical Journal Letters*, **928**, L6, DOI: 10.3847/2041-8213/ac5b72
- Lingri, D., Mavromichalaki, H., Belov, A., et al., Solar Activity Parameters and Associated Forbush Decreases During the Minimum Between Cycles 23 and 24 and the Ascending Phase of Cycle 24. 2016, *Solar Physics*, **291**, 1025, DOI: 10.1007/s11207-016-0863-8
- Papaioannou, A., Kouloumvakos, A., Mishev, A., et al., The first ground-level enhancement of solar cycle 25 on 28 October 2021. 2022, *A&A*, **660**, L5, DOI: 10.1051/0004-6361/202142855
- Savić, M., Veselinović, N., Dragić, A., et al., New insights from cross-correlation studies between solar activity indices and cosmic-ray flux during Forbush decrease events. 2023, *Advances in Space Research*, **71**, 2006, DOI: <https://doi.org/10.1016/j.asr.2022.09.057>, recent progress in the physics of the Sun and heliosphere
- Torsti, J., Mäkelä, P., Teittinen, M., & Laivola, J., SOHO/Energetic and Relativistic Nucleon and Electron Experiment Measurements of Energetic H, He, O, and Fe Fluxes during the 1997 November 6 Solar Event. 2000, *The Astrophysical Journal*, **544**, 1169, DOI: 10.1086/317219
- Veselinović, N., Dragić, A., Savić, M., et al., An underground laboratory as a facility for studies of cosmic-ray solar modulation. 2017, *Nuclear Instruments and Methods in Physics Research Section A: Accelerators, Spectrometers, Detectors and Associated Equipment*, **875**, 10, DOI: <https://doi.org/10.1016/j.nima.2017.09.008>

- Veselinović, N., Savić, M., Dragić, A., et al., Correlation analysis of solar energetic particles and secondary cosmic ray flux. 2021, *The European Physical Journal D*, **75**, 173, DOI: 10.1140/epjd/s10053-021-00172-x
- Werner, A. L. E., Yordanova, E., Dimmock, A. P., & Temmer, M., Modeling the Multiple CME Interaction Event on 6–9 September 2017 with WSA-ENLIL+Cone. 2019, *Space Weather*, **17**, 357, DOI: <https://doi.org/10.1029/2018SW001993>
- Yermolaev, Y. I., Lodkina, I. G., Dremukhina, L. A., Yermolaev, M. Y., & Khokhlachev, A. A., What Solar-Terrestrial Link Researchers Should Know about Interplanetary Drivers. 2021, *Universe*, **7**, DOI: 10.3390/universe7050138
- Zhao, L.-L. & Zhang, H., Transient galactic cosmic-ray modulation during solar cycle 24: A comparative study of two prominent Forbush decrease events. 2016, *The Astrophysical Journal*, **827**, 13, DOI: 10.3847/0004-637X/827/1/13



Detailed optimization procedure of an HPGe detector using Geant4 toolkit

M. Travar¹ · J. Nikolov¹ · N. Todorović¹ · A. Vraničar¹ · P. Völgyesi² · P. Kirchknopf² · I. Čeliković³ · T. Milanović³ · D. Joković⁴

Received: 26 November 2022 / Accepted: 27 January 2023 / Published online: 5 March 2023
© Akadémiai Kiadó, Budapest, Hungary 2023

Abstract

Presented study describes the optimization method of an HPGe detector through implementation of Geant4 toolkit. The optimized model was verified through comparison with experimentally obtained data using a set of point-like radioactive calibration sources. Acquired results displayed good agreement with the experimental data that falls under an average relative deviation of the order of ~2% within the energy range of 53–1836 keV. Additionally, in order to test the validity of the code it was also applied to a different detection equipment where an average relative deviation of the order of ~1.8% was achieved within the energy range of 121–1112 keV.

Keywords HPGe detector · γ -Spectrometry · FEP efficiency · Geant4 model · Monte Carlo simulation

Introduction

Over the years, High Purity Germanium (HPGe) detectors proved to be an excellent practical tool and as such have established their today's wide use in low background γ -spectrometry. One of the more significant advantages of γ -spectrometry is its easy sample preparation as chemical processing and separation of the studied subject is not always required. Therefore, with a single measurement, one can simultaneously perform both qualitative and quantitative analysis [1].

One of the most prominent features of HPGe detectors is their superior resolution. This feature virtually allows researchers to perform a thorough analysis by discriminating photons of similar energies in the studied spectra where otherwise they would superimpose within a single-energy

peak and as such would scathe analysis and produce wrongly assessed results. Naturally, this comes as of great importance when identification of radionuclides, as well as their activity concentrations, is being performed where high precision comes as a necessity [2].

Performance and reliability of HPGe systems depends, amongst other factors, on the quality of their calibration. In particular, performing radionuclide identification requires good energy calibration, while on the other hand to be able to obtain high-quality characterization of the activities one would require an accurate understanding and knowledge on the full-energy-peak (FEP) efficiency appropriate to specific conditions under which the measurement was carried out. This efficiency represents complex function that is characterized not only by detectors specifications but also by the aforementioned measuring conditions. Detailed information on the FEP efficiencies could be experimentally obtained using standard calibration sources. However, this carries certain difficulties. Namely, it is a question of availability of sources that have same or similar composition, as well as same or similar counting geometry as the studied sample. This may not always be physically or economically feasible, and can sometimes be difficult and time consuming. In turn, this led many of the research groups to turn towards the use of different software toolkits that implement Monte Carlo method. When applied along with γ -spectrometry Monte Carlo simulations provide means to determine the detectors

✉ J. Nikolov
jovana.nikolov@df.uns.ac.rs

¹ Faculty of Sciences, University of Novi Sad, Trg Dositeja Obradovića 3a, 21000 Novi Sad, Serbia

² Centre for Energy Research, Konkoly-Thege Miklós út. 29-33, Budapest, Hungary

³ Institute for Nuclear Sciences Vinča, Mike Petrovića Alasa 12-16, 11000 Belgrade, Serbia

⁴ Institute for Physics, University of Belgrade, Pregrevica 18, 11000 Belgrade, Serbia

response function for any new given measuring geometry or matrix without the need of additional standard calibration sources, optimizing in that way both time and financial resources. Thus, Monte Carlo approach comes as a reliable solution with little to no expense depending on the software of choice [3].

Monte Carlo simulations

Today there is a handful of Monte Carlo codes available to the scientific community, but the ones most commonly used for the purpose of detector optimization are MCNP (Monte Carlo N-Particle code, LoS Alamos National Laboratory [4]) and Geant4 (GEometry ANd Tracking4, CERN [5]). Besides the two, there are other commercially available codes that utilize and combine both absolute approach to FEP efficiency calculations by means of Monte Carlo simulations as well as relative approach by means of experimental comparison with well-known sources (LabSOCS [6], ANGLE [7], EFFTRAN [8], etc.). A detailed optimization procedure of a co-axial extended range (XtRa) HPGe detector based on application of Geant4 toolkit, with accent on the dependencies of FEP efficiency values on certain detector parameters, is presented within this work.

Geant4: a brief overview

Geant4, first introduced back in 1998, is an open-source software toolkit that can accurately simulate the passage of particles through matter. Design choice for this code was an object-oriented methodology and C++ language in order to provide the user with a modular and flexible software. Unlike its previous instalment Geant3, which was not able to simulate particles with energies below 10 keV, Geant4 can simulate electromagnetic processes down to 250 eV. This feature can greatly influence the accuracy when low-energy γ -spectrometry simulations are being performed [9].

Geant4 code includes facilities for handling geometry, tracking, run management, visualization, detector response and user interface (UI). Unlike other computational Monte Carlo codes such as MCNP [4], FLUKA [10], PENELOPE [11], etc., Geant4 is not an executable program but rather a set of C++ class libraries that users must implement on their own. In order to build a simulation code, one must describe through these classes the geometry of the setup (shapes and materials used, sensitive components), generation of primary particles as well as the production of relevant secondary particles (their type, energy, momentum, charge), physics processes, etc. Hence, a firm knowledge in object-oriented programming is required [9].

Utility of Geant4 reflects in its ability to trace the history of each individual particle which consists of its emission by the radioactive source, its interaction with the detector and

surrounding materials and the production and transport of secondary particles. As such, the code can directly determine energy deposition in the simulated scoring volume of the detector, allowing one to perform FEP efficiency calculations. Since no approximations are needed there are no limitations to sample-detector configurations. However, the accuracy of the simulated efficiencies is largely affected by incomplete parameters of the detector. Generic characterization provided by the manufacturer is usually insufficient, since some of the parameters are unknown or sometimes not even related to the specific detector but are instead rather averaged over a set of the detectors of the same or similar type. Consequently, many studies reported large deviations between the simulated and experimentally obtained FEP efficiencies when nominal values provided by manufacturer were used (well over 10–20%). This in turn demands the optimization of the detector model to be carried out in order to achieve better agreements. Beside this, one of the main disadvantages of the code in the past was its time scale for generating sufficient number of events in order to achieve good statistical uncertainties of the order of 1% or less. This issue is complemented with today's available hardware where significant improvements have been made in terms of computational times thanks to significant increase in the computational power due to use of parallel computing, computer clusters, supercomputers, etc.

Version of Geant4 used for optimization procedure presented in this work was 4.10.0.7. To significantly reduce computational times the simulation code was written in multithreading mode. Based on data provided by the manufacturer (Table 2) initial model of the detector was made using a variety of geometry classes that Geant4 provides. Parameters supplied by the manufacturer were taken as constant while other parameters were taken as free that would undergo further adjustments.

Geant4 also provides a variety of classes that describe physics processes. Low-energy electromagnetic package valid down to energy of 250 eV was used in this study (G4EmLivermorePhysics). This package facilitates processes necessary for performing low energy γ -ray spectrometry, some of which are: Compton and Rayleigh scattering, photo-electric effect, pair production, fluorescence and Auger effect, bremsstrahlung and ionization, etc.

Materials and methods

Optimization procedure

The most notable detector parameters that can significantly influence FEP efficiency calculations, and which are not always provided, are the so-called dead layers. These layers are formed by diffusion of contact material (usually

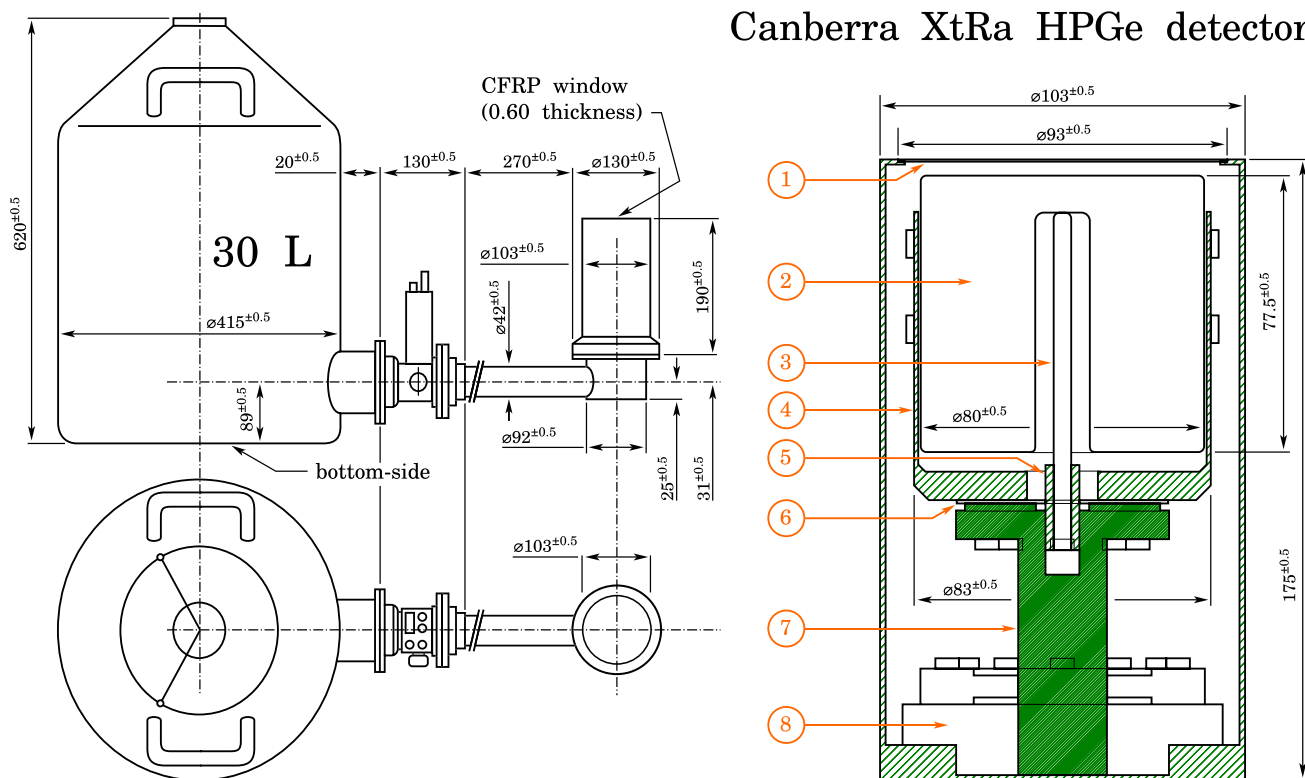


Fig. 1 Schematic diagram of the HPGe detector (XtRa—extended range, model no. GX10021, Canberra, Mirion Inc.) and its cooling system (U-type of cryostat configuration, model no. 7915-30-ULB, Canberra, Mirion Inc.). Values given in mm

Table 1 Components and materials (refer to Fig. 1)

Components	Material
Entry-window	cfrp*
Ge-crystal	Ge
Inner contact pin	Cu
Crystal cup holder	Cu
CN nut	Al
Alumina	Al
Cold finger	Cu
Lead shielding	Pb

*Carbon-fiber-reinforced polymer (1.42 g/cm³ density)

lithium) into the germanium crystal. However, they cannot simply be quantified as the depth of Li-diffused atoms. They are described as layers consisting of actual dead layer (with no charge collection) and partially active or effective dead layer (with low charge collection efficiency). Thickness of these layers depends on the impurity level of germanium crystal as well as the electrode production process. Dead layers virtually act as absorbing layers, shielding the crystal and effectively decreasing its active volume. Over time, they increase as a consequence of

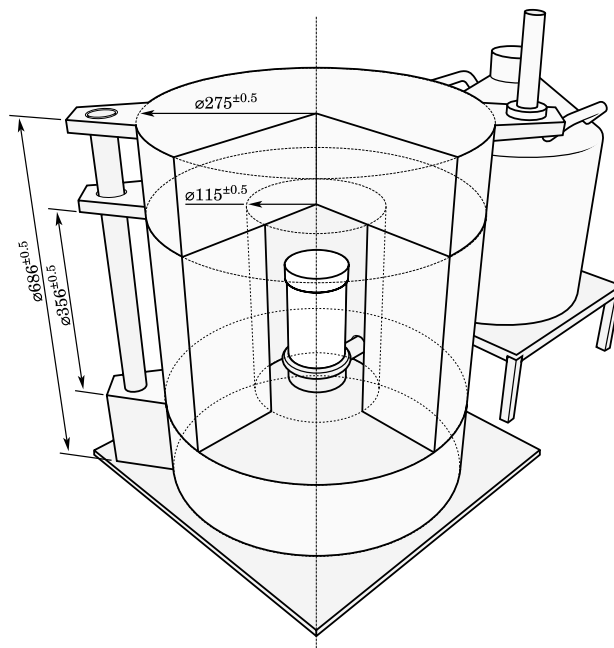


Fig. 2 3D model of the detector with its cooling system and commercial passive shielding in which it is installed

continuous diffusion of Li-atoms, making it important to be precisely quantified especially when working with older equipment. For p-type HPGe detectors these layers play a significant role and have to be properly taken into account. In contrast, for n-type detectors also known as Reverse Electrode Ge-detectors (REGe), the outer dead layer is much thinner and doesn't represent a significant modification in the simulation model. Other than this, there is also the possibility of other parameters deviating from the values they were initially assigned by the manufacturer, some of which are the diameter or length of the crystal, crystal-to-window distance, inner crystals cavity dimensions, the rounding of the crystal (bulletization), thickness of the entry window, etc. Any change of these parameters can have an impact on the efficiency values. Thus, to improve on the accuracy an optimization procedure needs to be carried out [12].

Generally, there are two approaches one could adopt when optimizing a model. First one involves an accurate determination of the geometrical parameters using various techniques that include x/γ-ray radiography scans. With these, a detailed imaging of the inner structure of their equipment can be obtained and thus greatly facilitate optimization (refer to “LEGe detector optimization” section). Even though this approach can be extremely precise, its application is difficult for many laboratories as the required equipment for this may not always be available. Second approach involves an experimental calibration of a simple configuration after which one tries to adjust the parameters in the simulation in order to obtain better results. Many of the studies that performed the latter approach [1–3, 9, 12–17] report agreements that typically fall within an average uncertainty of 5% or less within the studied energy range. Main advantages of this approach is its simplicity and quick implementation. However, it brings certain downsides as well. Namely, there is no guarantee that the optimized model actually matches the one in reality as there is no reference to take from and since efficiencies depend on more than one factor, it is also possible that multiple configurations yield satisfactory results for a given setup. With this in mind, the optimized model for one counting geometry would not necessarily be reliable for a different one. Therefore, it is advised to perform the optimization for each new counting configuration.

Experimental setup

In this study a low-background γ-spectrometer with coaxial p-type HPGe detector (XtRa, model no. GX10021, Canberra, Mirion Inc.) was used. Figure 1 illustrates technical drawing of the detector with its components listed in Table 1. A 3D model of the equipment along with its commercial

Table 2 Information on the detectors specification and performance data provided by the manufacturer

<i>Specifications</i>	
Detector model	GX10021
Cryostat model	7915-30-ULB
Preamplifier model	2002C
<i>Physical characteristics</i>	
Crystal diameter	80 mm
Crystal height	77.5 mm
End-to-cap distance	5 mm
Active volume	0.6 mm
Inner cavity height	/
Inner cavity diameter	/
Top dead layer	/
Inner dead layer (p + contact)	/
Lateral dead layer (n + contact)	/
<i>Electrical characteristics</i>	
Depletion voltage	3000 Vdc
Recommended bias voltage Vdc	(+) 3500 Vdc

Table 3 Point-like radioactive source along with their activities and respective uncertainties (Ritverc co.)

Source	Activity (kBq)	Uncertainty (%)
Mn-54	57.23	3
Co-57	45.52	3
Co-60	74.55	3
Y-88	1.781	3
Cd-109	57.03	3
Ba-133	83.33	3
Eu-152	88.48	3
Am-241	40.84	3

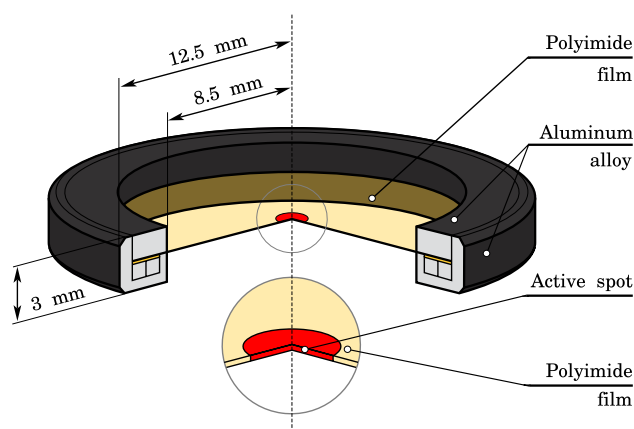


Fig. 3 Ritverc co. point-like standard gamma calibration sources

shielding and cooling system is illustrated in Fig. 2. Table 2 lists detectors nominal values provided by the manufacturer.

This detector has a relative efficiency of 100% and an energy resolution of 1.20 keV and 2.1 keV at energies 122 keV and 1332 keV, respectively. Most conventional p-type co-axial detectors come with a lithium diffused contact of typically 0.5–1.5 mm thickness which is more than enough to stop most of the photons below 40 keV energies. However, the entry window present with XtRa offers all the advantages of standard co-axial detector, as well as the energy response in low-energy region of the more expensive REGe detectors. In our case the entry window is made of highly durable carbon composition in the form of carbon epoxy, which allows the transmission of more than 85% for photons of energies above 15 keV and nearly 100% for those of energies above 20 keV.

The detector is installed within commercial passive shielding in order to achieve low background needed in environmental applications (Canberra, Mirion Inc., model type 777B). This shielding consists of (from inside to outside) a thin layer of copper and tin, followed by lead layer of 150 mm thickness and a layer of low-carbon steel of 10 mm thickness. Thin layers of copper and tin play a role of passive shielding of x-rays produced by transitions on K-shell of lead (75–85 keV energy region). The presence of x-rays in tin in the energy region of 25–28 keV is reduced by the presence of copper layer. Lead layer is made of 125 mm outer layer which contains standard low-radioactive lead while the inner layer of 25 mm thickness contains ^{210}Pb with activities less than 20 Bq/kg. As such, this type of passive shielding offers significant reduction of surrounding background (mainly from ^{40}K and ^{208}Tl) as well as reduction to the contribution of the annihilation line at 511 keV.

Acquisition of gamma spectra was driven by Genie2K™ software [18]. All of spectra were recorded in mode of 16,384 channels with the energy width per channel of

178.4 eV and with the upper energy threshold set to detect photons of energies up to 3 MeV. Acquisition time for each measured spectrum was adjusted as such to keep the statistical uncertainty of the interested peak area below 1% with dead-times for all measurements standing less than 4%.

Experimental calibration of the equipment was carried out using a set of point-like standard gamma calibration radioactive sources (Table 3, Fig. 3). These sources are hot sealed between two polyimide foils of total thickness of $100 \pm 10 \mu\text{m}$ placed in aluminium capsule in the form of a ring of 3 mm thickness and 25 mm diameter. The active part is less than 2 mm in diameter. Sources were mounted on a support made of polyethylene in order to minimize attenuation losses at lower energies. Measurements were performed with sources placed at a distance of 150 mm from the end-cap of the detector to also minimize effects on dead times as well as the coincidence summing in sources where this effect is present.

Results and discussion

Full-energy-peak efficiency calculations

Experimental FEP efficiencies along with their relative uncertainties were calculated by the following formulas:

$$\epsilon_{\text{exp.}}(E) = \frac{N(E)}{A \cdot p_{\gamma} \cdot t} \cdot C_i \quad (1)$$

$$C_i = C_{\text{dead time}} \cdot C_{\text{coincidence}} \cdot C_{\text{decay}} \cdot C_{\text{attenuation}} \quad (2)$$

$$U_{\epsilon} = \sqrt{(U_N)^2 + (U_A)^2 + (U_{p_{\gamma}})^2 + (U_t)^2} \quad (3)$$

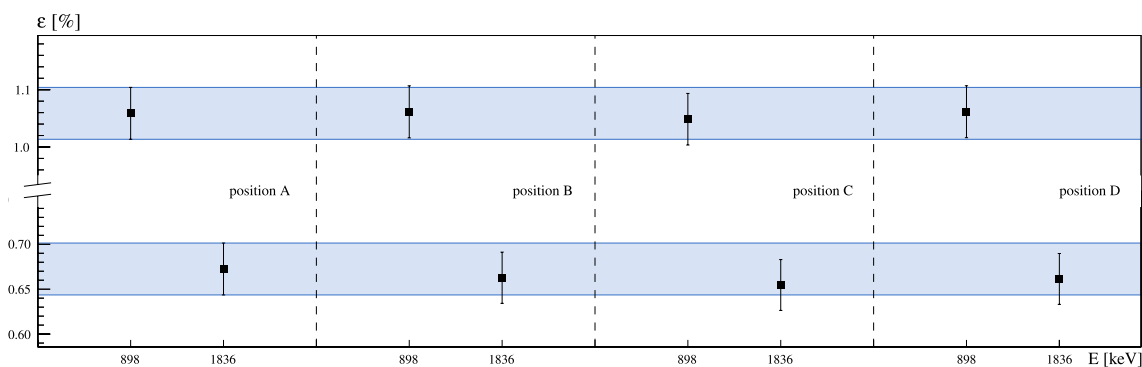


Fig. 4 Experimentally obtained FEP efficiency values for yttrium-88 measurement. Efficiencies from all four measured points show good agreements indicating that there is no displacement of the crystal or any possible type of irregularities in it

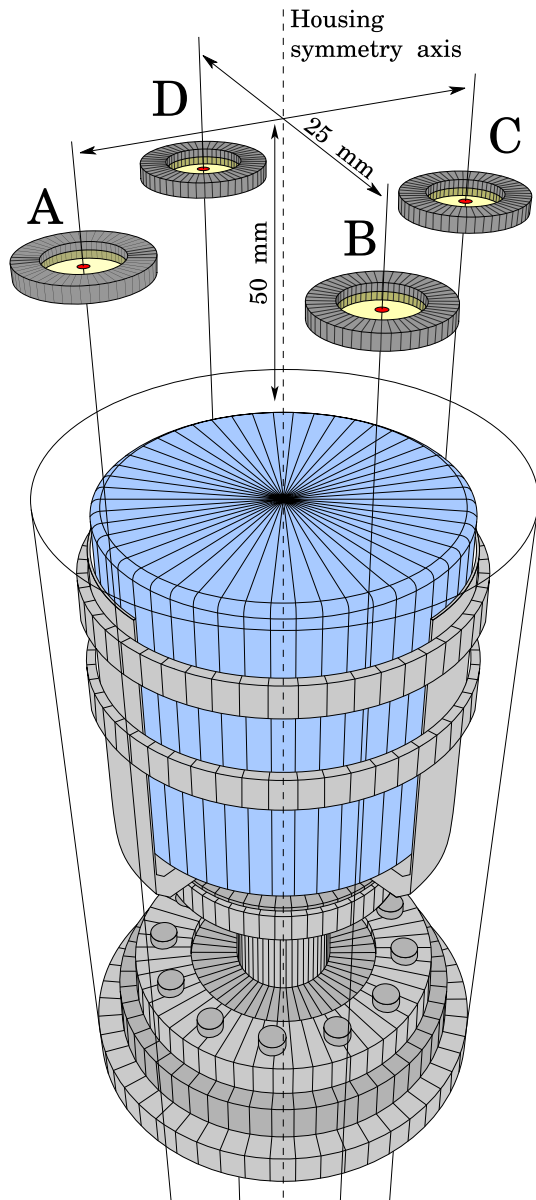


Fig. 5 Measuring geometry used for validation of crystals placement inside detectors housing using yttrium-88 source. Source was measured at 4 individual spatial points at 5 cm distance from the end-cap of the detector, with each point being displaced from the housing symmetry axis by 2.5 cm and covering full circle with a step of $\pi/4$ between the points

where $N(E)$ represents the number of net counts under a peak at energy of interest E , A is the activity of the source at the measurement start, p_γ is the emission probability of the studied peak, while t is the measurement live time. C_i are correction factors due to effects of dead time, decay correction factor for the activity decrease during measurement, coincidence summing correction factor for radionuclides

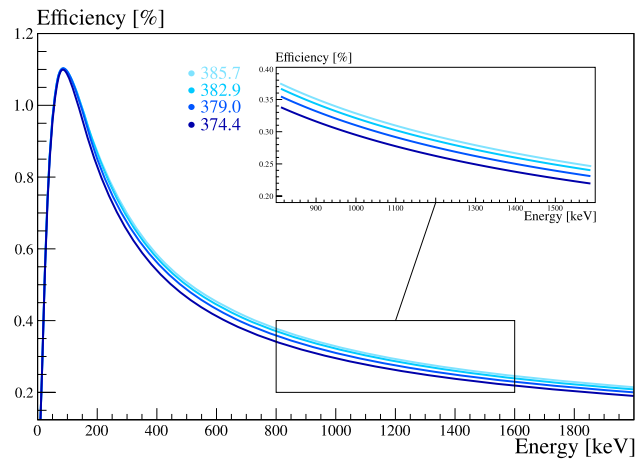


Fig. 6 Efficiency curves for four different set combinations of the crystals inner cavity radius and height

with complex decay-schemes and correction to the effect of self-attenuation. Dead-time was virtually corrected for during the measurement itself since the analyzer automatically corrects dead-time losses because the MCA works in the live-time regime. Thus, time used for efficiency calculations was the ADC live time. Also coincidence summing effect was negligible since the reference measuring geometry was as such that the sources were far enough from the end-cap of the detector to minimize this effect while the correction on activity decline during the measurement was also negligible since the measurement times were significantly shorter than the half-life periods of corresponding sources. Taking into account the construction of the sources used the correction factor due to self-attenuation was also excluded from the calculations. As such, main source of uncertainty was the uncertainty of sources activities. Values of photon energies, emission probabilities, half-lives and their uncertainties were all taken from the recommended data of National Nuclear Data Center (NNDC—Brookhaven National Laboratory [19]).

When it comes to simulation, the primary particles were generated as photons of discrete energies that were emitted in random direction in 4π sr spatial angle [20]. Simulated efficiencies were calculated as:

$$\epsilon_{\text{sim.}}(E) = \frac{N_{\text{det.}}}{N_{\text{total}}} \quad (4)$$

where $N_{\text{det.}}$ is the number of events that deposit their full energy in the defined scoring volume while N_{total} is the total number of simulated events for a given energy E . Number of photons generated in each run was as such that the relative uncertainty of the simulated FEP efficiencies at given energies was below 1%.

Table 4 Simulated FEP efficiencies covering all 14 different combinations of inner cavities radius and height along with average relative deviation (RSD) in respect to experimental data

E (keV)	ϵ_{exp} (%)	Crystals active volume (cc)													
		Simulated FEP efficiencies (%)													
		386.2	385.7	385.1	384.4	383.7	382.9	382.1	381.1	380.1	379.0	377.9	376.6	375.3	374.4
662	0.369	0.421	0.423	0.418	0.419	0.413	0.411	0.408	0.405	0.401	0.399	0.392	0.390	0.383	0.382
779	0.324	0.384	0.381	0.380	0.377	0.376	0.373	0.369	0.367	0.364	0.359	0.356	0.350	0.346	0.344
835	0.312	0.368	0.368	0.364	0.364	0.360	0.358	0.355	0.351	0.348	0.347	0.340	0.338	0.332	0.327
898	0.292	0.355	0.351	0.351	0.347	0.347	0.345	0.342	0.339	0.336	0.329	0.328	0.322	0.319	0.315
964	0.289	0.334	0.334	0.331	0.331	0.327	0.325	0.323	0.319	0.316	0.314	0.309	0.306	0.301	0.300
1173	0.242	0.298	0.299	0.294	0.295	0.291	0.288	0.286	0.283	0.280	0.279	0.273	0.272	0.267	0.265
1332	0.224	0.277	0.274	0.274	0.271	0.269	0.268	0.265	0.263	0.260	0.256	0.254	0.249	0.248	0.244
1836	0.186	0.223	0.222	0.220	0.219	0.217	0.215	0.213	0.211	0.208	0.206	0.203	0.200	0.198	0.194
Avg. RSD (%)		18.20	17.64	17.23	16.56	16.01	15.30	14.49	13.61	12.57	11.26	10.09	8.84	7.42	6.74

Efficiency curves corresponding to highlighted crystals active volumes of 385.7, 382.9, 379.0 and 374.4 cc are illustrated in Fig. 6

Creating the MC model

Due to geometry of the sources and the distance at which they were measured, in simulation one could approximate them as ideal point-sources. However, for the purpose of completeness of the simulation sources were defined as thin discs of 50 μm thickness with diameter of 2 mm. Therefore, the events in the simulation were generated randomly in spatial points confined by volume defined in this manner.

Initially, before creating a model, quick measurement was carried out in order to check if there was any possible displacement of the crystal from the axis of the housing as well as if the inactive layers surrounding the crystal, including the Ge dead layer, were homogeneously distributed. This revolved around measuring yttrium-88 source at four different spatial points. The idea was to check if there were any significant changes in efficiencies between these four measuring points since it could indicate on irregularities one would need to further investigate. However, all four measured points showed good agreements between one another, with maximum deviation being less than 1.2%. Efficiencies of this measurement are given in Fig. 4, while the setup used is illustrated in Fig. 5.

One of the biggest obstacles we have encountered while modelling the detector was quantifying the inner contact cavity of the crystal as its dimensions were not specified by the manufacturer (refer to Table 2). This property of the crystal is important as any kind of modification essentially impacts its active volume. As such it influences the FEP efficiency values in mid and high-end energy region the most. For lower energies it doesn't play a significant role since low-energy photons don't have the ability to penetrate high-density material such as germanium more than only few millimetres in depth. In order to characterize this property of the crystal, a simulation of 14 different combinations of cavities length (starting at 40 mm with 2.5 mm step) and radius (starting at 5 mm with 0.25 mm step) were carried out.

During this an approximation for crystals active volume based on crystals dimensions was taken into account. It was our understanding that the active volume of such a crystal could be in the range of 380 cc \pm 1%. Side dead layer was chosen to be 1 mm in addition to its further tuning. Since low-energy photons are not as important in this adjustment as previously mentioned the top dead layer was excluded for the time being. While choosing optimum values of radius and height we opted out to stay within \sim 10% deviation from the experimental data. Further accuracy would later on be achieved with additional dead layer tuning.

For our model, the optimum values for radius and height of the cavity were chosen to be 7.5 mm and 65 mm (corresponding to crystals active volume of 377.9 cc), respectively. Figure 6 displays efficiencies covering full energy range for a set of four different radius-height combinations, while Table 4 lists efficiencies covering all 14 runs (lower energies are excluded from the table as they are not impacted by these crystal parameters which can be seen from Fig. 6). Here, it is worth noting that radiography scans would be very beneficial, but that aside them there are other experimental approaches (e.g. with the use of collimators) that could provide a more insightful information on the matter [14].

Dead layers tuning

Lateral dead layer

HPGe crystals typically have dead layers on their surface that do not contribute to detection events. Their thickness can change over time and thus their estimation needs to be made in order to appropriately model it in the simulation (refer to "Optimization procedure" section). Since precise thicknesses and compositions of all layers surrounding the detector can significantly vary from the nominal values, the thicknesses of the dead layers were used for correction of these unknown parameters. The dead layers in the simulation

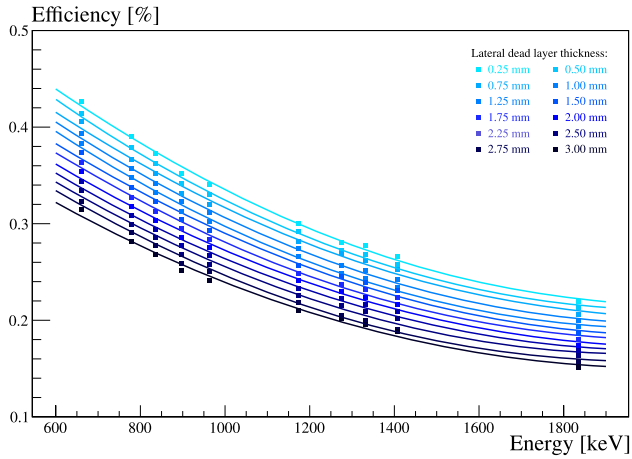


Fig. 7 Efficiencies covering energy range of 662–1836 keV for different values of the lateral dead layer thickness

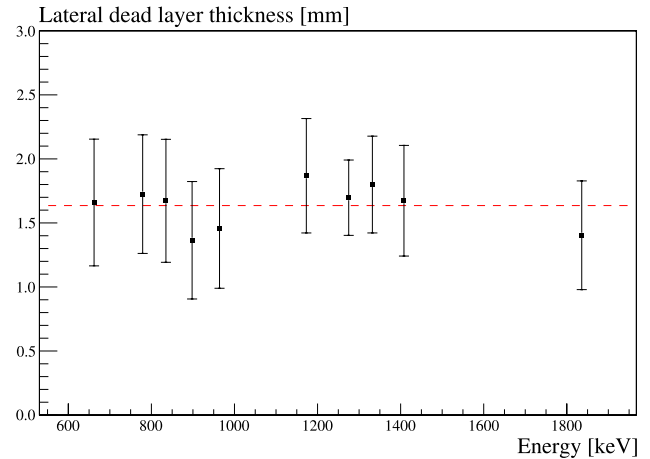


Fig. 10 Thickness of lateral dead layer obtained from linear interpolation covering the energy range of 662–1836 keV

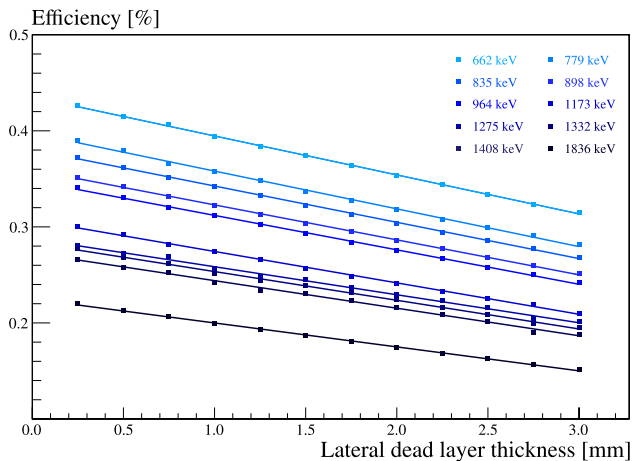


Fig. 8 Dependency of FEP efficiency at a given photon energy in relation to the thickness of the lateral dead layer

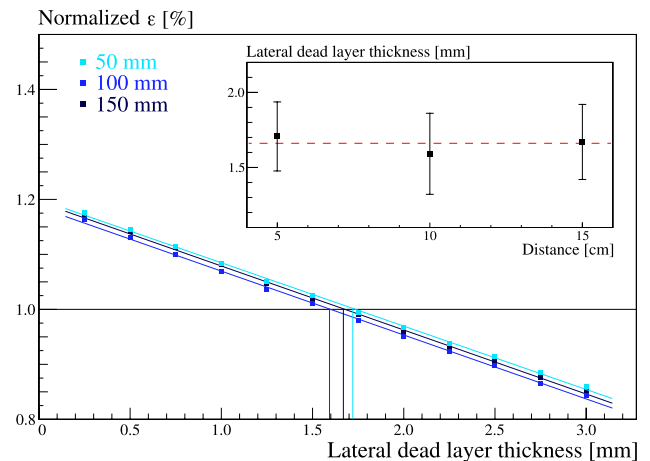


Fig. 11 Interpolation of normalized efficiency at 662 keV line from ^{137}Cs measured at three distances from the detector

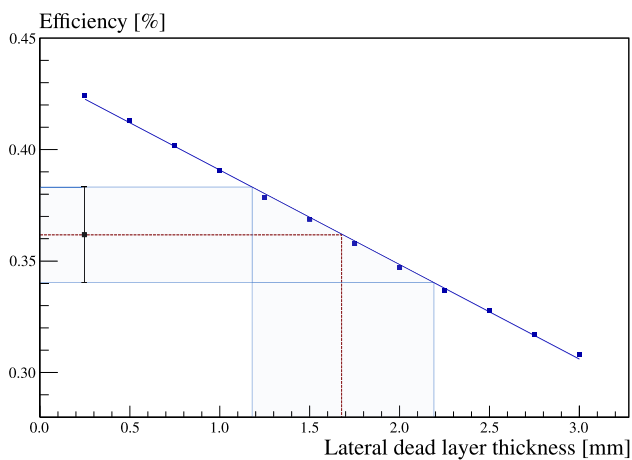


Fig. 9 An example of experimental efficiency interpolation on the linear fit obtained from simulated FEP efficiencies

were considered as completely inactive layers with no charge collection and were split into two parts: lateral (side) and top dead layer. Each part was individually optimized, since different thicknesses were expected (due to detectors entry window, top layer was expected to be thinner).

First adjustments were made for the lateral dead layer. For this, the efficiencies in the energy range of 662–1836 keV for measuring configuration of sources at a distance of 150 mm were used. With photon energies high enough the attenuation effects within the absorbing layers between the source and the active volume of the crystal are negligible. Therefore, since top dead layer doesn't play a significant role at these energies it was excluded for the time being. Simulated efficiencies in this energy region for different values of lateral dead layer thickness are illustrated in Fig. 7. Figure 8 shows the decrease of FEP efficiency at a given

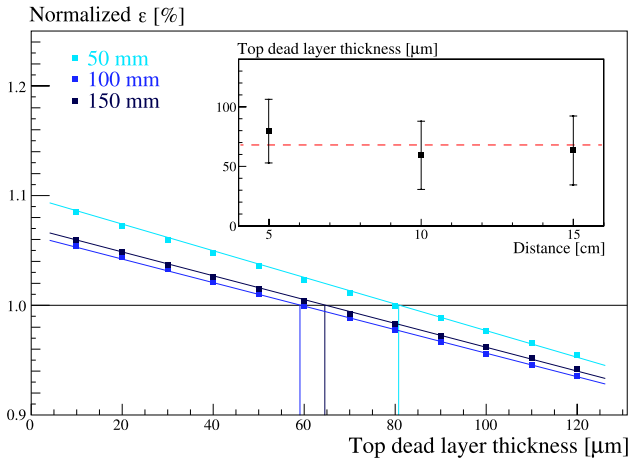


Fig. 12 Interpolation of normalized efficiency at 59 keV line from ²⁴¹Am measured at three distances from the detector

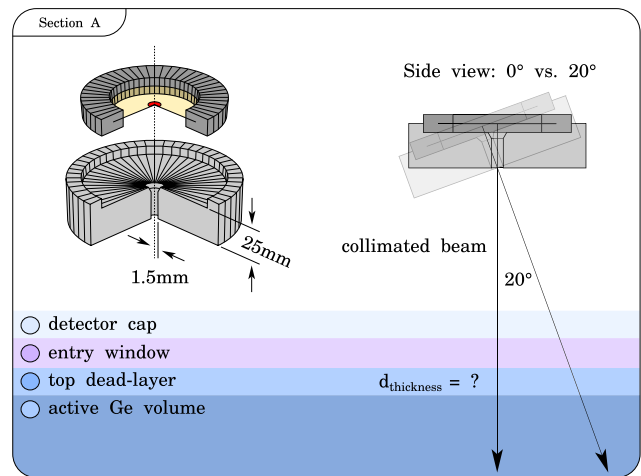
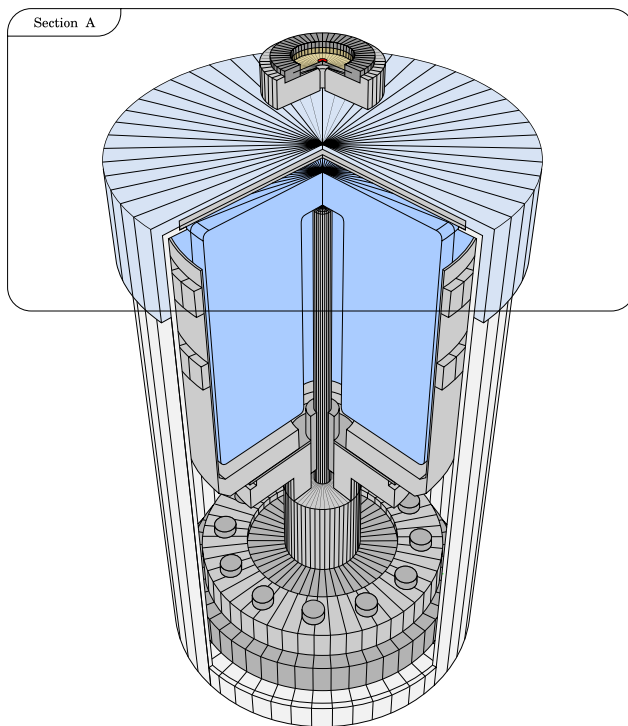
photon energy for different values of dead layer thicknesses. Clearly there is good linearity between the simulated efficiencies and the thicknesses of the lateral dead layer. These values were thus fitted using linear function with the value of adjusted R-squared of greater than 0.995 for all investigated photon energies.

The thickness of the lateral dead layer for a given photon energy was then interpolated based on these linear functions using the experimental FEP efficiency value as a reference

point. Example of this interpolation for energy of 662 keV in the case of ¹³⁷Cs is illustrated in Fig. 9. Interpolated values corresponding to different photon energies with an average thickness of 1.62 mm are shown in Fig. 10. In order to corroborate this value another measurement was carried out using ¹³⁷Cs source measured at three different distances from the end-cap of the detector (50 mm, 100 mm and 150 mm). Value of lateral dead layer thickness was then obtained with previously described interpolation on the linear fits (Fig. 11). Average thickness from this measurement was obtained to be 1.66 mm which is in good agreement with previously obtained value.

Top dead layer

Similar approach was adopted for the adjustment of top dead layer. Figure 12 shows efficiency dependance on the thickness of the top dead layer for 59 keV photons from ²⁴¹Am source measured at three different distances from the end-cap of the detector (50 mm, 100 mm and 150 mm). Average thickness of the top dead layer obtained in this way was 67.4 μm. In contrast to lateral, the top dead layer is significantly thinner which was expected due to the detectors entry window. However, in order to experimentally corroborate this another measurement using collimator made out of brass and again ²⁴¹Am source was performed (setup illustrated in Fig. 13). In total two measurements were carried out. In the



Mass attenuation coefficients

	μ_m [cm ² /g]
○ air (atmosphere)	0.188441
○ detector cap (polyethylene)	0.197523
○ detector entry window (cfrp)	0.175841
○ detector crystal (germanium)	2.083190

Fig. 13 Experimental setup using collimator and an ²⁴¹Am source for the estimation of the top dead layer. Table lists mass attenuation coefficients of different layers that photons traverse taken from NIST Standard Reference Database [21]

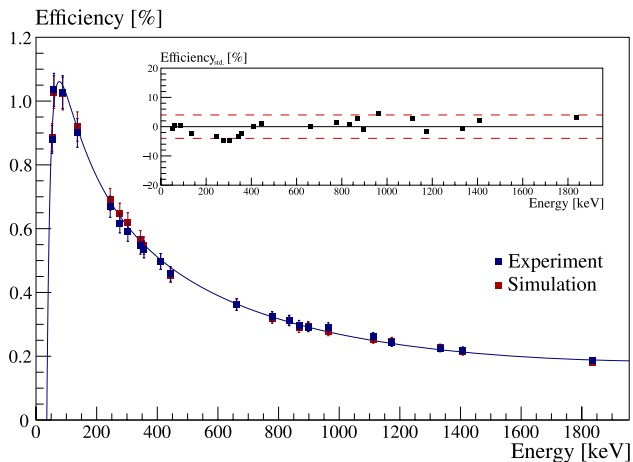


Fig. 14 Comparison of the experimental and simulated FEP efficiencies along with relative deviation between the two

first measurement the collimated beam from ^{241}Am source incident on the crystal was perpendicular in respect to crystals surface. In the second one the collimator was placed on a different mounting tilting the beam under a certain angle in respect to crystals axis (in our case the angle was 20°). This implies that photons have to traverse different lengths of layers in order to be detected. Both measurements were performed with source being at the same distance of 30 mm from the end-cap of the detector.

From photon intensity, given as:

$$I = I_0 e^{-\mu d} \quad (5)$$

where I is the photon intensity after they traverse the depth d of material with attenuation coefficient μ , while I_0 is the initial intensity, one can deduce the depth of the layers from the ratio of the two as:

$$\left. \begin{aligned} I_{20^\circ} &= I_0 e^{-\mu \frac{d}{\cos \alpha}} \\ I_{0^\circ} &= I_0 e^{-\mu d} \end{aligned} \right\} \mu d = \frac{\ln \frac{I_{20^\circ}}{I_{0^\circ}}}{1 - \frac{1}{\cos \alpha}} \quad (6)$$

where

$$d_{\text{Ge}} = \left(\frac{\ln \frac{I_{20^\circ}}{I_{0^\circ}}}{1 - \frac{1}{\cos \alpha}} - \sum_{i=1}^n d_i \mu_i \rho_i \right) / \mu_m(\text{Ge}) \rho_{\text{Ge}} \quad (7)$$

where the summation term represents each known layer that photons traverse before finally depositing their energy in the crystal and being detected.

Thickness of the top dead layer obtained using this approach was estimated to be $71.8 \mu\text{m}$ which is in good agreement with previously obtained simulated value. Comparison between the experimental FEP efficiencies and the

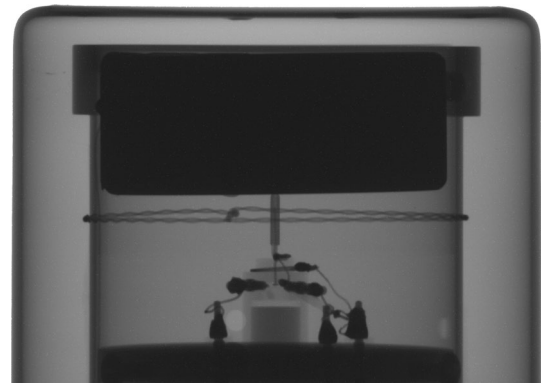


Fig. 15 Radiography scan of the LEGe detector (GL2020) showing the inner components of the detector in great detail

Table 5 Information from the manufacturer along with data obtained through radiography scan

Physical characteristics	Nominal	Scan
Crystal diameter	50	50.52
Crystal height	20	20.37
End-to-cap distance	5	5.0
Entry-window thickness	0.5	/
Cup end thickness	/	1.54
Cup outer diameter	/	77.35
Cup inner diameter	/	73.65
Top holder ring outer diameter	/	59.24
Crystal holder outer diameter	/	54.13
Crystal holder inner diameter	/	51.97
Crystal bulletization (average)	/	1.9
Cup rounded corner outer radius	/	4.09
Cup rounded corner inner radius	/	2.47

Values are given in mm

final simulation model covering full studied energy range (53–1836 keV) is given in Fig. 14.

LEGe detector optimization

Additionally, after performing the optimization on the XtRa detector, the code was also applied to a different detection equipment. This time around the optimization was not as detailed as it was primarily done only to check to a certain extent the validity of the code when applied to a different setup as well as to test the quickness of its implementation. For this purpose, our colleagues from Centre for Energy Research in Budapest have provided us with one of their detection devices. The detector in question is

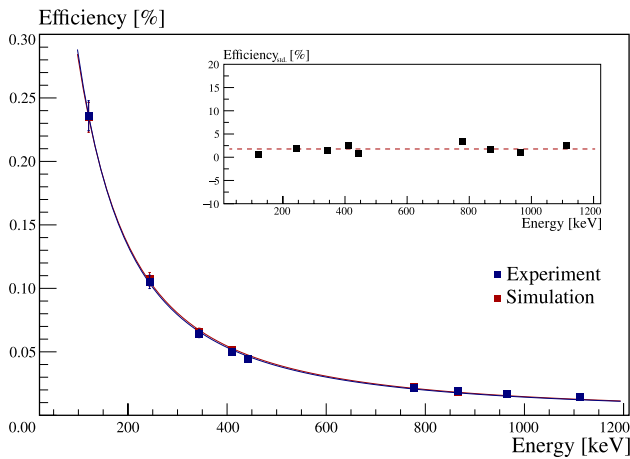


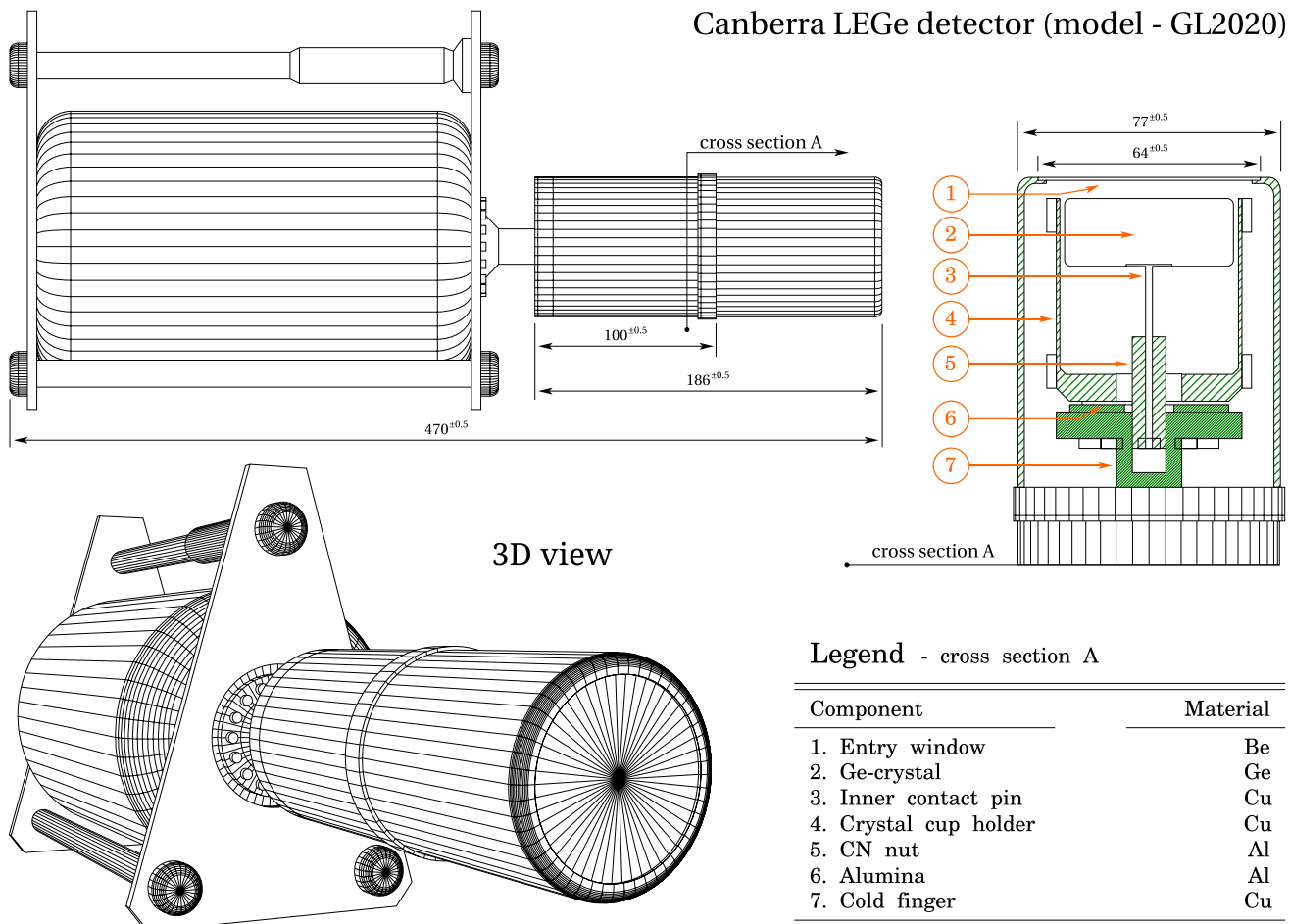
Fig. 16 Schematic diagram of the LEGe detector (Low Energy range Germanium, model GL2020, Canberra, Mirion Inc.) along with its 3D model and a listing of its inner components and materials

a Low Energy high-purity Germanium (LEGe) detector, model no. GL2020, manufactured by Canberra. This detector has a crystal of 20 mm thickness with an upper active

area of ~2000 mm² and an energy resolution of 400 eV and 680 eV at energies 5.9 keV and 122 keV, respectively. It is designed with thin front and side contacts, while the rear contact is significantly less in surface than crystals full lower area which provides lower detector capacitance. To further improve efficiency performance of the detector at low-energy part of the spectrum it is equipped with an entry window made of beryllium of 0.5 mm in thickness.

In contrast to GX10021 model, the GL2020 model came with a slightly more detailed documentation on its specifications. However, what makes this detector stand out in regards to the previously described one in terms of available information, is that it went under a radiography scan which provided a detailed imaging of its inner structure. This represented a significant source of information on its construction which greatly facilitated the process of creating its MC model. Image obtained through this scan, displayed in Fig. 15, allowed determining in greater detail the components of the detector as well as their dimensions, some of which are the thickness of the aluminium housing, position and outer dimensions of the crystal, crystals bulletization, crystal-to-window distance, etc. Detailed listing of the

Canberra LEGe detector (model - GL2020)



Legend - cross section A

Component	Material
1. Entry window	Be
2. Ge-crystal	Ge
3. Inner contact pin	Cu
4. Crystal cup holder	Cu
5. CN nut	Al
6. Alumina	Al
7. Cold finger	Cu

Fig. 17 Comparison of the experimental and simulated FEP efficiencies along with relative deviation between the two

dimensions of different detector components are given in Table 5. Technical drawing of GL2020 detector along with its 3D model is illustrated in Fig. 16.

Experimental calibration of detection equipment was carried out using a point-like standard gamma calibration ^{152}Eu source measured at 25 cm distance from the end-cap of the detector and thus covering energy range of 121–1112 keV. As before, the source is hot sealed between two polyimide foils with active area of around 2 mm in diameter. Because of the more detailed information on the equipment thanks to radiography imaging the MC modelling was significantly faster as there was no need to check for additional things (e.g. possible crystal displacement, “Dead layers tuning” section). Optimized model of the GL2020 detector showed good agreement with the experimental data that falls under an average relative deviation of ~1.8% for the studied energy range (Fig. 17). This can also further be improved upon by expanding the studied energy range using additional calibration sources, but it only shows that the more detailed documentation and information on the equipment plays a significant role in the process of optimizing detection equipment through Monte Carlo simulations.

Conclusion

Here presented study describes in detail a procedure for optimization of a coaxial p-type HPGe detector. Four detector parameters including the radius and height of the inner crystals cavity as well as the thickness of the lateral and top dead layers were tuned with the goal of achieving better results. Dead layers were adjusted based on the interpolation of the experimental efficiencies into the linear functions, which were determined by the fitting of the simulated efficiencies. For detector model GX10021 simulated FEP efficiencies obtained using the optimized model showed good agreement with the experimental data for a given measuring configuration. An average relative deviation of ~2% between the two for energy range of 53–1836 keV was achieved. Additionally, the code was applied on a different detection equipment (detector model GL2020) where an average relative deviation of ~1.8% was achieved for energy range of 121–1112 keV.

Acknowledgements Presented work was supported by the Ministry of Education, Science and Technological Development of the Republic of Serbia through Grants for PhD students (PhD grant OI 171002), IAEA Coordinated Research Project RC 23159. The authors would also like to thank Gamma Spectrometry team (Nuclear Security Department) and Radiography team (Nuclear Analysis and Radiography Department) from the Centre for Energy Research, Budapest, Hungary, for the data about LEGe detector.

References

- Conti CC, Salinas ICP, Zylberberg H (2013) A detailed procedure to simulate an HPGe detector with MCNP5. *Prog Nucl Energy* 66:35–40
- Jeřkovský M, Javorník A, Breier R, Slučiak J, Povinec PP (2019) Experimental and Monte Carlo determination of HPGe detector efficiency. *J Radioanal Nucl Chem* 322:1863–1869
- Saraiva A, Oliveira C, Reis M, Portugal L, Paiva I, Cruz C (2016) Study of the response of an ORTEC GMX45 HPGe detector via multi-radionuclide volume source using Monte Carlo simulations. *Appl Radiat Isot* 113:47–52
- Monte Carlo N-Particle code (MCNP) <https://mcnp.lanl.gov/>
- Geant4 <https://geant4.web.cern.ch/>
- LabSOCS <https://www.mirion.com/products/labsoocs-calibration-software>
- ANGLE <https://www.angle.me/>
- Vidmar T (2005) EFFTRAN-A Monte Carlo efficiency transfer code for gamma-ray spectrometry. *Nucl Instrum Methods Phys Res Sect A* 550:603–608
- Hurtado S, García-León R, García-Tenorio R (2004) GEANT4 code for simulation of a germanium gamma-ray detector and its application to efficiency calibration. *Nucl Inst Methods Phys Res A* 518:764–774
- FLUKA <http://www.fluka.org/fluka.php>
- PENELOPE <http://pypenelope.sourceforge.net/index.html>
- Trang LTN, Chuong HD, Thanh TT (2020) Optimization of p-type HPGe detector model using Monte Carlo simulation. *J Radioanal Nucl Chem* 327:287–297
- Khan W, Zhang Q, He C, Saleh M (2018) Monte Carlo simulation of the full energy peak efficiency of an HPGe detector. *Appl Radiat Isot* 131:67–70
- Khedr HI, Abdelati M, El Kourghly KM (2019) Investigation of a HPGe detector's geometry using X-Ray computed tomography in collaboration with Monte Carlo method. *Int J Eng Appl Sci* 6:42–46
- Joel GSC, Maurice NM, Jilbert NME, Ousmanou M, David S (2018) Monte Carlo method for gamma spectrometry based on GEANT4 toolkit: efficiency calibration of BE6530 detector. *J Environ Radioact* 189:109–119
- Elanique A, Marzocchi O, Leone D, Hegenbart L, Breustedt B, Oufni L (2012) Dead layer thickness characterization of the HPGe detector by measurements and Monte Carlo simulations. *Appl Radiat Isot* 70:538–542
- Tsang RHM, Pieke A, Auty DJ, Cleveland B, Delaquais S, Diederidze T, MacLellan R, Meng Y, Nusair O, Told T (2019) GEANT4 models of HPGe detectors for radioassay. *Nucl Instrum Methods Phys Res Sect A* 935:75–82
- Genie2KTM <https://www.mirion.com/products/genie-2000-basic-spectroscopy-software>
- NNDC - Brookhaven National Laboratory <https://www.nndc.bnl.gov/>
- Nikolić JD, Joković D, Todorović D, Rajačić M (2014) Application of GEANT4 simulation on calibration of HPGe detectors for cylindrical environmental samples. *J Radiol Prot* 34:47–55
- NIST—Standard Reference Database. <https://physics.nist.gov/PhysRefData/XrayMassCoeff/tab3.html>

Publisher's Note Springer Nature remains neutral with regard to jurisdictional claims in published maps and institutional affiliations.

Springer Nature or its licensor (e.g. a society or other partner) holds exclusive rights to this article under a publishing agreement with the author(s) or other rightsholder(s); author self-archiving of the accepted manuscript version of this article is solely governed by the terms of such publishing agreement and applicable law.



Detailed optimization procedure of an HPGe detector using Geant4 toolkit

M. Travar¹ · J. Nikolov¹ · N. Todorović¹ · A. Vraničar¹ · P. Völgyesi² · P. Kirchknopf² · I. Čeliković³ · T. Milanović³ · D. Joković⁴

Received: 26 November 2022 / Accepted: 27 January 2023 / Published online: 5 March 2023
© Akadémiai Kiadó, Budapest, Hungary 2023

Abstract

Presented study describes the optimization method of an HPGe detector through implementation of Geant4 toolkit. The optimized model was verified through comparison with experimentally obtained data using a set of point-like radioactive calibration sources. Acquired results displayed good agreement with the experimental data that falls under an average relative deviation of the order of ~2% within the energy range of 53–1836 keV. Additionally, in order to test the validity of the code it was also applied to a different detection equipment where an average relative deviation of the order of ~1.8% was achieved within the energy range of 121–1112 keV.

Keywords HPGe detector · γ -Spectrometry · FEP efficiency · Geant4 model · Monte Carlo simulation

Introduction

Over the years, High Purity Germanium (HPGe) detectors proved to be an excellent practical tool and as such have established their today's wide use in low background γ -spectrometry. One of the more significant advantages of γ -spectrometry is its easy sample preparation as chemical processing and separation of the studied subject is not always required. Therefore, with a single measurement, one can simultaneously perform both qualitative and quantitative analysis [1].

One of the most prominent features of HPGe detectors is their superior resolution. This feature virtually allows researchers to perform a thorough analysis by discriminating photons of similar energies in the studied spectra where otherwise they would superimpose within a single-energy

peak and as such would scathe analysis and produce wrongly assessed results. Naturally, this comes as of great importance when identification of radionuclides, as well as their activity concentrations, is being performed where high precision comes as a necessity [2].

Performance and reliability of HPGe systems depends, amongst other factors, on the quality of their calibration. In particular, performing radionuclide identification requires good energy calibration, while on the other hand to be able to obtain high-quality characterization of the activities one would require an accurate understanding and knowledge on the full-energy-peak (FEP) efficiency appropriate to specific conditions under which the measurement was carried out. This efficiency represents complex function that is characterized not only by detectors specifications but also by the aforementioned measuring conditions. Detailed information on the FEP efficiencies could be experimentally obtained using standard calibration sources. However, this carries certain difficulties. Namely, it is a question of availability of sources that have same or similar composition, as well as same or similar counting geometry as the studied sample. This may not always be physically or economically feasible, and can sometimes be difficult and time consuming. In turn, this led many of the research groups to turn towards the use of different software toolkits that implement Monte Carlo method. When applied along with γ -spectrometry Monte Carlo simulations provide means to determine the detectors

✉ J. Nikolov
jovana.nikolov@df.uns.ac.rs

¹ Faculty of Sciences, University of Novi Sad, Trg Dositeja Obradovića 3a, 21000 Novi Sad, Serbia

² Centre for Energy Research, Konkoly-Thege Miklós út. 29-33, Budapest, Hungary

³ Institute for Nuclear Sciences Vinča, Mike Petrovića Alasa 12-16, 11000 Belgrade, Serbia

⁴ Institute for Physics, University of Belgrade, Pregrevica 18, 11000 Belgrade, Serbia

response function for any new given measuring geometry or matrix without the need of additional standard calibration sources, optimizing in that way both time and financial resources. Thus, Monte Carlo approach comes as a reliable solution with little to no expense depending on the software of choice [3].

Monte Carlo simulations

Today there is a handful of Monte Carlo codes available to the scientific community, but the ones most commonly used for the purpose of detector optimization are MCNP (Monte Carlo N-Particle code, LoS Alamos National Laboratory [4]) and Geant4 (GEometry ANd Tracking4, CERN [5]). Besides the two, there are other commercially available codes that utilize and combine both absolute approach to FEP efficiency calculations by means of Monte Carlo simulations as well as relative approach by means of experimental comparison with well-known sources (LabSOCS [6], ANGLE [7], EFFTRAN [8], etc.). A detailed optimization procedure of a co-axial extended range (XtRa) HPGe detector based on application of Geant4 toolkit, with accent on the dependencies of FEP efficiency values on certain detector parameters, is presented within this work.

Geant4: a brief overview

Geant4, first introduced back in 1998, is an open-source software toolkit that can accurately simulate the passage of particles through matter. Design choice for this code was an object-oriented methodology and C++ language in order to provide the user with a modular and flexible software. Unlike its previous instalment Geant3, which was not able to simulate particles with energies below 10 keV, Geant4 can simulate electromagnetic processes down to 250 eV. This feature can greatly influence the accuracy when low-energy γ -spectrometry simulations are being performed [9].

Geant4 code includes facilities for handling geometry, tracking, run management, visualization, detector response and user interface (UI). Unlike other computational Monte Carlo codes such as MCNP [4], FLUKA [10], PENELOPE [11], etc., Geant4 is not an executable program but rather a set of C++ class libraries that users must implement on their own. In order to build a simulation code, one must describe through these classes the geometry of the setup (shapes and materials used, sensitive components), generation of primary particles as well as the production of relevant secondary particles (their type, energy, momentum, charge), physics processes, etc. Hence, a firm knowledge in object-oriented programming is required [9].

Utility of Geant4 reflects in its ability to trace the history of each individual particle which consists of its emission by the radioactive source, its interaction with the detector and

surrounding materials and the production and transport of secondary particles. As such, the code can directly determine energy deposition in the simulated scoring volume of the detector, allowing one to perform FEP efficiency calculations. Since no approximations are needed there are no limitations to sample-detector configurations. However, the accuracy of the simulated efficiencies is largely affected by incomplete parameters of the detector. Generic characterization provided by the manufacturer is usually insufficient, since some of the parameters are unknown or sometimes not even related to the specific detector but are instead rather averaged over a set of the detectors of the same or similar type. Consequently, many studies reported large deviations between the simulated and experimentally obtained FEP efficiencies when nominal values provided by manufacturer were used (well over 10–20%). This in turn demands the optimization of the detector model to be carried out in order to achieve better agreements. Beside this, one of the main disadvantages of the code in the past was its time scale for generating sufficient number of events in order to achieve good statistical uncertainties of the order of 1% or less. This issue is complemented with today's available hardware where significant improvements have been made in terms of computational times thanks to significant increase in the computational power due to use of parallel computing, computer clusters, supercomputers, etc.

Version of Geant4 used for optimization procedure presented in this work was 4.10.0.7. To significantly reduce computational times the simulation code was written in multithreading mode. Based on data provided by the manufacturer (Table 2) initial model of the detector was made using a variety of geometry classes that Geant4 provides. Parameters supplied by the manufacturer were taken as constant while other parameters were taken as free that would undergo further adjustments.

Geant4 also provides a variety of classes that describe physics processes. Low-energy electromagnetic package valid down to energy of 250 eV was used in this study (G4EmLivermorePhysics). This package facilitates processes necessary for performing low energy γ -ray spectrometry, some of which are: Compton and Rayleigh scattering, photo-electric effect, pair production, fluorescence and Auger effect, bremsstrahlung and ionization, etc.

Materials and methods

Optimization procedure

The most notable detector parameters that can significantly influence FEP efficiency calculations, and which are not always provided, are the so-called dead layers. These layers are formed by diffusion of contact material (usually

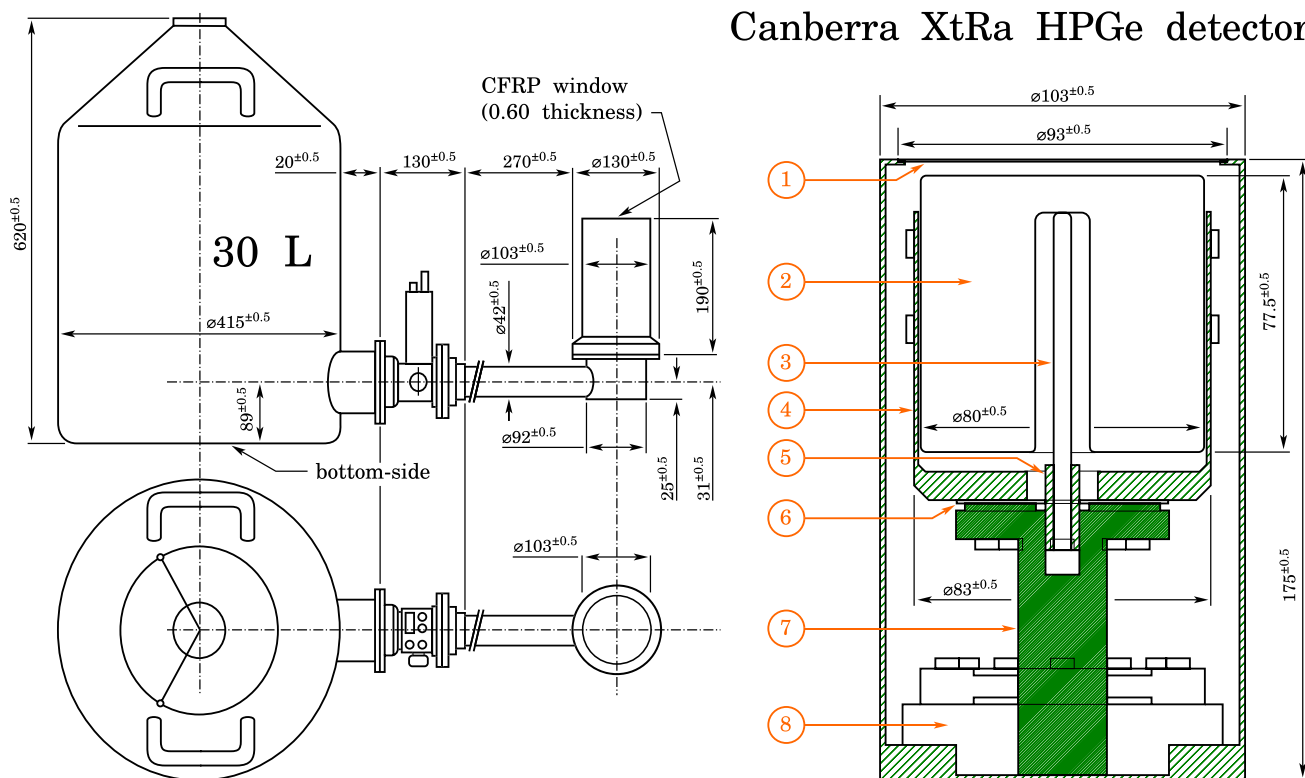


Fig. 1 Schematic diagram of the HPGe detector (XtRa—extended range, model no. GX10021, Canberra, Mirion Inc.) and its cooling system (U-type of cryostat configuration, model no. 7915-30-ULB, Canberra, Mirion Inc.). Values given in mm

Table 1 Components and materials (refer to Fig. 1)

Components	Material
Entry-window	cfrp*
Ge-crystal	Ge
Inner contact pin	Cu
Crystal cup holder	Cu
CN nut	Al
Alumina	Al
Cold finger	Cu
Lead shielding	Pb

*Carbon-fiber-reinforced polymer (1.42 g/cm³ density)

lithium) into the germanium crystal. However, they cannot simply be quantified as the depth of Li-diffused atoms. They are described as layers consisting of actual dead layer (with no charge collection) and partially active or effective dead layer (with low charge collection efficiency). Thickness of these layers depends on the impurity level of germanium crystal as well as the electrode production process. Dead layers virtually act as absorbing layers, shielding the crystal and effectively decreasing its active volume. Over time, they increase as a consequence of

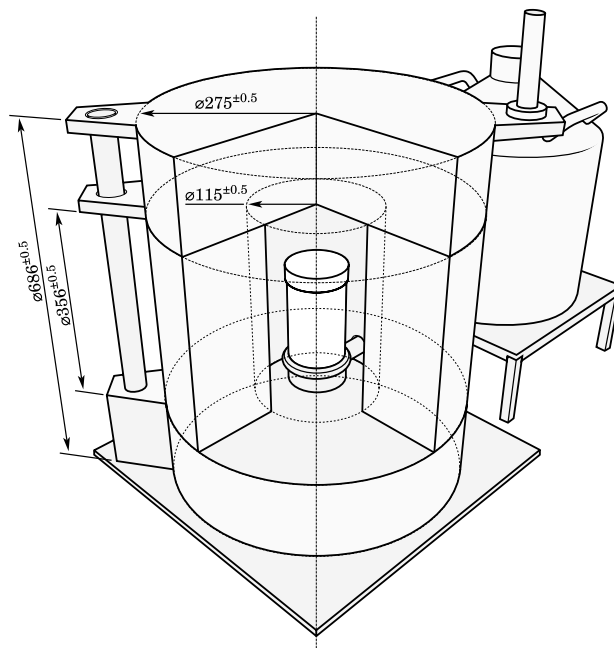


Fig. 2 3D model of the detector with its cooling system and commercial passive shielding in which it is installed

continuous diffusion of Li-atoms, making it important to be precisely quantified especially when working with older equipment. For p-type HPGe detectors these layers play a significant role and have to be properly taken into account. In contrast, for n-type detectors also known as Reverse Electrode Ge-detectors (REGe), the outer dead layer is much thinner and doesn't represent a significant modification in the simulation model. Other than this, there is also the possibility of other parameters deviating from the values they were initially assigned by the manufacturer, some of which are the diameter or length of the crystal, crystal-to-window distance, inner crystals cavity dimensions, the rounding of the crystal (bulletization), thickness of the entry window, etc. Any change of these parameters can have an impact on the efficiency values. Thus, to improve on the accuracy an optimization procedure needs to be carried out [12].

Generally, there are two approaches one could adopt when optimizing a model. First one involves an accurate determination of the geometrical parameters using various techniques that include x/γ-ray radiography scans. With these, a detailed imaging of the inner structure of their equipment can be obtained and thus greatly facilitate optimization (refer to “LEGe detector optimization” section). Even though this approach can be extremely precise, its application is difficult for many laboratories as the required equipment for this may not always be available. Second approach involves an experimental calibration of a simple configuration after which one tries to adjust the parameters in the simulation in order to obtain better results. Many of the studies that performed the latter approach [1–3, 9, 12–17] report agreements that typically fall within an average uncertainty of 5% or less within the studied energy range. Main advantages of this approach is its simplicity and quick implementation. However, it brings certain downsides as well. Namely, there is no guarantee that the optimized model actually matches the one in reality as there is no reference to take from and since efficiencies depend on more than one factor, it is also possible that multiple configurations yield satisfactory results for a given setup. With this in mind, the optimized model for one counting geometry would not necessarily be reliable for a different one. Therefore, it is advised to perform the optimization for each new counting configuration.

Experimental setup

In this study a low-background γ-spectrometer with coaxial p-type HPGe detector (XtRa, model no. GX10021, Canberra, Mirion Inc.) was used. Figure 1 illustrates technical drawing of the detector with its components listed in Table 1. A 3D model of the equipment along with its commercial

Table 2 Information on the detectors specification and performance data provided by the manufacturer

<i>Specifications</i>	
Detector model	GX10021
Cryostat model	7915-30-ULB
Preamplifier model	2002C
<i>Physical characteristics</i>	
Crystal diameter	80 mm
Crystal height	77.5 mm
End-to-cap distance	5 mm
Active volume	0.6 mm
Inner cavity height	/
Inner cavity diameter	/
Top dead layer	/
Inner dead layer (p + contact)	/
Lateral dead layer (n + contact)	/
<i>Electrical characteristics</i>	
Depletion voltage	3000 Vdc
Recommended bias voltage Vdc	(+) 3500 Vdc

Table 3 Point-like radioactive source along with their activities and respective uncertainties (Ritverc co.)

Source	Activity (kBq)	Uncertainty (%)
Mn-54	57.23	3
Co-57	45.52	3
Co-60	74.55	3
Y-88	1.781	3
Cd-109	57.03	3
Ba-133	83.33	3
Eu-152	88.48	3
Am-241	40.84	3

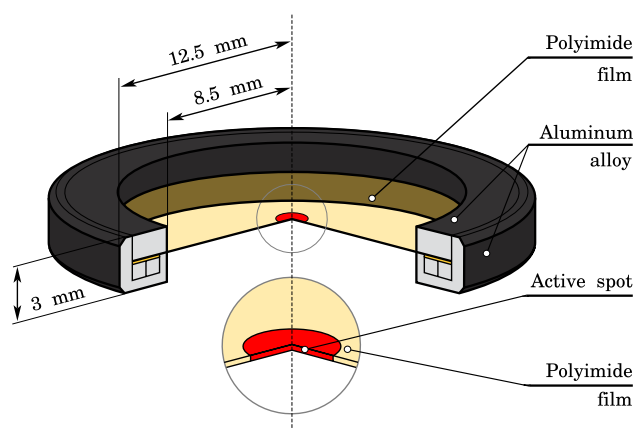


Fig. 3 Ritverc co. point-like standard gamma calibration sources

shielding and cooling system is illustrated in Fig. 2. Table 2 lists detectors nominal values provided by the manufacturer.

This detector has a relative efficiency of 100% and an energy resolution of 1.20 keV and 2.1 keV at energies 122 keV and 1332 keV, respectively. Most conventional p-type co-axial detectors come with a lithium diffused contact of typically 0.5–1.5 mm thickness which is more than enough to stop most of the photons below 40 keV energies. However, the entry window present with XtRa offers all the advantages of standard co-axial detector, as well as the energy response in low-energy region of the more expensive REGe detectors. In our case the entry window is made of highly durable carbon composition in the form of carbon epoxy, which allows the transmission of more than 85% for photons of energies above 15 keV and nearly 100% for those of energies above 20 keV.

The detector is installed within commercial passive shielding in order to achieve low background needed in environmental applications (Canberra, Mirion Inc., model type 777B). This shielding consists of (from inside to outside) a thin layer of copper and tin, followed by lead layer of 150 mm thickness and a layer of low-carbon steel of 10 mm thickness. Thin layers of copper and tin play a role of passive shielding of x-rays produced by transitions on K-shell of lead (75–85 keV energy region). The presence of x-rays in tin in the energy region of 25–28 keV is reduced by the presence of copper layer. Lead layer is made of 125 mm outer layer which contains standard low-radioactive lead while the inner layer of 25 mm thickness contains ^{210}Pb with activities less than 20 Bq/kg. As such, this type of passive shielding offers significant reduction of surrounding background (mainly from ^{40}K and ^{208}Tl) as well as reduction to the contribution of the annihilation line at 511 keV.

Acquisition of gamma spectra was driven by Genie2KTM software [18]. All of spectra were recorded in mode of 16,384 channels with the energy width per channel of

178.4 eV and with the upper energy threshold set to detect photons of energies up to 3 MeV. Acquisition time for each measured spectrum was adjusted as such to keep the statistical uncertainty of the interested peak area below 1% with dead-times for all measurements standing less than 4%.

Experimental calibration of the equipment was carried out using a set of point-like standard gamma calibration radioactive sources (Table 3, Fig. 3). These sources are hot sealed between two polyimide foils of total thickness of $100 \pm 10 \mu\text{m}$ placed in aluminium capsule in the form of a ring of 3 mm thickness and 25 mm diameter. The active part is less than 2 mm in diameter. Sources were mounted on a support made of polyethylene in order to minimize attenuation losses at lower energies. Measurements were performed with sources placed at a distance of 150 mm from the end-cap of the detector to also minimize effects on dead times as well as the coincidence summing in sources where this effect is present.

Results and discussion

Full-energy-peak efficiency calculations

Experimental FEP efficiencies along with their relative uncertainties were calculated by the following formulas:

$$\epsilon_{\text{exp.}}(E) = \frac{N(E)}{A \cdot p_{\gamma} \cdot t} \cdot C_i \quad (1)$$

$$C_i = C_{\text{dead time}} \cdot C_{\text{coincidence}} \cdot C_{\text{decay}} \cdot C_{\text{attenuation}} \quad (2)$$

$$U_{\epsilon} = \sqrt{(U_N)^2 + (U_A)^2 + (U_{p_{\gamma}})^2 + (U_t)^2} \quad (3)$$

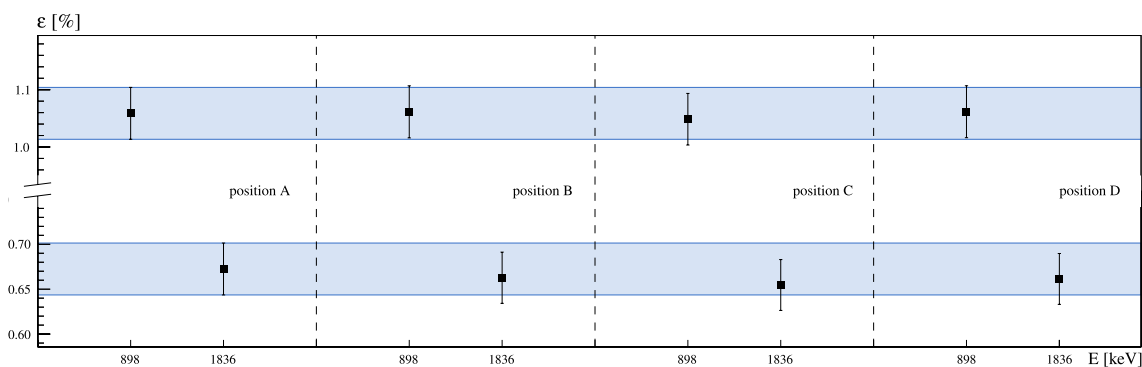


Fig. 4 Experimentally obtained FEP efficiency values for yttrium-88 measurement. Efficiencies from all four measured points show good agreements indicating that there is no displacement of the crystal or any possible type of irregularities in it

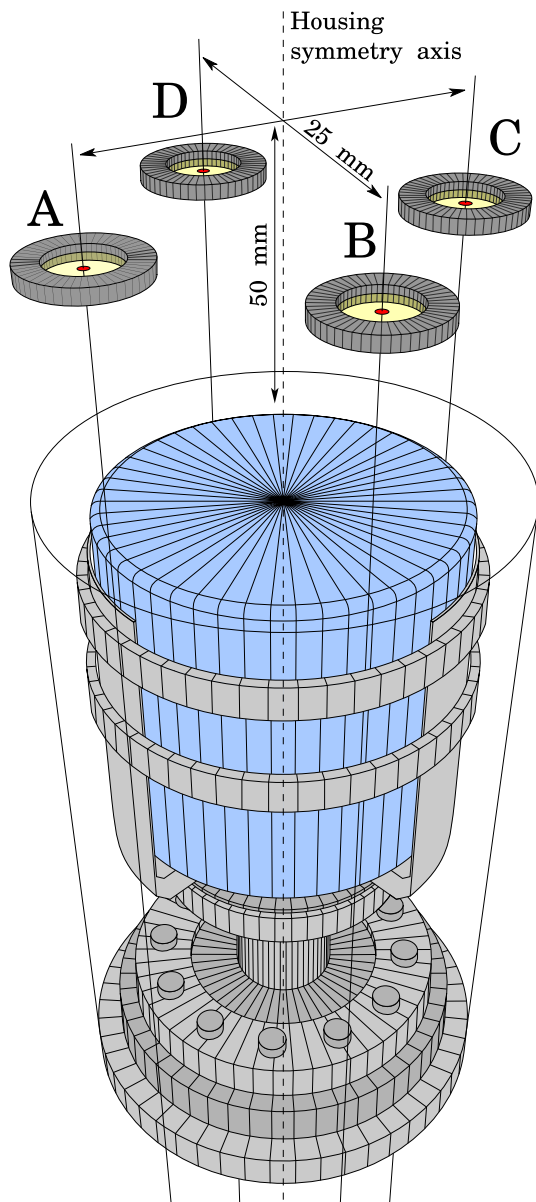


Fig. 5 Measuring geometry used for validation of crystals placement inside detectors housing using yttrium-88 source. Source was measured at 4 individual spatial points at 5 cm distance from the end-cap of the detector, with each point being displaced from the housing symmetry axis by 2.5 cm and covering full circle with a step of $\pi/4$ between the points

where $N(E)$ represents the number of net counts under a peak at energy of interest E , A is the activity of the source at the measurement start, p_γ is the emission probability of the studied peak, while t is the measurement live time. C_i are correction factors due to effects of dead time, decay correction factor for the activity decrease during measurement, coincidence summing correction factor for radionuclides

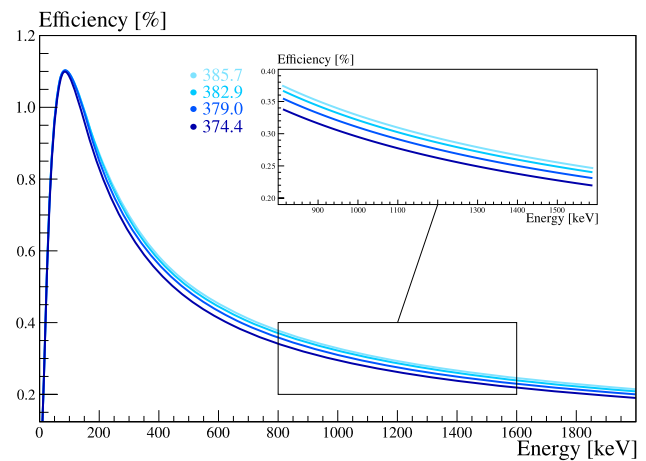


Fig. 6 Efficiency curves for four different set combinations of the crystals inner cavity radius and height

with complex decay-schemes and correction to the effect of self-attenuation. Dead-time was virtually corrected for during the measurement itself since the analyzer automatically corrects dead-time losses because the MCA works in the live-time regime. Thus, time used for efficiency calculations was the ADC live time. Also coincidence summing effect was negligible since the reference measuring geometry was as such that the sources were far enough from the end-cap of the detector to minimize this effect while the correction on activity decline during the measurement was also negligible since the measurement times were significantly shorter than the half-life periods of corresponding sources. Taking into account the construction of the sources used the correction factor due to self-attenuation was also excluded from the calculations. As such, main source of uncertainty was the uncertainty of sources activities. Values of photon energies, emission probabilities, half-lives and their uncertainties were all taken from the recommended data of National Nuclear Data Center (NNDC—Brookhaven National Laboratory [19]).

When it comes to simulation, the primary particles were generated as photons of discrete energies that were emitted in random direction in 4π sr spatial angle [20]. Simulated efficiencies were calculated as:

$$\epsilon_{\text{sim.}}(E) = \frac{N_{\text{det.}}}{N_{\text{total}}} \quad (4)$$

where $N_{\text{det.}}$ is the number of events that deposit their full energy in the defined scoring volume while N_{total} is the total number of simulated events for a given energy E . Number of photons generated in each run was as such that the relative uncertainty of the simulated FEP efficiencies at given energies was below 1%.

Table 4 Simulated FEP efficiencies covering all 14 different combinations of inner cavities radius and height along with average relative deviation (RSD) in respect to experimental data

E (keV)	ϵ_{exp} (%)	Crystals active volume (cc)													
		Simulated FEP efficiencies (%)													
		386.2	385.7	385.1	384.4	383.7	382.9	382.1	381.1	380.1	379.0	377.9	376.6	375.3	374.4
662	0.369	0.421	0.423	0.418	0.419	0.413	0.411	0.408	0.405	0.401	0.399	0.392	0.390	0.383	0.382
779	0.324	0.384	0.381	0.380	0.377	0.376	0.373	0.369	0.367	0.364	0.359	0.356	0.350	0.346	0.344
835	0.312	0.368	0.368	0.364	0.364	0.360	0.358	0.355	0.351	0.348	0.347	0.340	0.338	0.332	0.327
898	0.292	0.355	0.351	0.351	0.347	0.347	0.345	0.342	0.339	0.336	0.329	0.328	0.322	0.319	0.315
964	0.289	0.334	0.334	0.331	0.331	0.327	0.325	0.323	0.319	0.316	0.314	0.309	0.306	0.301	0.300
1173	0.242	0.298	0.299	0.294	0.295	0.291	0.288	0.286	0.283	0.280	0.279	0.273	0.272	0.267	0.265
1332	0.224	0.277	0.274	0.274	0.271	0.269	0.268	0.265	0.263	0.260	0.256	0.254	0.249	0.248	0.244
1836	0.186	0.223	0.222	0.220	0.219	0.217	0.215	0.213	0.211	0.208	0.206	0.203	0.200	0.198	0.194
Avg. RSD (%)		18.20	17.64	17.23	16.56	16.01	15.30	14.49	13.61	12.57	11.26	10.09	8.84	7.42	6.74

Efficiency curves corresponding to highlighted crystals active volumes of 385.7, 382.9, 379.0 and 374.4 cc are illustrated in Fig. 6

Creating the MC model

Due to geometry of the sources and the distance at which they were measured, in simulation one could approximate them as ideal point-sources. However, for the purpose of completeness of the simulation sources were defined as thin discs of 50 μm thickness with diameter of 2 mm. Therefore, the events in the simulation were generated randomly in spatial points confined by volume defined in this manner.

Initially, before creating a model, quick measurement was carried out in order to check if there was any possible displacement of the crystal from the axis of the housing as well as if the inactive layers surrounding the crystal, including the Ge dead layer, were homogeneously distributed. This revolved around measuring yttrium-88 source at four different spatial points. The idea was to check if there were any significant changes in efficiencies between these four measuring points since it could indicate on irregularities one would need to further investigate. However, all four measured points showed good agreements between one another, with maximum deviation being less than 1.2%. Efficiencies of this measurement are given in Fig. 4, while the setup used is illustrated in Fig. 5.

One of the biggest obstacles we have encountered while modelling the detector was quantifying the inner contact cavity of the crystal as its dimensions were not specified by the manufacturer (refer to Table 2). This property of the crystal is important as any kind of modification essentially impacts its active volume. As such it influences the FEP efficiency values in mid and high-end energy region the most. For lower energies it doesn't play a significant role since low-energy photons don't have the ability to penetrate high-density material such as germanium more than only few millimetres in depth. In order to characterize this property of the crystal, a simulation of 14 different combinations of cavities length (starting at 40 mm with 2.5 mm step) and radius (starting at 5 mm with 0.25 mm step) were carried out.

During this an approximation for crystals active volume based on crystals dimensions was taken into account. It was our understanding that the active volume of such a crystal could be in the range of 380 cc \pm 1%. Side dead layer was chosen to be 1 mm in addition to its further tuning. Since low-energy photons are not as important in this adjustment as previously mentioned the top dead layer was excluded for the time being. While choosing optimum values of radius and height we opted out to stay within \sim 10% deviation from the experimental data. Further accuracy would later on be achieved with additional dead layer tuning.

For our model, the optimum values for radius and height of the cavity were chosen to be 7.5 mm and 65 mm (corresponding to crystals active volume of 377.9 cc), respectively. Figure 6 displays efficiencies covering full energy range for a set of four different radius-height combinations, while Table 4 lists efficiencies covering all 14 runs (lower energies are excluded from the table as they are not impacted by these crystal parameters which can be seen from Fig. 6). Here, it is worth noting that radiography scans would be very beneficial, but that aside them there are other experimental approaches (e.g. with the use of collimators) that could provide a more insightful information on the matter [14].

Dead layers tuning

Lateral dead layer

HPGe crystals typically have dead layers on their surface that do not contribute to detection events. Their thickness can change over time and thus their estimation needs to be made in order to appropriately model it in the simulation (refer to "Optimization procedure" section). Since precise thicknesses and compositions of all layers surrounding the detector can significantly vary from the nominal values, the thicknesses of the dead layers were used for correction of these unknown parameters. The dead layers in the simulation

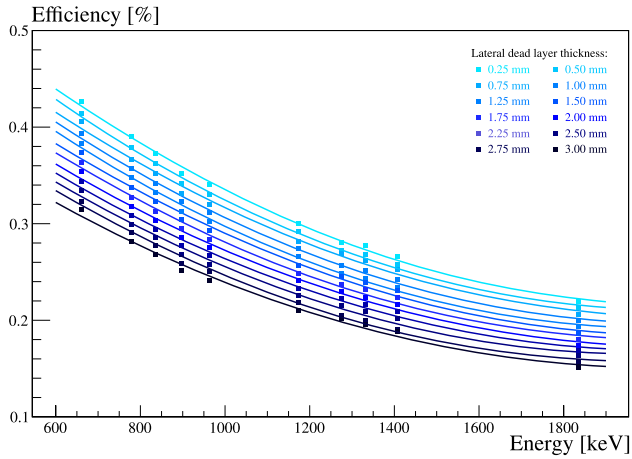


Fig. 7 Efficiencies covering energy range of 662–1836 keV for different values of the lateral dead layer thickness

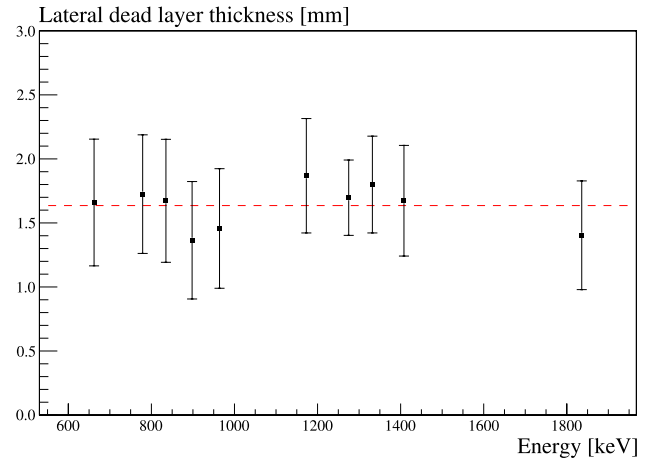


Fig. 10 Thickness of lateral dead layer obtained from linear interpolation covering the energy range of 662–1836 keV

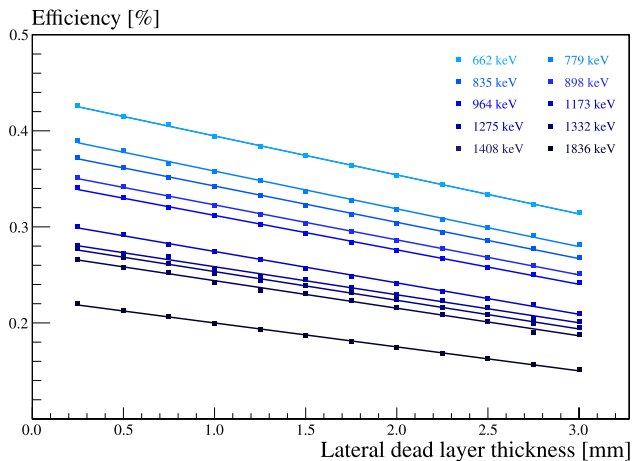


Fig. 8 Dependency of FEP efficiency at a given photon energy in relation to the thickness of the lateral dead layer

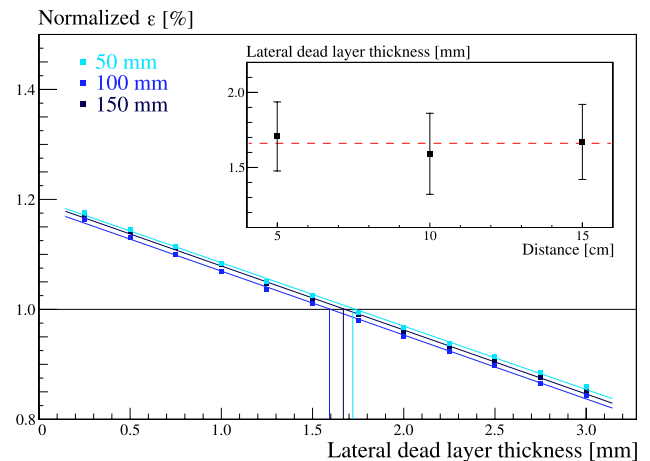


Fig. 11 Interpolation of normalized efficiency at 662 keV line from ^{137}Cs measured at three distances from the detector

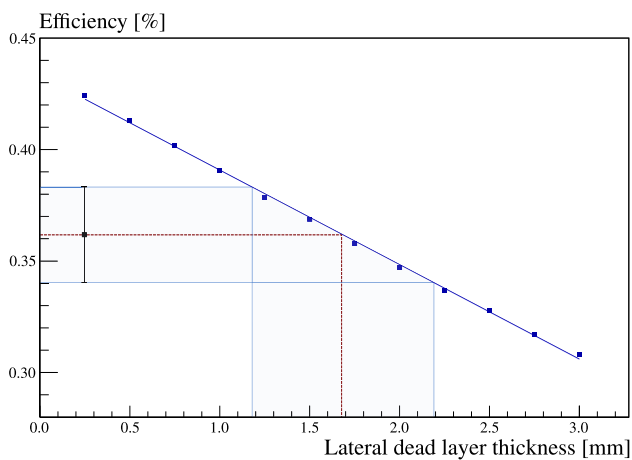


Fig. 9 An example of experimental efficiency interpolation on the linear fit obtained from simulated FEP efficiencies

were considered as completely inactive layers with no charge collection and were split into two parts: lateral (side) and top dead layer. Each part was individually optimized, since different thicknesses were expected (due to detectors entry window, top layer was expected to be thinner).

First adjustments were made for the lateral dead layer. For this, the efficiencies in the energy range of 662–1836 keV for measuring configuration of sources at a distance of 150 mm were used. With photon energies high enough the attenuation effects within the absorbing layers between the source and the active volume of the crystal are negligible. Therefore, since top dead layer doesn't play a significant role at these energies it was excluded for the time being. Simulated efficiencies in this energy region for different values of lateral dead layer thickness are illustrated in Fig. 7. Figure 8 shows the decrease of FEP efficiency at a given

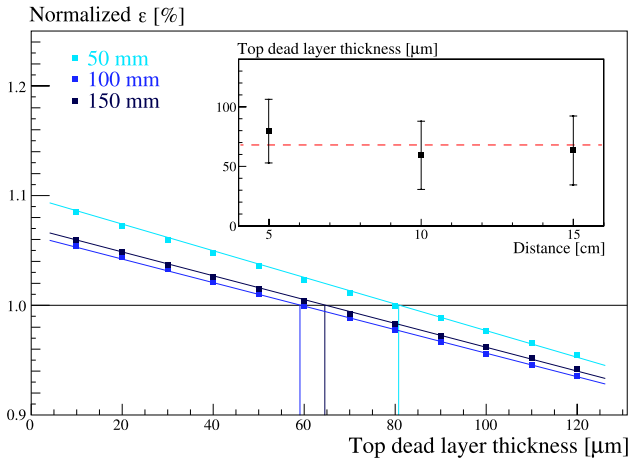


Fig. 12 Interpolation of normalized efficiency at 59 keV line from ²⁴¹Am measured at three distances from the detector

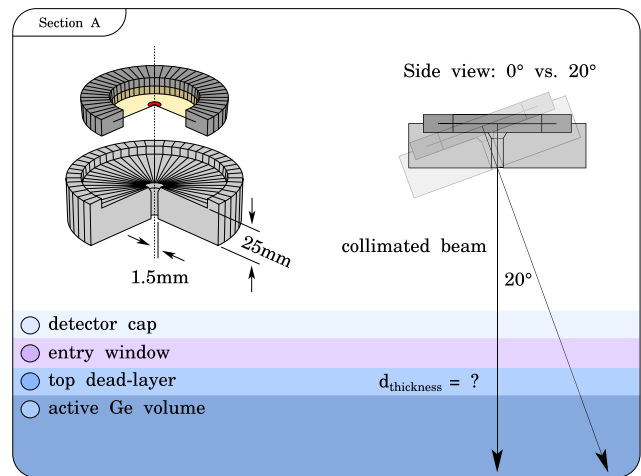
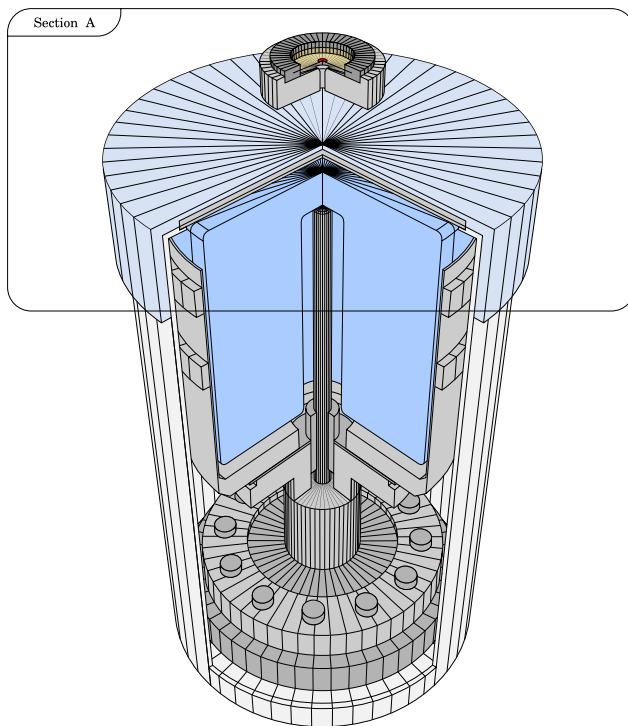
photon energy for different values of dead layer thicknesses. Clearly there is good linearity between the simulated efficiencies and the thicknesses of the lateral dead layer. These values were thus fitted using linear function with the value of adjusted R-squared of greater than 0.995 for all investigated photon energies.

The thickness of the lateral dead layer for a given photon energy was then interpolated based on these linear functions using the experimental FEP efficiency value as a reference

point. Example of this interpolation for energy of 662 keV in the case of ¹³⁷Cs is illustrated in Fig. 9. Interpolated values corresponding to different photon energies with an average thickness of 1.62 mm are shown in Fig. 10. In order to corroborate this value another measurement was carried out using ¹³⁷Cs source measured at three different distances from the end-cap of the detector (50 mm, 100 mm and 150 mm). Value of lateral dead layer thickness was then obtained with previously described interpolation on the linear fits (Fig. 11). Average thickness from this measurement was obtained to be 1.66 mm which is in good agreement with previously obtained value.

Top dead layer

Similar approach was adopted for the adjustment of top dead layer. Figure 12 shows efficiency dependance on the thickness of the top dead layer for 59 keV photons from ²⁴¹Am source measured at three different distances from the end-cap of the detector (50 mm, 100 mm and 150 mm). Average thickness of the top dead layer obtained in this way was 67.4 μm. In contrast to lateral, the top dead layer is significantly thinner which was expected due to the detectors entry window. However, in order to experimentally corroborate this another measurement using collimator made out of brass and again ²⁴¹Am source was performed (setup illustrated in Fig. 13). In total two measurements were carried out. In the



Mass attenuation coefficients

	μ_m [cm ² /g]
○ air (atmosphere)	0.188441
○ detector cap (polyethylene)	0.197523
○ detector entry window (cfrp)	0.175841
○ detector crystal (germanium)	2.083190

Fig. 13 Experimental setup using collimator and an ²⁴¹Am source for the estimation of the top dead layer. Table lists mass attenuation coefficients of different layers that photons traverse taken from NIST Standard Reference Database [21]

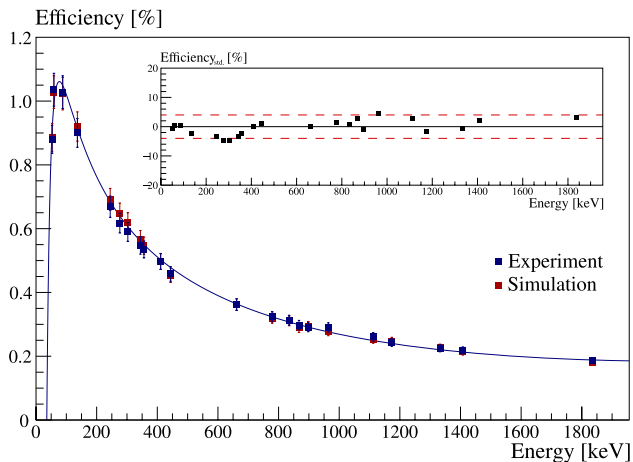


Fig. 14 Comparison of the experimental and simulated FEP efficiencies along with relative deviation between the two

first measurement the collimated beam from ^{241}Am source incident on the crystal was perpendicular in respect to crystals surface. In the second one the collimator was placed on a different mounting tilting the beam under a certain angle in respect to crystals axis (in our case the angle was 20°). This implies that photons have to traverse different lengths of layers in order to be detected. Both measurements were performed with source being at the same distance of 30 mm from the end-cap of the detector.

From photon intensity, given as:

$$I = I_0 e^{-\mu d} \quad (5)$$

where I is the photon intensity after they traverse the depth d of material with attenuation coefficient μ , while I_0 is the initial intensity, one can deduce the depth of the layers from the ratio of the two as:

$$\left. \begin{aligned} I_{20^\circ} &= I_0 e^{-\mu \frac{d}{\cos \alpha}} \\ I_{0^\circ} &= I_0 e^{-\mu d} \end{aligned} \right\} \mu d = \frac{\ln \frac{I_{20^\circ}}{I_{0^\circ}}}{1 - \frac{1}{\cos \alpha}} \quad (6)$$

where

$$d_{\text{Ge}} = \left(\frac{\ln \frac{I_{20^\circ}}{I_{0^\circ}}}{1 - \frac{1}{\cos \alpha}} - \sum_{i=1}^n d_i \mu_i \rho_i \right) / \mu_m(\text{Ge}) \rho_{\text{Ge}} \quad (7)$$

where the summation term represents each known layer that photons traverse before finally depositing their energy in the crystal and being detected.

Thickness of the top dead layer obtained using this approach was estimated to be $71.8 \mu\text{m}$ which is in good agreement with previously obtained simulated value. Comparison between the experimental FEP efficiencies and the

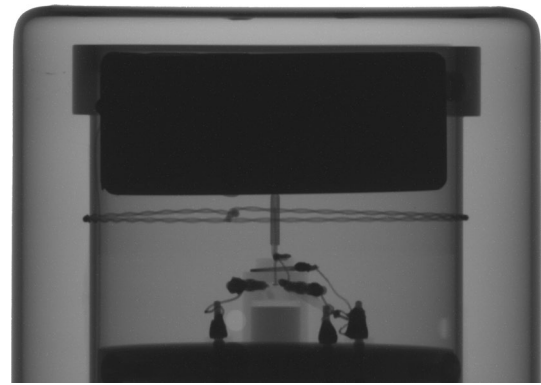


Fig. 15 Radiography scan of the LEGe detector (GL2020) showing the inner components of the detector in great detail

Table 5 Information from the manufacturer along with data obtained through radiography scan

Physical characteristics	Nominal	Scan
Crystal diameter	50	50.52
Crystal height	20	20.37
End-to-cap distance	5	5.0
Entry-window thickness	0.5	/
Cup end thickness	/	1.54
Cup outer diameter	/	77.35
Cup inner diameter	/	73.65
Top holder ring outer diameter	/	59.24
Crystal holder outer diameter	/	54.13
Crystal holder inner diameter	/	51.97
Crystal bulletization (average)	/	1.9
Cup rounded corner outer radius	/	4.09
Cup rounded corner inner radius	/	2.47

Values are given in mm

final simulation model covering full studied energy range (53–1836 keV) is given in Fig. 14.

LEGe detector optimization

Additionally, after performing the optimization on the XtRa detector, the code was also applied to a different detection equipment. This time around the optimization was not as detailed as it was primarily done only to check to a certain extent the validity of the code when applied to a different setup as well as to test the quickness of its implementation. For this purpose, our colleagues from Centre for Energy Research in Budapest have provided us with one of their detection devices. The detector in question is

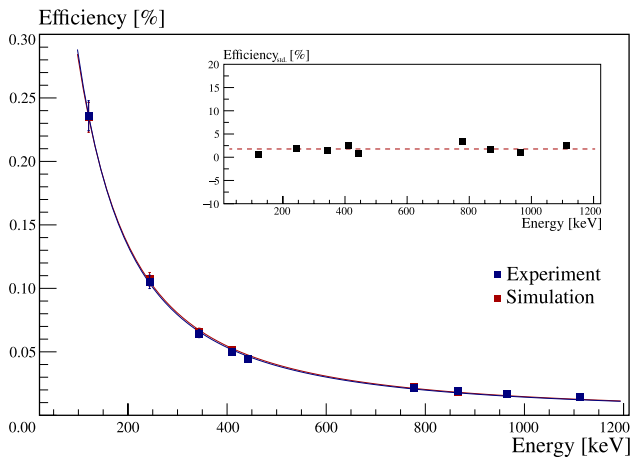


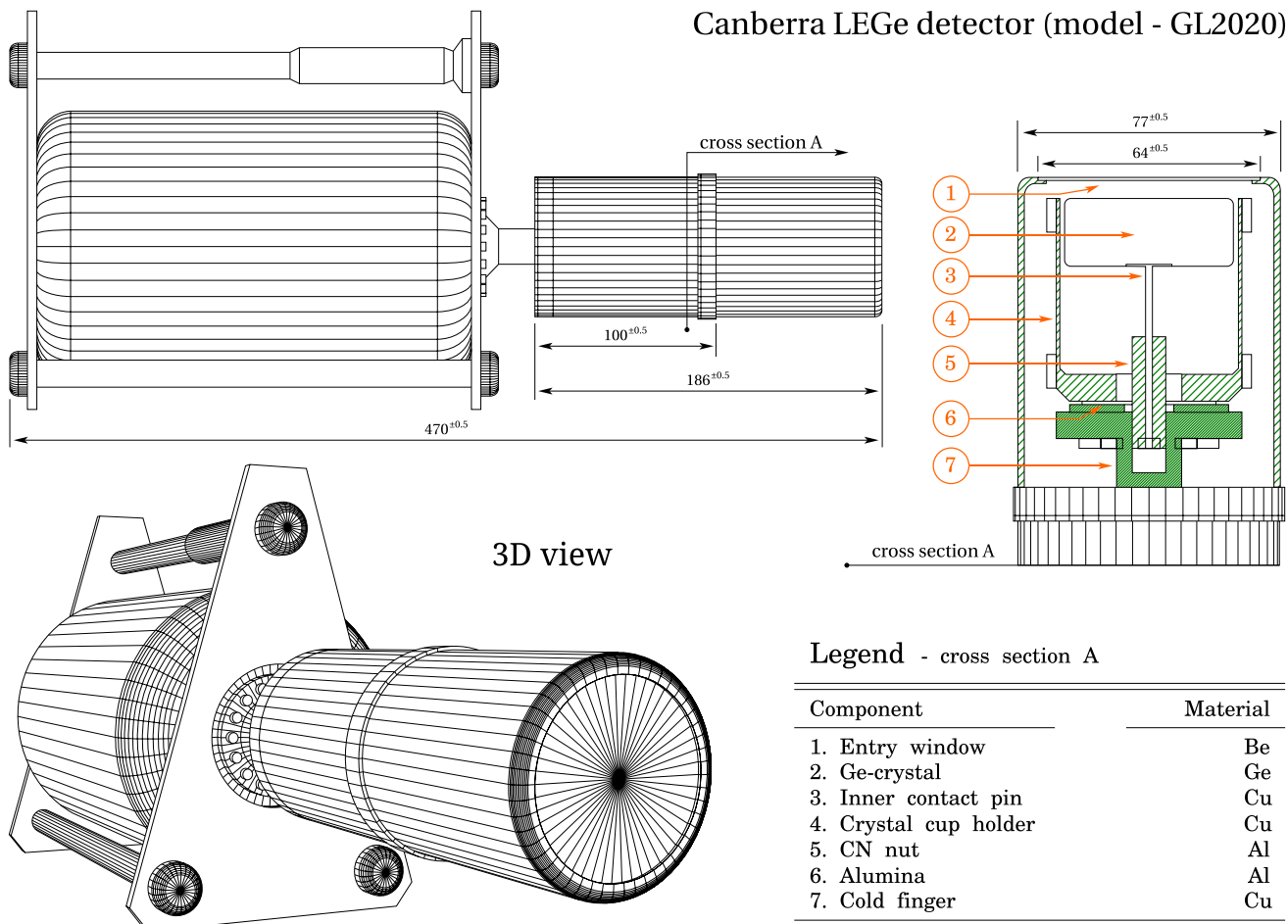
Fig. 16 Schematic diagram of the LEGe detector (Low Energy range Germanium, model GL2020, Canberra, Mirion Inc.) along with its 3D model and a listing of its inner components and materials

a Low Energy high-purity Germanium (LEGe) detector, model no. GL2020, manufactured by Canberra. This detector has a crystal of 20 mm thickness with an upper active

area of ~2000 mm² and an energy resolution of 400 eV and 680 eV at energies 5.9 keV and 122 keV, respectively. It is designed with thin front and side contacts, while the rear contact is significantly less in surface than crystals full lower area which provides lower detector capacitance. To further improve efficiency performance of the detector at low-energy part of the spectrum it is equipped with an entry window made of beryllium of 0.5 mm in thickness.

In contrast to GX10021 model, the GL2020 model came with a slightly more detailed documentation on its specifications. However, what makes this detector stand out in regards to the previously described one in terms of available information, is that it went under a radiography scan which provided a detailed imaging of its inner structure. This represented a significant source of information on its construction which greatly facilitated the process of creating its MC model. Image obtained through this scan, displayed in Fig. 15, allowed determining in greater detail the components of the detector as well as their dimensions, some of which are the thickness of the aluminium housing, position and outer dimensions of the crystal, crystals bulletization, crystal-to-window distance, etc. Detailed listing of the

Canberra LEGe detector (model - GL2020)



Legend - cross section A

Component	Material
1. Entry window	Be
2. Ge-crystal	Ge
3. Inner contact pin	Cu
4. Crystal cup holder	Cu
5. CN nut	Al
6. Alumina	Al
7. Cold finger	Cu

Fig. 17 Comparison of the experimental and simulated FEP efficiencies along with relative deviation between the two

dimensions of different detector components are given in Table 5. Technical drawing of GL2020 detector along with its 3D model is illustrated in Fig. 16.

Experimental calibration of detection equipment was carried out using a point-like standard gamma calibration ^{152}Eu source measured at 25 cm distance from the end-cap of the detector and thus covering energy range of 121–1112 keV. As before, the source is hot sealed between two polyimide foils with active area of around 2 mm in diameter. Because of the more detailed information on the equipment thanks to radiography imaging the MC modelling was significantly faster as there was no need to check for additional things (e.g. possible crystal displacement, “Dead layers tuning” section). Optimized model of the GL2020 detector showed good agreement with the experimental data that falls under an average relative deviation of ~1.8% for the studied energy range (Fig. 17). This can also further be improved upon by expanding the studied energy range using additional calibration sources, but it only shows that the more detailed documentation and information on the equipment plays a significant role in the process of optimizing detection equipment through Monte Carlo simulations.

Conclusion

Here presented study describes in detail a procedure for optimization of a coaxial p-type HPGe detector. Four detector parameters including the radius and height of the inner crystals cavity as well as the thickness of the lateral and top dead layers were tuned with the goal of achieving better results. Dead layers were adjusted based on the interpolation of the experimental efficiencies into the linear functions, which were determined by the fitting of the simulated efficiencies. For detector model GX10021 simulated FEP efficiencies obtained using the optimized model showed good agreement with the experimental data for a given measuring configuration. An average relative deviation of ~2% between the two for energy range of 53–1836 keV was achieved. Additionally, the code was applied on a different detection equipment (detector model GL2020) where an average relative deviation of ~1.8% was achieved for energy range of 121–1112 keV.

Acknowledgements Presented work was supported by the Ministry of Education, Science and Technological Development of the Republic of Serbia through Grants for PhD students (PhD grant OI 171002), IAEA Coordinated Research Project RC 23159. The authors would also like to thank Gamma Spectrometry team (Nuclear Security Department) and Radiography team (Nuclear Analysis and Radiography Department) from the Centre for Energy Research, Budapest, Hungary, for the data about LEGe detector.

References

- Conti CC, Salinas ICP, Zylberberg H (2013) A detailed procedure to simulate an HPGe detector with MCNP5. *Prog Nucl Energy* 66:35–40
- Jeřkovský M, Javorník A, Breier R, Slučiak J, Povinec PP (2019) Experimental and Monte Carlo determination of HPGe detector efficiency. *J Radioanal Nucl Chem* 322:1863–1869
- Saraiva A, Oliveira C, Reis M, Portugal L, Paiva I, Cruz C (2016) Study of the response of an ORTEC GMX45 HPGe detector via multi-radionuclide volume source using Monte Carlo simulations. *Appl Radiat Isot* 113:47–52
- Monte Carlo N-Particle code (MCNP) <https://mcnp.lanl.gov/>
- Geant4 <https://geant4.web.cern.ch/>
- LabSOCS <https://www.mirion.com/products/labsoocs-calibration-software>
- ANGLE <https://www.angle.me/>
- Vidmar T (2005) EFFTRAN-A Monte Carlo efficiency transfer code for gamma-ray spectrometry. *Nucl Instrum Methods Phys Res Sect A* 550:603–608
- Hurtado S, García-León R, García-Tenorio R (2004) GEANT4 code for simulation of a germanium gamma-ray detector and its application to efficiency calibration. *Nucl Inst Methods Phys Res A* 518:764–774
- FLUKA <http://www.fluka.org/fluka.php>
- PENELOPE <http://pypenelope.sourceforge.net/index.html>
- Trang LTN, Chuong HD, Thanh TT (2020) Optimization of p-type HPGe detector model using Monte Carlo simulation. *J Radioanal Nucl Chem* 327:287–297
- Khan W, Zhang Q, He C, Saleh M (2018) Monte Carlo simulation of the full energy peak efficiency of an HPGe detector. *Appl Radiat Isot* 131:67–70
- Khedr HI, Abdelati M, El Kourghly KM (2019) Investigation of a HPGe detector's geometry using X-Ray computed tomography in collaboration with Monte Carlo method. *Int J Eng Appl Sci* 6:42–46
- Joel GSC, Maurice NM, Jilbert NME, Ousmanou M, David S (2018) Monte Carlo method for gamma spectrometry based on GEANT4 toolkit: efficiency calibration of BE6530 detector. *J Environ Radioact* 189:109–119
- Elanique A, Marzocchi O, Leone D, Hegenbart L, Breustedt B, Oufni L (2012) Dead layer thickness characterization of the HPGe detector by measurements and Monte Carlo simulations. *Appl Radiat Isot* 70:538–542
- Tsang RHM, Pieke A, Auty DJ, Cleveland B, Delaquais S, Dideridze T, MacLellan R, Meng Y, Nusair O, Told T (2019) GEANT4 models of HPGe detectors for radioassay. *Nucl Instrum Methods Phys Res Sect A* 935:75–82
- Genie2KTM <https://www.mirion.com/products/genie-2000-basic-spectroscopy-software>
- NNDC - Brookhaven National Laboratory <https://www.nndc.bnl.gov/>
- Nikolić JD, Joković D, Todorović D, Rajačić M (2014) Application of GEANT4 simulation on calibration of HPGe detectors for cylindrical environmental samples. *J Radiol Prot* 34:47–55
- NIST—Standard Reference Database. <https://physics.nist.gov/PhysRefData/XrayMassCoeff/tab3.html>

Publisher's Note Springer Nature remains neutral with regard to jurisdictional claims in published maps and institutional affiliations.

Springer Nature or its licensor (e.g. a society or other partner) holds exclusive rights to this article under a publishing agreement with the author(s) or other rightsholder(s); author self-archiving of the accepted manuscript version of this article is solely governed by the terms of such publishing agreement and applicable law.

Article

Further Study of the Relationship between Transient Effects in Energetic Proton and Cosmic Ray Fluxes Induced by Coronal Mass Ejections

Mihailo Savić ^{1,*} , Nikola Veselinović ¹ , Darije Maričić ², Filip Šterc ², Radomir Banjanac ¹, Miloš Travar ¹ and Aleksandar Dragić ¹ 

- ¹ Institute of Physics Belgrade, University of Belgrade, Pregrevica 118, 11080 Belgrade, Serbia; veselinovic@ipb.ac.rs (N.V.); banjanac@ipb.ac.rs (R.B.); mtravar@ipb.ac.rs (M.T.); dragic@ipb.ac.rs (A.D.)
² Astronomical Observatory Zagreb, Opatička 22, 10000 Zagreb, Croatia; dmaricic@zvjezdarnica.hr (D.M.); fsterc@zvjezdarnica.hr (F.Š.)
* Correspondence: msavic@ipb.ac.rs

Abstract: The study and better understanding of energetic transient phenomena caused by disturbances occurring on our Sun are of great importance, primarily due to the potential negative effects those events can have on Earth's environment. Here, we present the continuation of our previous work on understanding the connection between disturbances in the flux of energetic particles induced in the near-Earth environment by the passage of interplanetary coronal mass ejections and related Forbush decrease events. The relationship between the shape of fluence spectra of energetic protons measured by the instruments on the SOHO/ERNE probe at Lagrange point L1, Forbush decrease parameters measured by the worldwide network of neutron monitors, and coronal mass ejection parameters measured in situ is investigated. Various parameters used to characterize transient phenomena and their impact on the heliosphere, provided by the WIND spacecraft, were utilized to improve the accuracy of the calculation of the associated energetic proton fluence. The single and double power laws with exponential rollover were used to model the fluence spectra, and their effectiveness was compared. Correlation analysis between exponents used to characterize the shape of fluence spectra and Forbush decrease parameters is presented, and the results obtained by the two models are discussed.

Keywords: coronal mass ejections; solar energetic particles; solar wind; space weather; cosmic rays; Forbush decreases



Citation: Savić, M.; Veselinović, N.; Maričić, D.; Šterc, F.; Banjanac, R.; Travar, M.; Dragić, A. Further Study of the Relationship between Transient Effects in Energetic Proton and Cosmic Ray Fluxes Induced by Coronal Mass Ejections. *Universe* **2024**, *10*, 283. <https://doi.org/10.3390/universe10070283>

Academic Editor: Alexandre Marcowith

Received: 14 March 2024

Revised: 24 June 2024

Accepted: 25 June 2024

Published: 29 June 2024



Copyright: © 2024 by the authors. Licensee MDPI, Basel, Switzerland. This article is an open access article distributed under the terms and conditions of the Creative Commons Attribution (CC BY) license (<https://creativecommons.org/licenses/by/4.0/>).

1. Introduction

The study of eruptive events on the sun and associated disturbances in the heliosphere is of great importance, largely due to the potential hazards they can pose to many areas of modern life. This is especially true at the present time, given the increased likelihood of their occurrence in the rising phase of solar cycle 25.

Magnetic reconnection on the sun involves violent processes through which magnetic energy is transformed into other forms of energy, often resulting in solar flares (SFs) or coronal mass ejections (CMEs). SFs are sudden eruptive phenomena in the solar atmosphere's active regions, observed as a flash of electromagnetic radiation, and are frequently associated with CMEs [1,2]. CMEs are large-scale eruptions of magnetized plasma from the sun's corona into the interplanetary medium, where they can be referred to as interplanetary coronal mass ejections (ICMEs).

Solar flares and coronal mass ejections may induce complex disturbances in the heliosphere and Earth's magnetosphere. One such phenomenon includes particle acceleration that results in a flux enhancement of protons, electrons, and ions. These enhancements, typically referred to as solar energetic particle (SEP) events, can be measured in interplanetary

space by detectors onboard space probes, and in extreme cases, by Earth-based detectors. High-energy particles can be ejected and accelerated from the sun during SF events [3,4], or they can be accelerated by CME- and ICME-induced shock waves. These phenomena can accelerate SEPs to MeV or even GeV energies, reaching Earth usually within a day after their occurrence or even faster [5]. It is important to study not just the strong SEP events, which have the potential to affect our civilization [6], but also the weaker and more frequent ones. It is crucial to understand the circumstances under which they occur but also the parameters that describe the propagation and strength of these events [7].

Another way eruptive events on the sun can affect the near-Earth environment is through their impact on cosmic rays (CRs). Cosmic rays are high-energy charged particles that predominantly originate from outside our solar system, although some of these particles can originate from the sun. In the heliosphere, CRs interact with the interplanetary magnetic field (IMF), which is carried by the stream of supersonic plasma blowing outward from the sun known as the solar wind. Transients such as CMEs and ICMEs with accompanied bow shocks, created due to the interaction of faster ICME with slower solar wind, can modulate CRs [8,9]. This modulation of CRs can be detected on Earth as a sudden offset in the CR flux, followed by a gradual recovery phase that can last several days [10,11], an effect commonly known as a nonrecurrent Forbush decrease (FD). Thus, the observed change in CR flux can be used as a proxy for solar activity.

These are just some of the numerous phenomena that can occur in the heliosphere and are associated with the sun's activity. To maximize our understanding of such complex events, we must investigate all the interconnections among the various induced processes. In this work, we expand on our previous study of one such relationship [12], specifically the connection between the enhanced flux of solar energetic particles and the properties of concurrent Forbush decreases, which have also been observed and studied by other authors [13,14]. The main idea behind the study is that, on one hand, the passage of a CME/ICME can lead to particle acceleration and an increase in the detected flux of energetic particles, while on the other hand, it may cause a decrease in the observed flux of CRs or the aforementioned Forbush decrease. To investigate the connection between these two phenomena, we examined the correlation between the shape of the event-integrated differential SEP flux, or differential fluence, measured at Lagrange point 1 (L1), and the magnitudes of associated FDs. To extend and potentially refine our previous study, we implemented several improvements. These features include the utilization of high-resolution data for the IMF, solar wind, and CME speeds in order to increase the precision in determining the onset and duration of events. Furthermore, we introduced an additional model for the description of the fluence spectra to be used alongside and compared with the previously used one. Finally, we applied a new fitting procedure based on the Monte Carlo approach. We believe these improvements lead to noticeably more precise and reliable results that further support the proposed relationship between the shape of the differential fluence spectra and the magnitudes of FDs.

In the article, we first discuss various data sources used in the analysis and justify the selection of events from solar cycles 23 and 24. We then describe in detail the procedure used to determine the differential SEP fluence spectra. In the next section, we introduce two models that were used to parameterize the fluence spectra and compare how well they were able to fit the data. Finally, we perform the correlation analysis to study the dependence between FD parameters and the spectral indices of SEP fluence spectra, as well as the selected CME parameters. We discuss the results in terms of the models applied and evaluate the usefulness of obtained indices as predictors of FD properties.

2. Data and Event Selection

2.1. Data Sources

Various types of data were necessary for the presented study, including energetic proton data measured near Earth, selected IMF, CME, solar wind, and geomagnetic field parameters, as well as CR measurements by Earth-based detectors. The data are available

either in the form of time series or as extreme and averaged values over the duration of the event. Two main repositories were used to acquire these data: the OMNIWeb Plus repository provided by the NASA/Goddard Space Flight Center [15] (for energetic proton data and time series of IMF and solar wind speeds) and the IZMIRAN Forbush decrease database provided by the Pushkov Institute of Terrestrial Magnetism, Ionosphere, and Radio Wave Propagation, Russian Academy of Sciences [16] (for Forbush decrease and averaged space weather parameters).

Energetic proton data in the OMNIWeb Plus repository are provided by the Energetic and Relativistic Nuclei and Electron (ERNE) sensor unit onboard the Solar and Heliospheric Observatory (SOHO) [17]. SOHO is situated in a halo orbit around L1. SOHO/ERNE has two energetic particle sensors: the Low-Energy Detector (LED) and the High-Energy Detector (HED), each with ten energy channels measuring ion fluxes and count rates in the ranges of 1.3–13 MeV/nucleon and 13–130 MeV/nucleon, respectively. This setup has been actively monitoring differential proton flux over the course of the last three solar cycles [18,19]. For this study, hourly data of energetic protons were used.

IMF and solar wind speed data in the OMNIWeb Plus repository were provided by the Global Geospace Science (GGS) WIND spacecraft. The spacecraft was positioned upstream of Earth at L1, initially in a Lissajous orbit and then, more recently, inserted into a halo orbit around L1. The primary goal of the mission has been to monitor the properties of the solar wind, a task that its onboard instruments have successfully performed over the last three decades [20].

Various space weather parameters associated with a specific FD event were taken from the database of Forbush decreases compiled by researchers from IZMIRAN. FD magnitudes in the database are obtained using measurements from the worldwide network of neutron monitors (the most widely used type of ground-level CR detectors). Neutron monitor data were corrected for efficiency and atmospheric effects. Other space weather data in the IZMIRAN database were assembled from various sources to produce a comprehensive repository containing various associated parameters of FDs, the heliosphere, and the geomagnetic field. In this study, we used parameters related to CMEs and solar wind, such as average CME speed and maximum solar wind speed, as well as the minimal Disturbance Storm-Time index (Dst) over the duration of the FD event. We also used FD magnitudes calculated by the IZMIRAN researchers using the global survey method (GSM) technique [21]. GSM integrates measurements from a worldwide network of neutron monitors, accounting for all effects caused by various anisotropies and disturbances of atmospheric and geomagnetic origin, to derive the hourly variation of primary cosmic ray flux outside Earth's atmosphere. In addition to FD magnitudes measured at Earth, they also provide the values of FD magnitudes corrected for the magnetospheric effect, which should remove the contribution of the disturbances introduced by variations in the geomagnetic field.

2.2. Event Selection

In this study, we focused on the events that occurred during most of the solar cycle 23 and 24. To establish the connection between the shape of energetic proton fluence spectra and the properties of concurrent Forbush decrease (FD) events, we decided to focus on events with larger magnitudes, expecting the correlation to be more pronounced in such cases due to less noise from noncontributing processes. The lower boundary for FD magnitude for event selection was somewhat arbitrarily set to 4%. Further lowering this bound would certainly increase the statistics in the analysis, but we do not believe it would add much support to the proposed relationship, due to the non-negligible likelihood that events of lower magnitude may exhibit different behavior from events of larger magnitudes (which is further discussed in Section 5). However, there are plans to investigate this in more detail in the future and possibly extend the analysis to include events of lower magnitudes.

The term SEP event can be somewhat misleading due to two possible processes leading to particle acceleration, so we feel we should clarify the nature of the events used in this

work. Evidence of two distinctive physical mechanisms of SEP acceleration has been accumulating for the last half-century [4]. The first of the two mechanisms is associated with type II radio bursts from coronal and interplanetary shock waves, while the second is associated with type III radio bursts produced by streaming electrons. The former is driven by fast CMEs, is proton-dominated, and produces “gradual” SEP events (sometimes also referred to as Energetic Storm Particle, or ESP events) that have high SEP flux intensity near Earth. The latter mechanism is predominantly connected to magnetic reconnection with open magnetic field lines and resonant wave–particle interactions in impulsive SFs and jets. It produces “impulsive” SEP events that last for hours, in contrast to gradual events, which can last for days partly due to the continuing acceleration of the shock. Even though all of the CMEs used in the analysis can be associated with SFs, we believe all of them belong to the gradual SEP event class.

Determining event-integrated SEP fluence was not always simple, especially in the case of complex events where structures that appear to have different sources are superimposed. That is why we have decided to eliminate all events for which we did not find a clear association with the passage of a specific CME, leaving us with 20 events to be used in the analysis. Selected FD events and their respective parameters from the IZMIRAN database are shown in Table 1.

Table 1. Selected parameters from the IZMIRAN database associated with FD events: FD magnitude for particles with 10 GV rigidity (M), FD magnitude for particles with 10 GV rigidity corrected for magnetospheric effect (M_M), average CME speed between the Sun and the Earth calculated from the beginning of the associated CME (V_{meanC}), maximal hourly solar wind speed during the event (V_{max}), and minimal Dst index during the event (Dst_{min}).

Date/Time of FD Onset	M [%]	M_M [%]	V_{meanC} [kms ⁻¹]	V_{max} [kms ⁻¹]	Dst_{min} [nT]
29–Sep–2001 09:40:00	4.3	4.4	831	694.0	–56.0
11–Oct–2001 17:01:00	7.0	6.9	769	572.0	–71.0
21–Oct–2001 16:48:00	5.4	7.3	858	677.0	–187.0
24–Nov–2001 05:56:00	9.2	9.8	1366	1024.0	–221.0
17–Apr–2002 11:07:00	6.2	7.0	745	611.0	–127.0
07–Sep–2002 16:36:00	4.6	5.1	863	550.0	181.0
30–Oct–2003 16:19:00	14.3	9.4	2140	1876.0	383.0
20–Nov–2003 08:03:00	4.7	6.8	872	703.0	422.0
26–Jul–2004 22:49:00	13.5	14.4	1290	1053.0	197.0
13–Sep–2004 20:03:00	5.0	5.3	948	613.0	50.0
15–May–2005 02:38:00	9.5	12.2	1231	987.0	263.0
14–Dec–2006 14:14:00	8.6	9.6	1165	955.0	146.0
05–Aug–2011 17:51:00	4.3	4.8	1104	611.0	–115.0
24–Oct–2011 18:31:00	4.9	6.5	633	516.0	–147.0
08–Mar–2012 11:03:00	11.7	11.2	1188	737.0	143.0
14–Jul–2012 18:09:00	6.4	7.6	834	667.0	–127.0
23–Jun–2013 04:26:00	5.9	5.3	844	697.0	–49.0
12–Sep–2014 15:53:00	8.5	5.9	897	730.0	–75.0
22–Jun–2015 18:33:00	8.4	9.1	1040	742.0	–204.0
07–Sep–2017 23:00:00	6.9	7.7	1190	817.0	–124.0

3. Determination of Energetic Proton Fluence Spectra

Establishing a clear connection between a CME originating on the sun and a consequent FD is often not straightforward [22]. Due to the many potential interactions that can occur in the heliosphere, the same can be true when one tries to establish the effect of an ICME passage on the observed flux of energetic protons in interplanetary space.

Complex events on the sun and related disturbances in the heliosphere include various processes that can lead to particle acceleration and contribute to an increased flux of energetic protons [23]. Hence, the direct link between the structures observed in the energetic proton flux time series and the passage of an ICME is not always obvious. To establish this link as reliably as possible, we utilized data provided by various instruments onboard the WIND spacecraft. As our primary interest was the determination of the precise timing of the onset and duration of the interaction, we found the time series of the IMF and CME velocity to be the most useful parameters for this purpose available in the WIND data.

To illustrate the usefulness of WIND data for this purpose, Figure 1 shows the time series for the IMF (both the total magnitude and its components), solar wind velocity, and the flux of energetic protons for one selected channel (1.3–1.6 MeV/nucleon) measured by the SOHO/ERNE instrument for the November 2001 event. Vertical dashed lines indicate the time intervals associated with the shock-sheath region and the ICME itself (from left to right, respectively). Some of the analyzed events are forming complex magneto-plasma structures, which can be explained by interactions with high-speed solar wind streams or other ICMEs.

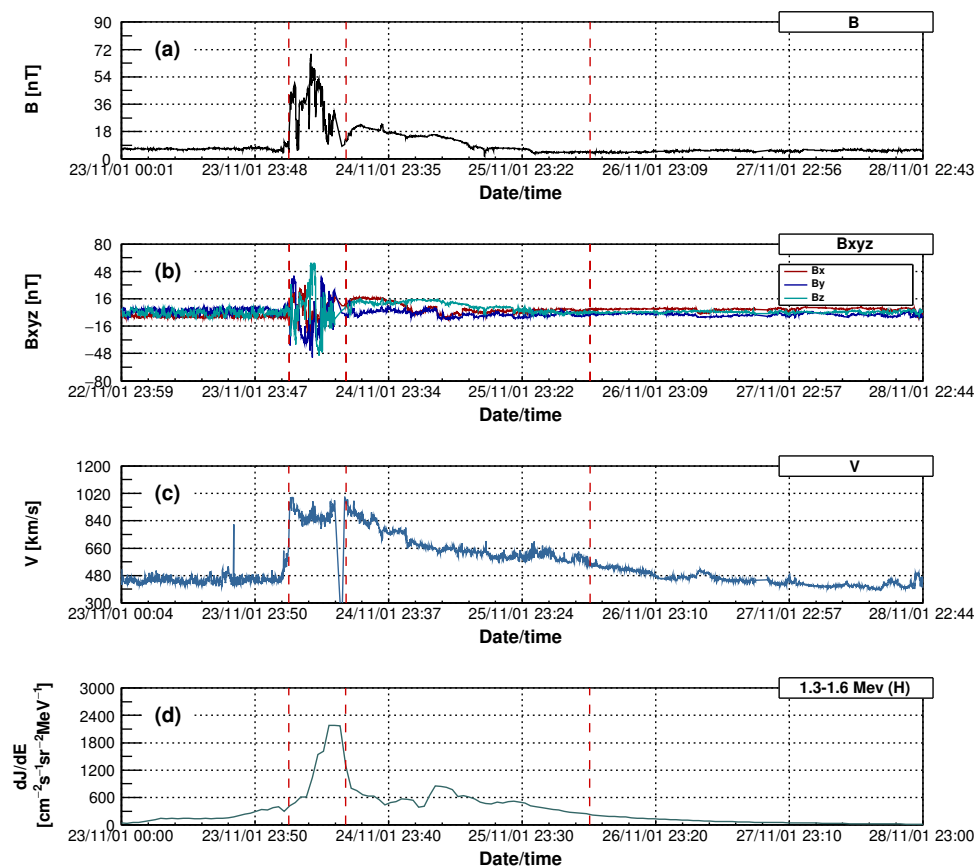


Figure 1. Time series for selected WIND parameters and SOHO/ERNE proton flux data for the November 2001 event: (a) IMF, (b) IMF components, (c) solar wind speed, and (d) energetic proton flux in 1.3–1.6 MeV energy channel.

Considering the different time resolutions of WIND (92 s) and SOHO/ERNE data (1 h), which can result in slight hour-round-off time shifts of the time series for the latter,

we observe a clear impact of the arrival of the ICME shock on the flux of energetic protons. In addition to the increase in proton flux attributed to the passage of the ICME, there is a noticeable structure that seemingly precedes the ICME shock. This structure does not appear to be directly related to the variations in the IMF or solar wind velocity. Due to the general complexity of events on the sun, which typically lead to the formation of CMEs, and the different mechanisms of particle acceleration and interaction with the solar wind, it is possible that the detected increase in proton flux preceding the shock is induced by some other aspect of such phenomena or could be some kind of event precursor. We discuss the possible nature of this structure below; however, we believe that the absence of a detailed explanation of the mechanism behind its origin will not critically affect the procedure of determining differential proton fluence and the presented results. Nonetheless, it is definitely a feature that we will try to investigate in our future work, as we believe it will lead to a better overall understanding of complex space weather phenomena.

The times marking the shock and the end of ICME interaction, determined as explained in the previous paragraphs, are now used as integration bounds to calculate event-integrated flux (or differential fluence) for each of the SOHO/ERNE energy channels. An illustration of this procedure is shown in Figure 2 for four selected SOHO/ERNE channels.

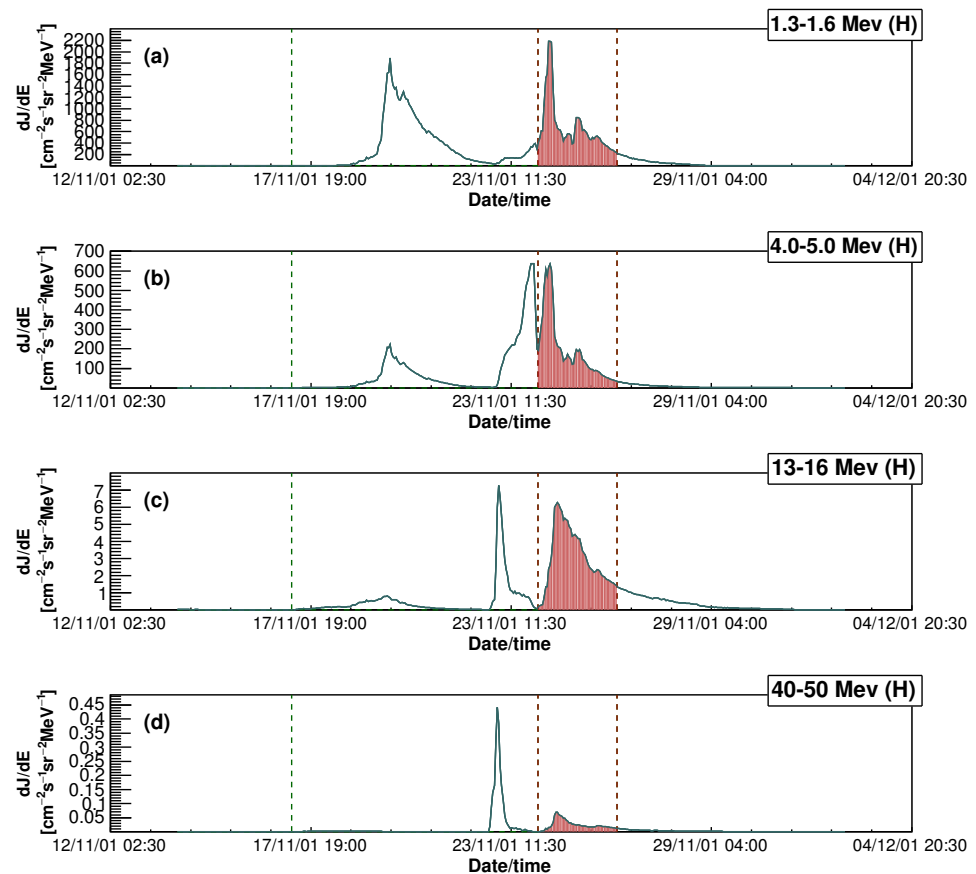


Figure 2. Energetic proton flux in four selected SOHO/ERNE energy channels for the November 2001 event: (a) 1.3–1.6 MeV, (b) 4.0–5.0 MeV, (c) 13–16 MeV, (d) 40–50 MeV. Green dashed line marks the end of the interval used to calculate the baseline, while the two red dashed lines indicate the bounds of the time interval used for integration.

Among the three vertical dashed lines, the second and the third ones mark the integration bounds, while the first one indicates the end of the time interval used to calculate the baseline value (the beginning of the baseline interval being the same as the beginning of the interval shown on the graph). In several cases where energetic proton flux preceding the event was disturbed for a longer period of time, a time interval after the event, when the

flux has recovered and was stable, was used. The duration of time intervals used for baseline determination ranged from a day and a half to several days. The filled area under the graph represents the differential fluence value for a given channel calculated relative to the baseline.

One can observe that part of the proton flux time series associated with the structure preceding the arrival of the shock exhibits a different energy dependence to the part we assume is induced by the passage of the ICME and its interaction with the local particles [24], as the relative ratio of the areas under respective profiles increases with increasing energy. This could indicate that the observed structure is not related to the CME but is a consequence of some other interaction.

In our previous work [12], due to the lack of high-resolution WIND data, integration intervals were more loosely defined. We were unable to precisely separate only the CME-induced part of the energetic proton flux, often including the precursor structure. We believe the new approach is a significant improvement and should lead to more reliable results.

4. Parametrization of Fluence Spectra

Using the values for differential energetic proton flux in different energy channels integrated over the duration of the event (as detailed in Section 3), we form the differential fluence spectra for selected events. The average energy in MeV was used for particle energy bin values [25].

Several models have been proposed over the years to describe the observed spectra [26]. One feature that has proven somewhat challenging to accurately describe is the characteristic brake or “knee”, which can be prominent in extreme events [27,28], possibly occurring due to the effect of interplanetary transport [29]. Previously [12], we relied on the model proposed by Band et al. [29,30] to fit the event-integrated fluence spectra. The model, originally developed to describe gamma-ray burst spectra but also successfully used to model fluence spectra [31], is based on the double power law in the following form:

$$\frac{dJ}{dE} = \begin{cases} AE^\alpha \exp\left(-\frac{E}{E_B}\right) & E \leq (\alpha - \beta)E_B, \\ AE^\beta [(\alpha - \beta)E_B]^{\alpha - \beta} \exp(\beta - \alpha) & E > (\alpha - \beta)E_B, \end{cases} \quad (1)$$

where E is the particle energy, E_B is the “knee” energy, α is the power law index that characterizes the low-energy part of the spectrum, β is the power law index that characterizes the high-energy part of the fluence spectrum, and A is the spectral coefficient.

While this model reasonably described the observed spectra for a number of events, in some cases, it seemed that the agreement could be better. Attempting to use the “knee” energy as a free parameter in the fitting procedure resulted in either fit instability or divergent fits. We believed this to be a consequence of the limitations of standard minimizers in handling a relatively large number of free parameters. To overcome this issue, in our previous analysis, we decided to treat the “knee” energy as a fixed parameter, determining E_B by relying on the dependence of this parameter on the integral fluence reported by some authors [28,32]. Additionally, the range conditions in Equation (1) were approximated using the expected values for indices α and β of -1 and -2 , respectively, as suggested in [30], effectively reducing the conditions for the low-energy and high-energy ranges to $E \leq E_B$ and $E > E_B$. However, the number of approximations needed to stabilize the fitting procedure seemed excessive, so considering an alternative approach seemed advisable.

To reduce potentially significant uncertainties and to increase the reliability of the fitting, in this study, we resorted to employing the procedure based on the Monte Carlo approach, specifically utilizing the *emcee* Python package. *emcee* is a robust, well-tested, and user-friendly MIT-licensed tool for Bayesian inference, which uses Markov Chain Monte Carlo (MCMC) sampling. It is based on the affine-invariant ensemble sampler and is widely and successfully applied in various research disciplines and data science domains, including astrophysics, biostatistics, and machine learning. We performed the fitting procedure using Equation (1) and setting all four parameters as free variables.

The fitting algorithm performed exceptionally well, rapidly and reliably converging to optimal parameter values with very high precision and minimal deviation between independent walkers. The approach led to a significantly improved and more stable fitting procedure, ultimately resulting in noticeably more reliable outcomes compared with our previous method.

Although fitting the energetic proton fluence spectra with the Band function using the MCMC method eventually performed remarkably well, the function was not so straightforward to implement when the fitting procedure was based on standard minimizer algorithms. Hence, we were interested in investigating whether a simpler and more robust model could be comparably effective in describing energetic proton spectra while also being easier to implement. One such model, proposed by Ellison and Ramaty, was developed based on observations of particle acceleration at interplanetary shocks [33], and was successfully used to model spectra of several particle species during large SEP events [34]. In these studies, it was concluded that for strong events it mainly fits the lower energy range satisfactorily. However, we felt it performed well enough to test it on the set of events we selected for the presented analysis. The model assumes the form of a power law with an exponential rollover to describe the energetic particle fluence spectra:

$$\frac{dJ}{dE} = AE^\gamma \exp\left(-\frac{E}{E_0}\right), \quad (2)$$

where E is the particle energy, E_0 is the cutoff exponent parameter, γ is the spectral index, and A is the spectral coefficient.

Even though it is one of the older proposed models, and some authors had objections to the somewhat arbitrary introduction of the rollover correction [32], we found the Ellison–Ramaty model to be mostly in good agreement with the observed data. Additionally, it proved to be robust in terms of the convergence of the fit. Hence, we felt it is a good candidate to compare against the model proposed by Band et al. to possibly determine if one is more suited than the other for the purpose of our analysis.

We fitted the fluence data with both Band and Ellison–Ramaty models and compared how accurately they described the observed spectra. The Ellison–Ramaty model mostly converged stably and performed reasonably well when used with standard minimizers. However, for a more accurate comparison of both models, we utilized the aforementioned implementation using the *emcee* package for the Ellison–Ramaty function as well. This indeed led to further improvements, greater accuracy, and increased precision of the fit results.

In direct comparison, the Band function proved to be an overall more flexible model, describing the spectra more accurately, particularly apparent in its ability to effectively model the “knee” feature. While in some cases this difference in performance was more evident, for the majority of events, the Ellison–Ramaty model seemed to describe the spectra sufficiently well, offering only a moderately poorer fit. In Figures 3 and 4, we show two events that best illustrate the different cases of the level of agreement between the two models.

The green line in Figures 3 and 4 represents the fit function given by Equation (1) (Band et al.), and the magenta line represents the fit function given by Equation (2) (Ellison–Ramaty). The left panels on both figures show the fluence spectrum in log–log scale, while the right panels zoom in on the region around the “knee” energy in linear scale, which proved to be the most demanding to fit adequately.

An example where the difference in performance between the two models is most apparent is the second event in October 2001 (occurring around October 21), shown in Figure 3. Here, the observed spectrum is clearly better described by Equation (1). The Ellison–Ramaty fit starts to diverge just after the “knee”, and although the divergence is not dramatic, it is still noticeable. However, in the case of the June 2013 event (Figure 4), the difference between the two models is much smaller, with Ellison–Ramaty providing only a marginally less accurate fit. We believe that the fact that the second situation is encountered more

often provides sufficient justification for continuing to use both models in the remainder of the analysis.

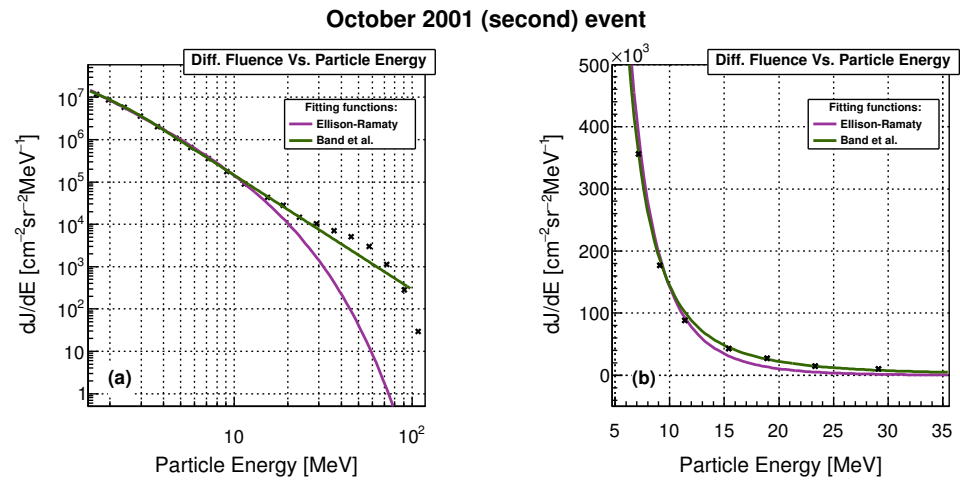


Figure 3. Fluence spectrum associated with the FD that occurred on 21 October 2001: (a) full range in log–log scale and (b) interval around the “knee” energy in linear scale. The green line indicates the fit by the Band et al. function, while the magenta line indicates the fit by the Ellison–Ramaty function.

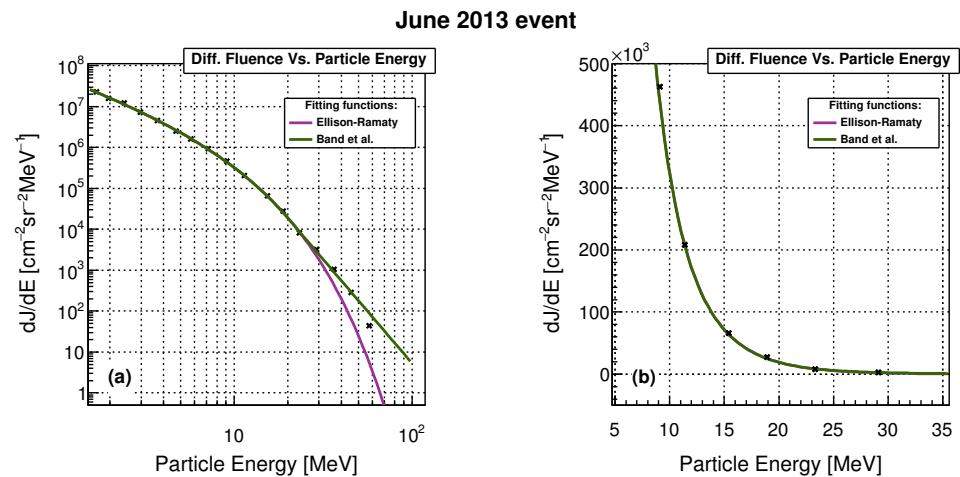


Figure 4. Fluence spectrum associated with the FD that occurred on 23 June 2013: (a) full range in log–log scale and (b) interval around the “knee” energy in linear scale. The green line indicates the fit by the Band et al. function, while the magenta line indicates the fit by the Ellison–Ramaty function.

The obtained spectral indices α , β , and γ , as well as the values for the ‘knee’ and roll-over energies, are shown in Table 2. Fit errors for all parameters are given in parentheses.

To further study and compare the usefulness of the models in describing the measured spectra, we performed a correlative analysis, presenting the results of both models in parallel.

Table 2. Parameters for the two models used to fit the fluence spectra for all events: spectral indices (α , β) and “knee” energy (E_B) for the Band et al. model, and spectral index (γ) and roll-over energy (E_0) for the Ellison–Ramaty model.

Date/Time of FD Onset	α	β	E_B [MeV]	γ	E_0 [MeV]
29–Sep–2001 09:40:00	−1.859(1)	−3.60(2)	11.71(5)	−1.806(1)	10.000(1)
11–Oct–2001 17:01:00	−1.229(8)	−4.130(4)	1.354(6)	−1.798(4)	1.999(6)
21–Oct–2001 16:48:00	−1.169(6)	−2.695(1)	2.44(2)	−1.918(2)	7.93(4)
24–Nov–2001 05:56:00	−0.375(1)	−5.537(5)	3.535(1)	−0.378(1)	3.548(1)
17–Apr–2002 11:07:00	−1.422(2)	−3.783(2)	2.529(4)	−1.667(1)	3.271(4)
07–Sep–2002 16:36:00	−1.866(1)	−4.73(2)	4.991(8)	−1.882(1)	5.122(7)
30–Oct–2003 16:19:00	−0.100(1)	−5.876(4)	3.271(1)	0.000(1)	3.071(1)
20–Nov–2003 08:03:00	−1.599(4)	−3.419(5)	3.45(2)	−1.801(2)	4.58(2)
26–Jul–2004 22:49:00	−1.234(1)	−4.910(7)	3.328(2)	−1.255(1)	3.404(2)
13–Sep–2004 20:03:00	−0.949(1)	−6.54(2)	3.467(1)	−0.951(1)	3.474(1)
15–May–2005 02:38:00	−0.431(1)	−7.37(4)	2.811(1)	−0.432(1)	2.813(1)
14–Dec–2006 14:14:00	−0.721(1)	−4.038(2)	2.200(1)	−0.841(1)	2.427(1)
05–Aug–2011 17:51:00	−1.532(1)	−4.70(1)	4.742(5)	−1.545(1)	4.837(5)
24–Oct–2011 18:31:00	−1.112(2)	−7.57(5)	1.641(1)	−1.119(1)	1.648(1)
08–Mar–2012 11:03:00	−0.677(1)	−3.642(1)	5.129(1)	−0.698(1)	5.286(1)
14–Jul–2012 18:09:00	−1.246(1)	−9.999(1)	2.496(1)	−1.245(1)	2.494(1)
23–Jun–2013 04:26:00	−1.560(1)	−5.08(3)	5.71(1)	−1.564(1)	5.752(9)
12–Sep–2014 15:53:00	−0.551(3)	−3.350(1)	1.287(2)	−1.699(1)	3.232(4)
22–Jun–2015 18:33:00	−1.382(1)	−6.21(2)	3.424(1)	−1.386(1)	3.437(1)
07–Sep–2017 23:00:00	−1.210(1)	−5.11(1)	4.553(3)	−1.216(1)	4.590(2)

5. Correlation between Spectral Indices and Forbush Decrease Parameters

To study the relationship between the enhanced flux of energetic protons accelerated by a CME/ICME-related interplanetary shock and the effect of the passage of these disturbances on cosmic rays, we investigate the correlation between spectral indices used to parameterize the shape of the energetic proton fluence spectra and the magnitudes of coincident Forbush decreases. FD magnitudes for 10 GV rigidity particles, calculated using GSM applied to neutron monitor data provided by the global neutron monitor network [35], are available in the IZMIRAN database. In addition to FD magnitudes measured at Earth, the database offers calculated values of FD magnitudes for 10 GV rigidity particles corrected for magnetospheric effects using the Dst index.

Figure 5 shows the dependence between the spectral index α , obtained by fitting the fluence spectra with the function proposed by Band et al., and FD magnitudes. The dependence for the measured FD magnitude (M) is shown in the left panel, while the dependence for FD magnitude corrected for magnetospheric effects (M_M) is shown in the right panel.

Equivalent plots for spectral index β are shown in Figure 6.

Figure 7 shows the relationship between FD magnitude and the spectral index γ , obtained by fitting the fluence spectra with the Ellison–Ramaty function. As in the previous figure, the dependence for the measured FD magnitude is shown on the left panel, while one for the FD magnitude corrected for magnetospheric effects is shown on the right panel.

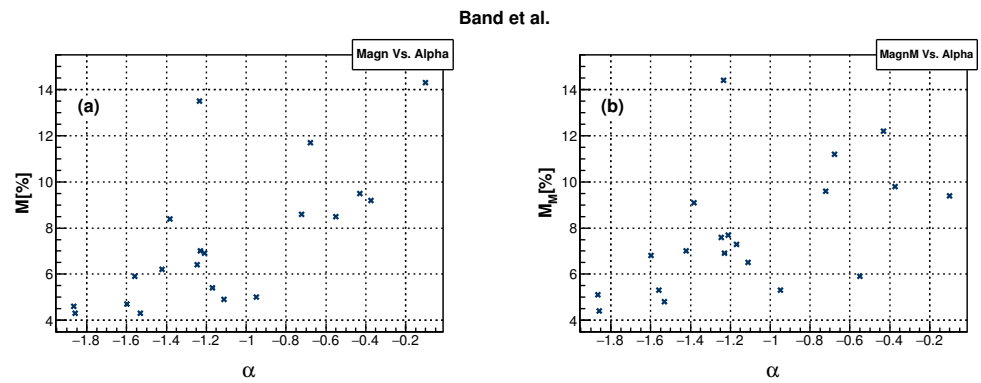


Figure 5. Dependence of FD magnitudes on the spectral index α for (a) FD magnitude for particles with 10 GV rigidity and (b) FD magnitude for particles with 10 GV rigidity corrected for magnetospheric effect.

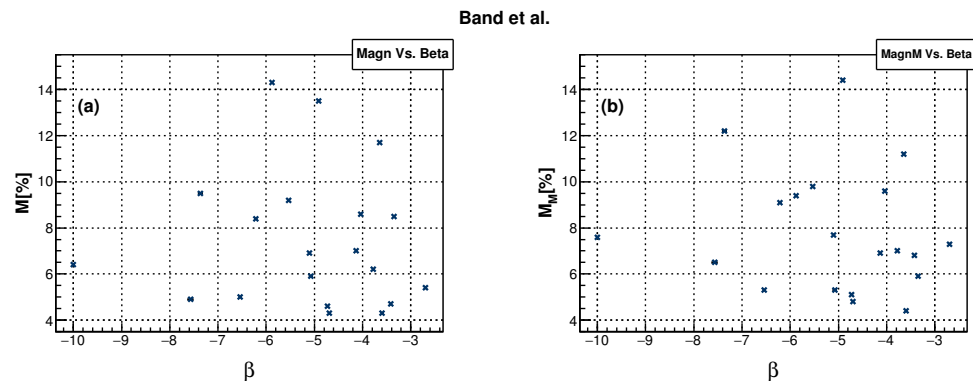


Figure 6. Dependence of FD magnitudes on the spectral index β for (a) FD magnitude for particles with 10 GV rigidity and (b) FD magnitude for particles with 10 GV rigidity corrected for magnetospheric effect.

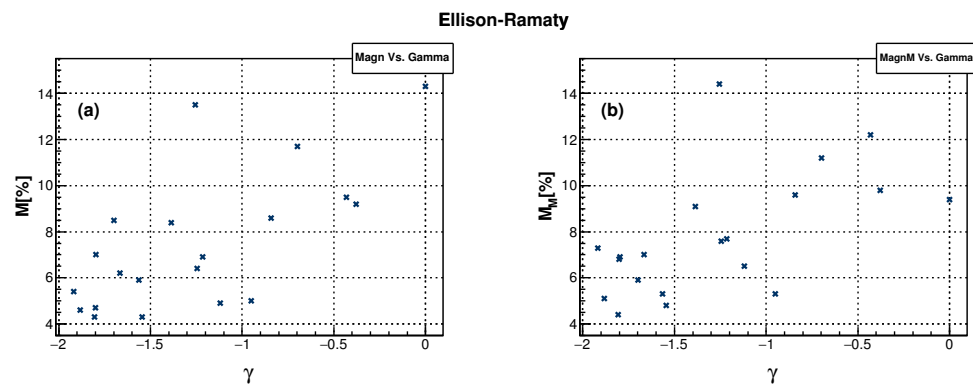


Figure 7. Dependence of FD magnitudes on the spectral index γ for (a) FD magnitude for particles with 10 GV rigidity and (b) FD magnitude for particles with 10 GV rigidity corrected for magnetospheric effect.

The new fitting procedure has undoubtedly improved the reliability with which spectral index α is determined, and for some events, the newly obtained values have changed non-negligibly. However, the effect of the new results on the dependence shown in Figure 5 was not dramatic. A much larger change was observed in new values for the parameter β (Figure 6). Where before it exhibited similar dependence as spectral index α in relation to FD magnitudes, now it is clear there is little correlation between these quantities. A few reasons come to mind to explain this observation, which could be related to the origin, acceleration mechanisms, and potential transport effects of the higher energy

protons. However, we feel such a discussion is probably beyond the scope of this study, so for now this feature should be noted and further investigation left for future analysis. When it comes to the spectral index obtained from the Ellison–Ramaty fit, we observe a very similar relationship between γ and FD magnitudes as we do for α . This could indicate that the poorer fit of the Ellison–Ramaty function does not have a significant impact on this relationship. The observation seems consistent with our assumption, based on the negligible correlation between the spectral index β and FD magnitudes, that the importance of the shape of the high-energy part of the spectrum appears to be less significant for the relationship we are investigating.

It is worth noting that in the distributions shown in Figures 5 and 7, we observe what could be an outlier event (the July 2004 event with the value for M slightly below and the value for M_M slightly above 14%) A potential reason for the deviation could be the overestimation of the FD magnitude for this event. The July 2004 event occurred on 26 July at 22:49:00 (according to the IZMIRAN database). It was preceded by two other events: one on 22 July at 10:36:00 (with a magnitude of 5.2%) and the second one on 24 July at 06:13:00 (with a magnitude of 4.6%). Cosmic ray flux had not yet recovered from these two events before the occurrence of the 26 July FD. We believe that if that was not the case, the magnitude for this event would be several percent smaller, hence it would deviate less in distributions presented in Figures 5 and 7.

Previously [12], we noticed the possibility of the existence of two classes of events, where a different trend was observed for the events of smaller and events of larger FD magnitude, the boundary between them somewhat arbitrarily set to a magnitude of 6%. After refining the analysis in this work, the possibility of such classification is not eliminated but is somewhat less evident, and it appears to require a more careful analysis, which could be considered in a possible future extension of this study.

To quantify the proposed correlations between the spectral indices and FD magnitudes, we have performed a standard correlation analysis. Pearson correlation coefficients between FD magnitudes and spectral indices α , β , and γ , as well as several selected space weather parameters, are shown in Table 3. We omitted to include the results for the parameters E_B and E_0 , as they exhibited an insignificant correlation with other parameters of interest. Additionally, aside from a relatively modest correlation between γ and E_0 of -41% , they also showed negligible correlations with the spectral indices themselves.

Table 3. Correlation coefficients between FD magnitudes and spectral indices, as well as selected space weather parameters.

	α	β	γ	V_{meanC} [kms ⁻¹]	V_{max} [kms ⁻¹]	Dst_{min} [nT]
M [%]	0.70	-0.05	0.68	0.78	0.79	-0.38
M_M [%]	0.54	-0.15	0.59	0.54	0.53	-0.42

The correlation between spectral index α and FD magnitude M is roughly the same as previously reported (70% instead of 67%), while the correlation with FD magnitude corrected for the magnetospheric effect M_M is somewhat smaller (54% instead of 64%). There is barely any correlation between spectral index β with any of the FD magnitudes, as was indicated by the plots in Figure 6. Correlation coefficients for the spectral index γ have values comparable to those obtained for α —68% and 59% for M and M_M , respectively. We believe that these results are non-negligibly affected by the observed deviation of the July 2004 event and that the actual correlations are stronger. Indeed, if the July 2004 event is removed, the correlations increase for both spectral indices α and γ , as shown in Table 4.

Table 4. Correlation coefficients between FD magnitudes, spectral indices, as well as selected space weather parameters, with the July 2004 event excluded.

	α	β	γ	V_{meanC} [kms ⁻¹]	V_{max} [kms ⁻¹]	Dst_{min} [nT]
M [%]	0.83	−0.07	0.77	0.81	0.80	−0.39
M_M [%]	0.71	−0.20	0.73	0.54	0.52	−0.47

Based on the results in Table 3, we see that the correlation between FD magnitude M and spectral indices α and γ are only slightly smaller than the correlations between M and the maximum hourly solar wind speed (V_{max}) and average CME velocity (V_{meanC}), which are quantities that typically show the largest correlation with FD magnitudes [36], and could be considered as the best predictors for FD magnitudes among space weather parameters. On the other hand, the correlations between the corrected FD magnitude M_M and spectral indices are comparable to the correlations between M_M and V_{max} and V_{meanC} . If the July 2004 event is not taken into account (results presented in Table 4), the correlations with M for both spectral indices become comparable to those for V_{max} and V_{meanC} . More importantly, for M_M , the correlations are significantly larger for both indices, indicating the extent to which the results in Table 3 were negatively influenced by the deviation of the July 2004 event.

Presented results, particularly the ones in Table 4, indicate even more strongly than in our previous work the significant correlation between spectral indices used to parameterize the shape of fluence spectra of energetic protons and FD magnitudes. The level of correlation for magnitude M suggests that spectral indices α and γ serve as equally effective predictors of FD magnitude for particles with 10 GV rigidity obtained by the GSM model (M) as other space weather parameters, while for the FD magnitude for particles with 10 GV rigidity corrected for magnetospheric effects (M_M), they appear to be better predictors than other parameters. The results for both α and γ are largely comparable, and they seem to be almost equally useful for our study. However, if we had to choose the recommended model for use in this type of analysis, it would be the model proposed by Band et al. This model proved to be more flexible, especially in modeling the “knee” and the higher energy part of the energetic proton fluence spectra. The potential downside of this model is that it requires some effort in implementation. In that sense, we believe the Ellison–Ramaty model remains a useful tool due to its robustness and ‘out-of-the-box’ applicability.

It was shown [1] that even during complex heliospheric events, involving multiple CMEs in succession, it was possible to calculate with sufficient accuracy the magnitude of the FD outside the geomagnetic field (corrected for the magnetospheric effect) using the established correlation. The obtained value for the FD magnitude corrected for magnetospheric effects was −8.3%, which was in good agreement with the value of −7.7% obtained from the GSM (the relative difference between the two methods being 7%). In the case of the FD magnitude measured at Earth relative difference was somewhat larger (15%), where we obtained the value of −8.1%, while the value calculated based on the GSM was −6.9%. These results indicate that the established correlations, even without additional refinement, can reliably predict FD amplitudes.

6. Conclusions

We presented an extension of our work, focusing on studying the connection between disturbances in the flux of energetic particles in the heliosphere and concurrent variations in the cosmic ray flux induced by the passage of a CME/ICME. Energetic proton flux, measured by the SOHO/ERNE instrument at L1 in twenty energy channels, was integrated over the duration of the event to obtain differential fluence spectra. To enhance the accuracy of this procedure, IMF and CME speed data provided by the WIND satellite were utilized. Fluence spectra were fitted with both the Ellison–Ramaty model and the model proposed by Band et al., and their effectiveness was compared. Cross-correlation between the spectral power indices obtained from the models and FD magnitudes, calculated by the GSM model

for 10 GV particles from the IZMIRAN database, was performed. The correlation between spectral indices and FD magnitude for events of moderate-to-high magnitude proved to be significant and, with the exception of the July 2004 event, comparable to the correlation with other space weather parameters that could be considered good predictors of FD magnitude. In the case of FD magnitude corrected for magnetospheric effects, the correlation with spectral indices is greater than for any other space weather parameter. Even though the Ellison–Ramaty model was able to model the energetic proton fluence spectra well in many cases, the model proposed by Band et al. performed better overall. Therefore, in our opinion, it should be the recommended model for similar studies.

Author Contributions: Conceptualization, M.S. and N.V.; methodology, M.S., N.V., D.M., F.Š., and A.D.; software, M.S., N.V., D.M. and F.Š.; validation, M.S., N.V., D.M., F.Š. and A.D.; formal analysis, M.S., N.V., D.M. and F.Š.; investigation, M.S., N.V., D.M. and F.Š.; resources, M.T. and M.S.; data curation, R.B., M.T. and M.S.; writing—original draft preparation, M.S. and N.V.; writing—review and editing, M.S., N.V., D.M., F.Š. and A.D. visualization, M.S. and N.V. All authors have read and agreed to the published version of the manuscript.

Funding: This work was funded by the Institute of Physics Belgrade, University of Belgrade, through a grant by the Ministry of Science, Technological Development and Innovations of the Republic of Serbia.

Data Availability Statement: Energetic proton data from SOHO/ERNE instrument are publicly available via OMNIWeb FTP page https://omniweb.gsfc.nasa.gov/ftpbrowser/soho_erne_flux_hr.html (accessed on 31 May 2024). IMF and solar wind speed time series measured by the WIND spacecraft are openly available at https://omniweb.gsfc.nasa.gov/ftpbrowser/wind_swe_2m.html (accessed on 31 May 2024). IZMIRAN database of Forbush decreases is free for public access at <http://spaceweather.izmiran.ru/eng/dbs.html> (accessed on 31 May 2024).

Acknowledgments: We would like to express our gratitude to the Reviewers for constructive comments and useful suggestions that significantly contributed to the quality of the manuscript. OMNI data were made available by NASA/GSFC’s Space Physics Data Facility’s OMNIWeb service. We acknowledge SOHO, a project of international cooperation between ESA and NASA. Additionally, we gratefully acknowledge the Cosmic Ray Group at the IZMIRAN Space Weather Prediction Center at the Pushkov Institute of Terrestrial Magnetism, Ionosphere, and Radio Wave Propagation of the Russian Academy of Sciences for providing the data used in our study.

Conflicts of Interest: The authors declare no conflicts of interest.

Abbreviations

The following abbreviations are used in this manuscript:

SF	Solar Flare
CME	Coronal Mass Ejection
ICME	Interplanetary coronal mass ejections
SEP	Solar Energetic Particles
CR	Cosmic Rays
FD	Forbush decrease
L1	Lagrange Point 1
IMF	Interplanetary Magnetic Field
Dst index	Disturbance Storm Time index
ERNE	Energetic and Relativistic Nuclei and Electron sensor unit
SOHO	Solar and Heliospheric Observatory
GSM	Global Survey Method
MCMC	Markov Chain Monte Carlo

References

1. Kolarski, A.; Veselinović, N.; Srećković, V.A.; Mijić, Z.; Savić, M.; Dragić, A. Impacts of Extreme Space Weather Events on September 6th, 2017 on Ionosphere and Primary Cosmic Rays. *Remote Sens.* **2023**, *15*, 1403. [CrossRef]
2. Yashiro, S.; Gopalswamy, N. Statistical relationship between solar flares and coronal mass ejections. *Univers. Heliophysical Processes Proc. IAU Symp.* **2008**, *4*, 233–243. [CrossRef]
3. Rotti, S.; Petrus, C.; Martens, P.C. Analysis of SEP Events and Their Possible Precursors Based on the GSEP Catalog2023. *Astrophys. J. Suppl. Ser.* **2023**, *267*, 40. [CrossRef]
4. Reames, D.V. The Two Sources of Solar Energetic Particles. *Space Sci. Rev.* **2013**, *175*, 53–92. [CrossRef]
5. Posner, A.; Strauss, R.D. Warning time analysis from SEP simulations of a two-tier RELeASE System applied to Mars exploration. *Space Weather* **2020**, *18*, e2019SW002354. [CrossRef]
6. Kataoka, R.; Sato, T.; Miyake, S.; Shiota, D.; Kubo, Y. Radiation dose nowcast for the ground level enhancement on 10–11 September 2017. *Space Weather* **2018**, *16*, 917–923. [CrossRef]
7. Waterfall, C.O.G.; Dalla, S.; Raukunen, O.; Heynderickx, D.; Jiggins, P.; Vainio, R. High energy solar particle events and their relationship to associated flare, CME and GLE parameters. *Space Weather* **2023**, *21*, e2022SW003334. [CrossRef]
8. Belov, A.; Abunin, A.; Abunina, M.; Eroshenko, E.; Oleneva, V.; Yanke, V.; Papaioannou, A.; Mavromichalaki, H.; Gopalswamy, N.; Yashiro, S. Coronal mass ejections and non-recurrent forrush decreases. *Sol. Phys.* **2014**, *289*, 3949–3960. [CrossRef]
9. Belov, A.; Shlyk, N.; Abunina, M.; Belova, E.; Abunin, A.; Papaioannou, A. Solar Energetic Particle Events and Forrush Decreases Driven by the Same Solar Sources. *Universe* **2022**, *8*, 403. [CrossRef]
10. Cane, H. Coronal mass ejections and forrush decreases. *Space Sci. Rev.* **2000**, *93*, 55–77. [CrossRef]
11. Gopalswamy, N. History and development of coronal mass ejections as a key player in solar terrestrial relationship. *Geosci. Lett.* **2016**, *3*, 8. [CrossRef]
12. Savić, M.; Veselinović, N.; Dragić, A.; Maletić, D.; Joković, D.; Udovičić, V.; Banjanac, R.; Knežević, D. New insights from cross-correlation studies between solar activity indices and cosmic-ray flux during Forrush decrease events. *Adv. Space Res.* **2023**, *71*, 2006–2016. [CrossRef]
13. Dumbovic, M.; Vrsnak, B.; Guo, J.; Heber, B.; Dissauer, K.; Carcaboso, F.; Temmer, M.; Veronig, A.; Podladchikova, T.; Möstl, C.; et al. Evolution of coronal mass ejections and the corresponding forrush decreases: Modeling vs. multi-spacecraft observations. *Sol. Phys.* **2020**, *295*, 104. [CrossRef]
14. Papaioannou, A.; Belov, A.; Abunina, M.; Eroshenko, E.; Anastasiadis, A.; Patsourakos, S.; Mavromichalaki, H. Interplanetary coronal mass ejections as the driver of non-recurrent Forrush decreases. *Astrophys. J.* **2020**, *890*, 101. [CrossRef]
15. OMNIWeb Plus Service. Available online: <https://omniweb.gsfc.nasa.gov/> (accessed on 12 February 2024).
16. IZMIRAN. Available online: <https://www.izmiran.ru/> (accessed on 12 February 2024).
17. Torsti, J.; Valtonen, E.; Lumme, M.; Peltonen, P.; Eronen, T.; Louhola, M.; Riihonen, E.; Schultz, G.; Teittinen, M.; Ahola, K.; et al. Energetic particle experiment ERNE. *Sol. Phys.* **1995**, *162*, 505–531. [CrossRef]
18. Paassilta, M.; Raukunen, O.; Vainio, R.; Valtonen, E.; Papaioannou, A.; Siipola, R.; Riihonen, E.; Dierckx, M.; Crosby, N.; Malandraki, O.; et al. Catalogue of 55–80 MeV solar proton events extending through solar cycles 23 and 24. *J. Space Weather Space Clim.* **2017**, *7*, A14. [CrossRef]
19. Belov, A.; Papaioannou, A.; Abunina, M.; Dumbovic, M.; Richardson, I.G.; Heber, B.; Kuhl, P.; Herbst, K.; Anastasiadis, A.; Vourlidas, A.; et al. On the rigidity spectrum of cosmic-ray variations within propagating interplanetary disturbances: Neutron monitor and SOHO/EPHIN observations at 1–10 GV. *Astrophys. J.* **2021**, *908*, 5. [CrossRef]
20. Wilson, L.B.; Brosius, A.L.; Gopalswamy, N.; Nieves-Chinchilla, T.; Szabo, A.; Hurley, K.; Phan, T.; Kasper, J.C.; Noé Lugaz, N.; Richardson, I.G.; et al. A quarter century of wind spacecraft discoveries. *Rev. Geophys.* **2021**, *59*, e2020RG000714. [CrossRef]
21. Belov, A.; Eroshenko, E.; Yanke, V.; Oleneva, V.; Abunin, A.; Abunina, M.; Papaioannou, A.; Mavromichalaki, H. The Global Survey Method Applied to Ground-level Cosmic Ray Measurements. *Sol. Phys.* **2016**, *293*, 578. [CrossRef]
22. Janvier, M.; Démoulin, P.; Guo, J.; Dasso, S.; Regnault, F.; Tóth, S.; Moutoussidou, S.; Gutierrez, C.; Perri, B. The Two-step Forrush Decrease: A Tale of Two Substructures Modulating Galactic Cosmic Rays within Coronal Mass Ejections. *Astrophys. J. Lett.* **2021**, *922*, 216. [CrossRef]
23. Gopalswamy, N. The Sun and Space Weather. *Atmosphere* **2022**, *13*, 1781. [CrossRef]
24. Desai, M.; Giacalone, J. Large gradual solar energetic particle events. *Living Rev. Sol. Phys.* **2016**, *13*, 3. [CrossRef]
25. Vainio, R.; Valtonen, E.; Heber, B.; Malandraki, O.E.; Papaioannou, A.L.; Klein, K.L.; Afanasiev, A.; Agueda, N.; Aurass, H.; Battarbee, M.; et al. The first SEPServer event catalogue ~68-MeV solar proton events observed at 1 AU in 1996–2010. *JSWSC* **2013**, *3*, A12.
26. Mottl, D.A.; Nymmik, R.A.; Sladkova, A.I. Energy spectra of high-energy SEP event protons derived from statistical analysis of experimental data on a large set of events. In Proceedings of the Space Technology and Applications International Forum—2001, Albuquerque, NM, USA, 11–14 February 2001; pp. 1191–1196.
27. Nymmik, R.A. Inflections (knees) in wide-range spectra of solar energetic protons and heavy ions: Their form, parameters, and regularities. *Bull. Russ. Acad. Sci. Phys.* **2011**, *75*, 761–763. [CrossRef]
28. Miroshnichenko, L.I.; Nymmik, R.A. Extreme fluxes in solar energetic particle events: Methodological and physical limitations. *Radiat. Meas.* **2011**, *61*, 6–15. [CrossRef]
29. Zhao, L.; Zhang, M.; Rassoul, H.K. Double power laws in the event-integrated solar energetic particle spectrum. *Astrophys. J.* **2016**, *821*, 62. [CrossRef]

30. Band, D.; Matteson, J.; Ford, L.; Schaefer, B.; Palmer, D.; Teegarden, B.; Cline, T.; Briggs, M.; Pacieras, W.; Pendleton, G.; et al. BATSE Observations of Gamma-Ray Burst Spectra. I. Spectral Diversity. *Astrophys. J.* **1993**, *413*, 281. [[CrossRef](#)]
31. Raukunen, O.; Vainio, R.; Tylka, A.J.; Dietrich, W.F.; Jiggins, P.; Heynderickx, D.; Dierckxsens, M.; Crosby, N.; Ganse, U.; Siipola, R. Two solar proton fluence models based on ground level enhancement observations. *J. Space Weather Spac.* **2018**, *A04*, 8. [[CrossRef](#)]
32. Nymmik, R.A. Charge states of heavy ions, as determined from the parameters of solar energetic particle spectra. *Bull. Russ. Acad. Sci. Phys.* **2013**, *77*, 490–492. [[CrossRef](#)]
33. Ellison, D.C.; Ramaty, R. Shock acceleration of electrons and ions in solar flares. *Astrophys. J.* **1985**, *298*, 400–408. [[CrossRef](#)]
34. Mewaldt, R.A.; Cohen, C.M.S.; Labrador, A.W.; Leske, R.A.; Mason, G.M.; Desai, M.I.;Looper, M.D.; Mazur, J.E.; Selesnick, R.S.; Haggerty, D.K. Proton, helium, and electron spectra during the large solar particle events of October–November 2003. *J. Geophys. Res.* **2005**, *110*, A09S18. [[CrossRef](#)]
35. NMDB: The Neutron Monitor Database. Available online: <https://www.nmdb.eu/> (accessed on 12 February 2024).
36. Lingri, D.; Mavromichalaki, H.; Belov, A.; Eroshenko, E.; Yanke, V.; Abunin, A.; Abunina, M. Solar Activity Parameters and Associated Forbush Decreases During the Minimum Between Cycles 23 and 24 and the Ascending Phase of Cycle 24. *Sol. Phys.* **2016**, *291*, 1025–1041. [[CrossRef](#)]

Disclaimer/Publisher’s Note: The statements, opinions and data contained in all publications are solely those of the individual author(s) and contributor(s) and not of MDPI and/or the editor(s). MDPI and/or the editor(s) disclaim responsibility for any injury to people or property resulting from any ideas, methods, instructions or products referred to in the content.